NASA Technical Paper 3605

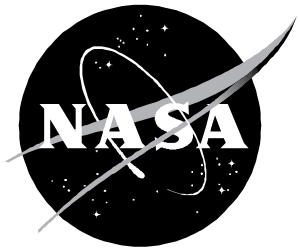

A Study of Fundamental Shock Noise Mechanisms

Kristine R. Meadows
Langley Research Center • Hampton, Virginia

National Aeronautics and Space Administration
Langley Research Center • Hampton, Virginia 23681-0001

April 1997

Available electronically at the following URL address: http://techreports.larc.nasa.gov/ltrs/ltrs.html

Printed copies available from the following:

NASA Center for AeroSpace Information
800 Elkridge Landing Road
Linthicum Heights, MD 21090-2934
(301) 621-0390

National Technical Information Service (NTIS)
5285 Port Royal Road
Springfield, VA 22161-2171
(703) 487-4650

Contents

List of Figures

Abstract

This paper investigates two mechanisms fundamental to sound generation in shocked flows: shock motion and shock deformation. Shock motion is modeled numerically by examining the interaction of a sound wave with a shock. The numerical approach is validated by comparison with results obtained by linear theory for a small-disturbance case. Analysis of the perturbation energy with Myers' energy corollary demonstrates that acoustic energy is generated by the interaction of acoustic disturbances with shocks. This analysis suggests that shock motion generates acoustic and entropy disturbance energy. Shock deformation is modeled numerically by examining the interaction of a vortex ring with a shock. These numerical simulations demonstrate the generation of both an acoustic wave and contact surfaces. The acoustic wave spreads cylindrically. The sound intensity is highly directional and the sound pressure increases with increasing shock strength. The numerically determined relationship between the sound pressure and the Mach number is found to be consistent with experimental observations of shock noise. This consistency implies that a dominant physical process in the generation of shock noise is modeled in this study.

Introduction

This research was conducted to establish a better understanding of the physical nature of sound generation in shocked flows. Increased understanding of the primary mechanisms in shock noise generation can be applied to a variety of aerodynamic problems. In helicopter and tilt-rotor aircraft, shock waves may form on blade surfaces and vortices from a preceding blade may interact with this shock, which results in impulsive noise. In supersonic engine inlets, combustion instabilities may result in shock oscillation that leads to what is commonly known as buzz (ref. 1). Subsonic transport aircraft often operate at conditions where the flow over the wing is transonic and unsteadiness in the flow over the wing can cause the shock to oscillate and generate noise.

The primary focus during this research was sound generation in supersonic jets. When jet engines operate at supercritical nozzle pressure ratios, shock waves may form in the jet plume. Turbulence interacting with the shock waves generates high amplitude, broadband noise, typically known as broadband shock noise or shock-associated noise. The expected shock noise during the climb-to-cruise operating condition of a supersonic civil transport may ruin its chance of ever being put in production. Shock noise is an important design issue because of the effects on airport communities, aircraft interiors, and structural fatigue.

Research toward the understanding of noise generation in jet flows has been ongoing for over 40 years. Morley in an investigation of sound intensity in the far field of turbulent jets showed that the sound power is proportional to about the eighth power of the jet velocity (ref. 2). Lighthill in his pioneering work on jet noise theory provided a theoretical basis for the eighth power law of Morley (ref. 3). Lighthill also provided a basis for an understanding of other jet noise phenomena, such as convective amplification (ref. 3). Lilley provides a review of classical jet noise theory and related experiments (ref. 4). There are two review papers specific to noise generation in supersonic jets that summarize significant contributions to the understanding of jet noise. The first, written from the perspective of an experimentalist, is the review paper by Seiner (ref. 5). The second, written from the perspective of a theoretician, is the review paper by Tam (ref. 6). The complicated nature of supersonic jet flow makes development of a comprehensive theory difficult and therefore the theories available for the prediction of shock noise in jets are largely empirical.

The approach of research reported herein is to compute directly the sound generated by shock waves in supersonic jets. Advances in computer hardware that resulted in more computational speed, affordable memory, and parallel architectures combined with advances in software that resulted in more efficient, accurate algorithms, and better networking have made this approach feasible for relatively simple, two-dimensional problems.

Direct computation of aerodynamically generated sound is useful because sound is inherently a component of a fluid flow field. The basic equations that govern sound are the same as those that govern fluid flow. For Newtonian fluid flows, these equations are the Navier-Stokes equations, or when viscous effects can be neglected, the Euler equations. As shown in figure 2, the acoustic portion of a fluid flow field consists of small perturbations on an inviscid, compressible flow. The generation of sound waves, however, often involves viscous nonlinear effects. Thus, an advantage of performing a direct simulation of the fully nonlinear equations is that both the sound generation and propagation are computed in the same analysis. In contrast, traditional acoustic methods require that the near field be found through a separate computation or experiment and the far field be computed with an acoustic analogy or Kirchhoff formulation.

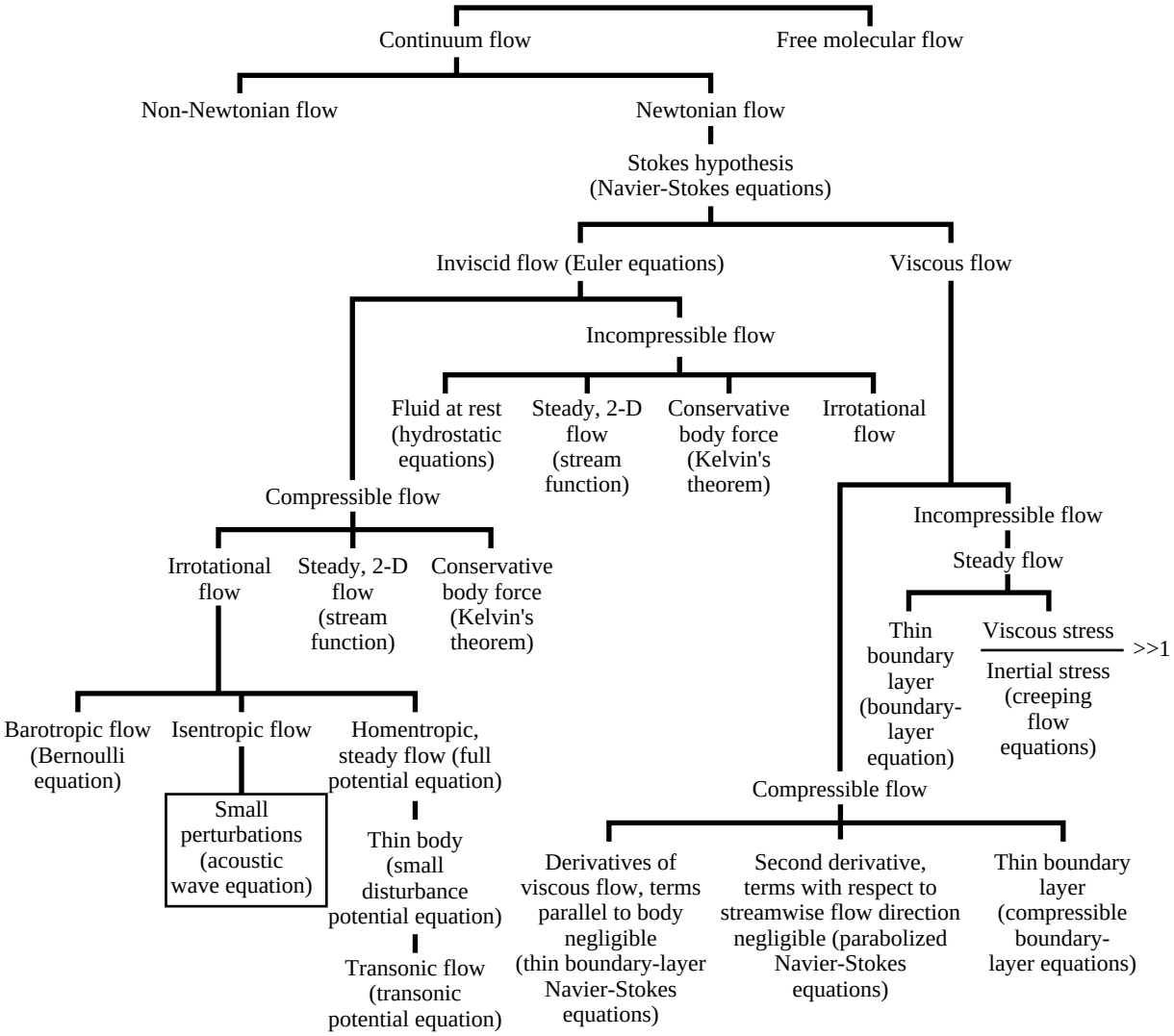

Figure 2. Some equations of fluid mechanics.

Direct computation is currently not feasible for routine study of supersonic jet flow because the flow contains far too many scales to be resolved in a reasonable computation. Therefore, a combined modeling and direct computation approach is taken in this research. First, the complicated flow field of a supersonic jet is simplified into model problems, which are chosen to isolate mechanisms that are likely to generate sound. The modeling of supersonic jet flow is described in chapter 1.

Chapter 1 begins with a description of features that are characteristic of supersonic jet noise and then proceeds to divide the complicated flow into several simpler problems that can readily be solved. Chapter 1 also presents an analytical model for shock noise generation. In this analysis, Lighthill's equation is used to derive the monopole, dipole, and quadrupole source terms that are associated with a moving planar shock. The source terms are presented and then Green's function is used to compute the far field sound that is associated with each of the source terms. All source terms were found to potentially contribute significantly to the far field sound.

Chapter 2 addresses numerical methods and some challenges in the computation of flows with moving shocks. Computation of sound generation in shocked flows is challenging because high-order accuracy is required to determine the acoustic portion of the solution, while numerical dissipation is required at the shock to maintain stability. Most calculations presented in this report use a finite-volume implementation of an essentially nonoscillatory (ENO) scheme. Because this algorithm is the basis for most calculations of this research, a brief description is included in this chapter.

Once candidate sound generating mechanisms are identified and modeled and the numerical methods are in place, the flow for each model problem can be computed and the acoustics extracted from the calculation. Chapter 3 describes the results obtained by an investigation of the first model problem: sound wave and shock wave interaction. Computations of the interaction of a sound wave with a shock wave in a quasi-one-dimensional nozzle show significant amplification of the sound wave pressure amplitude as a result of this interaction. The increase in amplitude of the acoustic pressure is shown to be a function of the Mach number upstream of the shock. Comparisons with linear theory are made for the small-disturbance calculations that validate the code. Results are also provided for the higher amplitude cases. In addition, an energy analysis is performed that shows that acoustic energy is generated during sound and shock interaction.

Chapter 4 presents results that were obtained by the investigation of the interaction of a vortex ring with a shock wave. This sound generating mechanism is more complicated than the plane sound and shock interaction because the shock bends during the interaction, which generates alternating compression and rarefaction regions along the acoustic wave front. Flow parameters downstream of the shock are observed and the conclusion is drawn that both acoustic waves and contact surfaces result from the interaction. Analysis of the results shows that the acoustic wave spreads cylindrically, that the sound intensity is highly directional, and that the sound pressure level increases significantly with increasing shock strength. The effect of shock strength on sound pressure level is consistent with experimental observations of shock noise, which indicates that the interaction of a ring vortex with a shock wave correctly models some of the physics of shock noise generation.

Figure Symbols

c_{01}	upstream stagnation speed of sound
c_1	upstream speed of sound
c_2	downstream speed of sound
c_∞	ambient speed of sound
ENO	essentially nonoscillatory
I_r	radial component of intensity
I_{cx}	axial component of intensity from classical definition

I_x	axial component of intensity
L_1	error norm
M	Mach number
M_D	design Mach number
M_s	perturbation Mach number
M_0	undisturbed upstream Mach number
M_1	upstream Mach number
M_2	downstream Mach number
$\mathbf{n}$	surface normal vector
p_D	pressure of dipole term in Lighthill analysis
p_M	pressure of monopole term in Lighthill analysis
p_Q	pressure of quadrupole term in Lighthill analysis
p_1	pressure upstream of shock
p_2	pressure downstream of shock
p_∞	ambient pressure
R	radial distance from vortex core
R_s	shock disk radius
r	radial coordinate
r_c	vortex core radius
r_o	distance from observer to center of shock
r_0	vortex ring radius
SPL	sound pressure level
s	entropy
T	normalized time
t	time
U	mean flow velocity
U_1	state upstream of shock
U_2	state between shock and contact surface
U_3	state between contact surface and acoustic wave
U_4	undisturbed state downstream of shock
u	velocity component normal to shock
u_s	shock velocity
u_1	upstream velocity
u_2	downstream velocity
V	vortex translation velocity
v	radial velocity
v_θ	tangential velocity
x	streamwise coordinate
x_0	initial axial coordinate of vortex ring

$\mathbf{x}$	observer position vector
$\mathbf{y}$	source position vector
β	measure of upstream Mach number
Γ	circulation strength of vortex
Δs	change in entropy across shock
δp	perturbation pressure
δp_{max}	maximum perturbation pressure
δp_{min}	minimum perturbation pressure
δp_1	perturbation pressure upstream of shock
δp_2	perturbation pressure downstream of shock
δs	perturbation entropy
δs_{max}	maximum perturbation entropy
δs_2	perturbation entropy downstream of shock
δU_1	perturbation of upstream state
δu	perturbation axial velocity
δv	perturbation radial velocity
δx_s	perturbation shock position
$\delta\rho$	perturbation density
$\delta\rho_1$	perturbation density upstream
$\delta\rho_2$	perturbation density downstream
$\delta\omega$	perturbation vorticity
ε	perturbation amplitude parameter
Θ	angle from horizontal
θ	angle from jet axis to observer
ξ	vortex filament position
ρ_1	upstream density
ρ_2	downstream density
ρ_∞	ambient density
σ	radial coordinate to source point
ϕ	observer angle about axis of symmetry
χ	angle to source point in plane of shock disk
ψ	angle from jet axis to source point
ω	frequency of disturbance
2-D	two-dimensional

Chapter 1

Modeling of Sound Generating Mechanisms in a Supersonic Jet

The inherently complicated nature of jet flows makes both theoretical analysis and direct numerical simulation impractical for realistic flow Mach and Reynolds numbers. The structure of the flow field of

a supersonic jet consists of regions of laminar flow, turbulent flow, and transitional flow. Within the jet a myriad of structures of disparate scales exists, such as turbulent eddies and shock waves, that make analysis of the fluid dynamics practically impossible for general flows. Highly accurate numerical simulation of these flows is impractical because of the disparity of the scales that must be resolved in the computation.

To predict accurately the sound generated by complex jet flows, the essential elements of the jet fluid dynamics must be resolved in the computation. Experimental studies of noise generation in supersonic jets have provided insight into what these essential elements may be. A result from an experimental investigation of sound generation in a supersonic axisymmetric jet is included in figure 3. This photographic image was produced by a horizontal spark schlieren of an underexpanded supersonic jet and confirms the complex nature of the jet flow (ref. 5). As the flow exits the nozzle, it rapidly becomes turbulent. For the underexpanded case shown here, shock waves are also present in the flow and a Mach disk is evident approximately one jet diameter downstream of the nozzle.

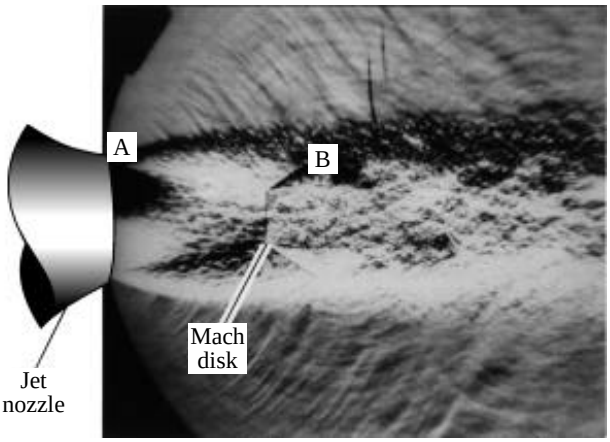

Figure 3. Schlieren photograph of underexpanded supersonic jet.

For the acoustician, the wave field outside the jet plume is of particular interest. Several types of waves are present, which indicate that several sound generating mechanisms are responsible. Two types of wave fields are intense enough to be readily visualized on schlieren photographs. The first wave field appears to emanate from a region close to the nozzle exit near marker A on the figure and radiate at approximately $\pm 30^\circ$ from the jet axis. These waves propagate to the far field as acoustic waves. The waves are thought to be generated by supersonically convecting eddies that occur when the jet flow is heated and when the plume Mach number approaches two in unheated flows (ref. 5). The eddies create a form of sound known as eddy Mach wave radiation, which generally dominates the noise spectrum in directions of its dominant directivity. The primary directivity can be determined by computing the angle complementary to the Mach angle. The Mach angle is determined from the eddy convection velocity by $\mu = \sin^{-1}(1/M)$ where M is the jet Mach number.

The second type of wave outside the jet plume appears to emanate from the terminal locations of the shock waves in the mixing layer. One such wave field is shown emanating from a region in the proximity of marker B in figure 3. This wave field appears to be more omnidirectional than the eddy Mach wave radiation because the wave fronts appear to spread spherically from the point of generation. This second type of acoustic wave is believed to be generated by the passage of turbulence through the shock waves and is referred to as broadband shock noise or shock noise. The broadband nature of this noise is illustrated in figure 4.

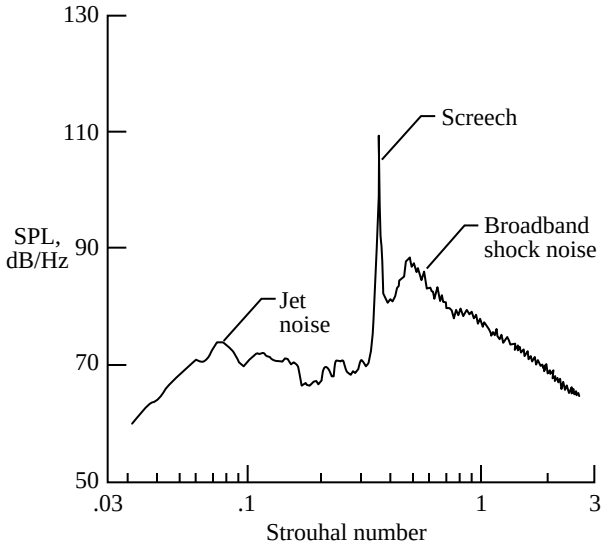

Figure 4. Spectrum of typical underexpanded supersonic jet.

Figure 4 shows the spectrum of a typical underexpanded supersonic jet at 150° from the jet axis. The spectrum is characterized by three phenomena that are highlighted in the figure. The figure shows that these three phenomena tend to occur in distinct frequency bands. At low Strouhal numbers (a dimensionless frequency formed by the product of the frequency and the jet diameter divided by the fully expanded jet velocity), jet noise dominates. Jet noise is generated by turbulent mixing of the fluid within the jet. The peak in jet noise, at a Strouhal number of about 0.1, is believed to be generated by the large scale structures within the shear layer and is typically referred to as eddy Mach wave radiation. Both large and small scales within the jet generate mixing noise. The mixing of the fine scales produces the background level of jet noise.

The peak of the spectrum is known as jet screech. Screech typically falls between the jet noise and the broadband shock noise in the spectrum. The accepted explanation for screech was originally proposed by Powell, who suggested that screech is generated when the turbulence interacting with shock waves in the flow develops a self-sustained aeroacoustic feedback loop (ref. 7). The resonant phenomenon, which generates a high amplitude sound at a particular frequency and its harmonics, is maintained by the shedding of a disturbance at the nozzle exit when sound passes the nozzle lip. Although Powell's explanation of the screech phenomenon is useful in explaining general features of the phenomenon, there are features of jet screech that are still not understood (ref. 5).

The high Strouhal number portion of the spectrum in figure 4 is called broadband shock noise. Broadband shock noise is present in all shocked jet flows and is due to the interaction of convecting disturbances with the shock waves in the jet plume. The broadband nature of this noise is due to the many scales of turbulent eddies in the flow. Experiments show that most of the broadband shock noise is directed slightly upstream (refs. 5 and 8).

Although jet engines are designed to be shock free at design operating conditions, jet engines are often operated at off-design conditions. Thus, screech and broadband shock noise can contribute significantly to the sound generated.

Models

Jet flows are too complicated to be practically analyzed or directly simulated. Therefore, the approach in this research is to identify elements essential to sound generation in supersonic jets and to analyze some models of these mechanisms for insight into the sound-generation processes.

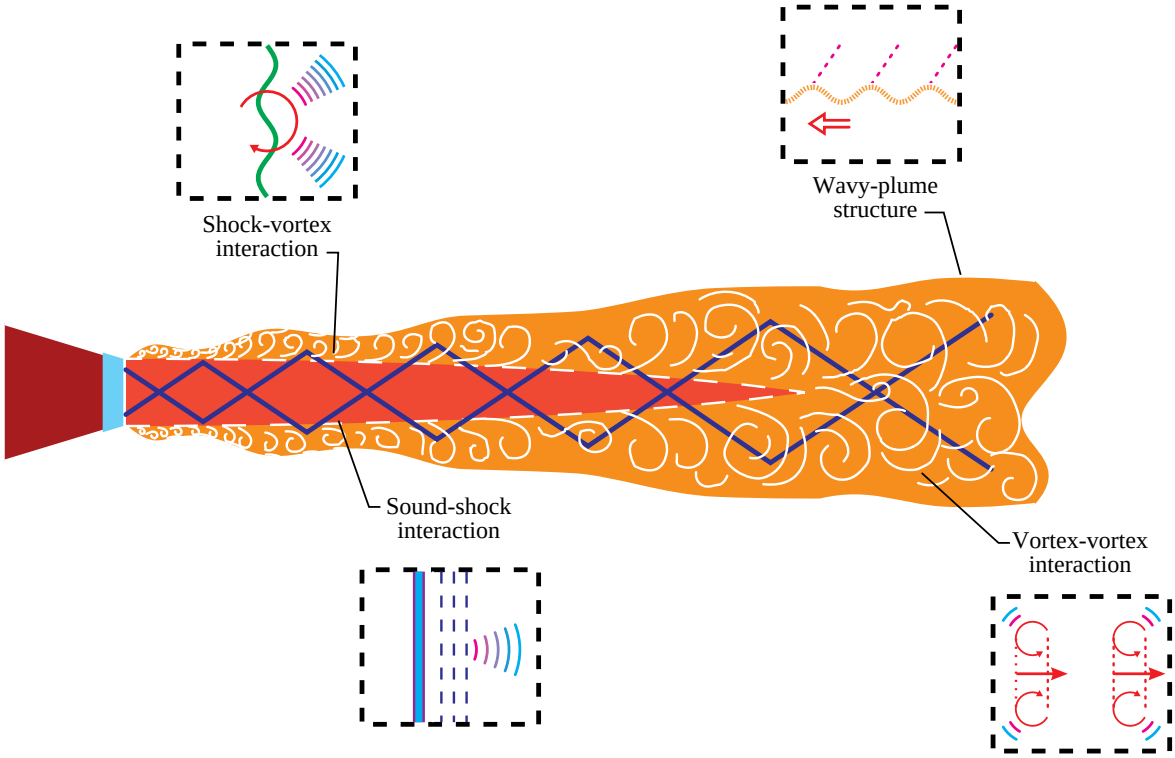

Figure 5. Fundamental sound-generating mechanisms of supersonic jet flow.

Experimental data indicate that noise is generated by different mechanisms within the jet. These sound-generating mechanisms associated with the complex flow of a supersonic jet are shown in figure 5. The first class of sound-generating mechanisms in the supersonic jet arises from the interaction of flow disturbances with the shock waves. The elements of the class that model the sound that is being generated by the interaction of flow disturbances with shock waves are illustrated in figure 5. These elements are (1) the interaction of a vortex with a plane shock wave and (2) the interaction of a plane sound wave with a shock. These two elements will be discussed in detail in chapters 3 and 4.

Additional models of sound generating mechanisms that are not directly related to the presence of shock waves are also illustrated in figure 5. The model presented for a wavy-plume structure is flow past a wavy wall. This models the component of sound generated by large scale structures within the jet plume. Clearly, Mach waves are expected to be generated by flow past a wavy wall, and in the model, these Mach waves are analogous to the eddy Mach wave radiation from supersonic jets. The vortex and vortex interaction model presented in figure 5 illustrates the interaction of turbulent structures within the jet, which are believed to be responsible for the background noise (jet noise) of supersonic jet flows.

Evaluation of Sound Generation by Shock Motion With Lighthill's Equation

This section presents an analysis of sound generation by shock motion in the context of Lighthill's acoustic analogy (ref. 3).

Background

Lighthill combined the equations that govern the conservation of mass and momentum into an inhomogeneous wave equation. A brief derivation of Lighthill's equation follows.

The physical law governing the conservation of mass written in indicial form is

$$\frac{\partial \rho}{\partial t} + \frac{\partial (\rho u_j)}{\partial x_j} = Q \qquad j = 1,2,3 \tag{1}$$

where ρ is the fluid density, u_j is the jth component of velocity, t is time, x_j is the coordinate in the jth direction, and Q is the mass per unit time per unit volume injected into the fluid.

The conservation of momentum equations are written as

$$\rho \frac{\partial u_i}{\partial t} + \rho u_i \frac{\partial u_j}{\partial x_j} = -\frac{\partial P_{ij}}{\partial x_j} + F_i \qquad i,j = 1,2,3 \tag{2}$$

where F_i is an externally applied force, the stress tensor $P_{ij} = p\delta_{ij} - \sigma_{ij}$, where p is pressure, δ_{ij} is the Kroneker delta, and σ_{ij} is the viscous stress tensor, $\sigma_{ij} = 2\mu e_{ij} - \lambda e_{kk}\delta_{ij}$, where $e_{ij} = 1/2\,(\partial u_i/\partial x_j + \partial u_j/\partial x_i)$, and μ and λ are the dynamic viscosity and second coefficient of viscosity, respectively.

Taking the inner product of u_i with equation (1) and adding it to equation (2) produces:

$$\frac{\partial \rho u_i}{\partial t} + \frac{\partial (\rho u_i u_j)}{\partial x_j} + \frac{\partial P_{ij}}{\partial x_j} = F_i + u_i Q \tag{3}$$

Differentiating equation (1) with time, subtracting the divergence of equation (3), and adding and subtracting $c_\infty^2 \nabla^2 \rho$, produces Lighthill's equation:

$$\frac{\partial^2 \rho}{\partial t^2} - c_\infty^2 \nabla^2 \rho = \frac{\partial Q}{\partial t} - \frac{\partial (F_i + u_i Q)}{\partial x_i} + \frac{\partial^2 T_{ij}}{\partial x_i \partial x_j} \tag{4}$$

where c_∞ is the free stream speed of sound and the stress tensor is defined as

$$T_{ij} = \rho u_i u_j - \sigma_{ij} + p\delta_{ij} - c_\infty^2 \rho \delta_{ij} \tag{5}$$

The terms on the right side of equation (4) are the acoustic source terms. The terms $\partial Q/\partial t$ represent sound generated by unsteady mass addition; $\partial (F_i + u_i\, Q)/\partial x_i$ represents unsteady forces; $\rho u_i u_j$ represents nonlinear viscous effects, turbulence, and nonlinear propagation; and $(p - \rho c_\infty^2)\delta_{ij}$ represents nonisentropic effects such as shock waves and heat addition. Effects of viscosity on the sound generation are represented by σ_{ij}.

Source Terms

Here, Lighthill's equation will be used to analyze the sound generated by shock oscillation. To simplify the analysis, dissipation effects are neglected and only the velocity component normal to the shock u is considered. Since there are no applied forces or unsteady mass addition, the source term simplifies to

$$T_{11} = \rho u^2 + p - \rho c_\infty^2 \tag{6}$$

The source term of Lighthill's equation requires that the second partial derivative of T_{11} be taken with respect to x. It is beneficial to use generalized functions because ordinary derivatives do not exist across the shock. The definition of a generalized derivative in one dimension is (ref. 9)

$$\frac{\bar{\partial} f(x,t)}{\partial x} = \frac{\partial f(x,t)}{\partial x} + \Delta f \delta (x - x_s) \tag{7}$$

where $\bar{\partial}/\partial x$ represents the generalized derivative operator, $\partial/\partial x$ is the ordinary derivative, and Δf represents the jump in the function f at the discontinuity located at $x = x_s$.

Applying equation (7) twice to obtain $\partial^2 T_{11}/\partial x^2$,

$$\frac{\bar{\partial} T_{11}}{\partial x} = \frac{\partial T_{11}}{\partial x} + \Delta T_{11}\delta(x - x_s)$$

$$\frac{\bar{\partial}^2 T_{11}}{\partial x^2} = \frac{\partial^2 T_{11}}{\partial x^2} + \frac{\partial}{\partial x}[\Delta T_{11}\delta(x - x_s)] + \Delta\left(\frac{\partial T_{11}}{\partial x}\right)\delta(x - x_s) \tag{8}$$

Thus, the source term in Lighthill's equation for sound generated by a moving shock has components that resemble shearing stresses (quadrupole), unsteady forces (dipole), and mass addition (monopole), which are represented by first, second, and third terms on the right side of equation (8), respectively.

In classical acoustics, where sound generation is considered in an ambient medium, the sound pressure associated with monopoles, dipoles, and quadrupoles is proportional to the second, third, and fourth power of the source Mach number, respectively. Therefore, the monopole source dominates at low Mach numbers, and the quadrupole source dominates at high Mach numbers. However, for sound generation at transonic speeds, each component may contribute significantly to the sound generation. It is a purpose of this section to analytically determine which term dominates the shock noise generation.

To determine the behavior of the monopole, dipole, and quadrupole terms as functions of Mach number, consider a planar shock that is set in motion by an upstream disturbance in Mach number (fig. 6). The Mach number upstream of the shock is

$$M_1 = M_0 - M_s \cos(\omega t - kx) \tag{9}$$

where M_0 is the undisturbed upstream Mach number, M_s is the maximum amplitude of the disturbance Mach number, ω is the frequency of the disturbance, and k is the wave number. Disturbances in pressure, density, and sound speed upstream of the shock are neglected because these quantities are proportional to the square of the upstream disturbance Mach number.

Monopole source term. The monopole term on the right hand side of equation (8) is

$$\Delta\left(\frac{\partial T_{11}}{\partial x}\right)\delta(x - x_s) \tag{10}$$

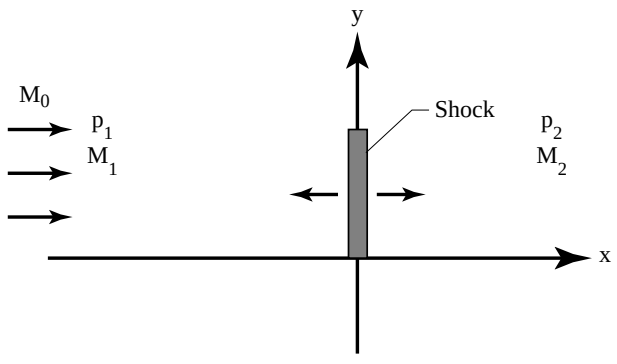

Figure 6. Shock oscillation used in determination of source term.

Considering for now only $\Delta(\partial T_{11}/\partial x)$,

$$\Delta\left(\frac{\partial T_{11}}{\partial x}\right) = \left.\frac{\partial T_{11}}{\partial x}\right|_2 - \left.\frac{\partial T_{11}}{\partial x}\right|_1$$

$$= \frac{\partial}{\partial x}\left(\rho_2 c_2^2 M_2^2 + p_2 - \rho_2 c_\infty^2\right) - \frac{\partial}{\partial x}\left(\rho_1 c_1^2 M_1^2 + p_1 - \rho_1 c_\infty^2\right)$$

$$\approx \left(c_2^2 M_2^2 - c_\infty^2\right)\frac{\partial \rho_2}{\partial x} + 2\rho_2 c_2 M_2 \frac{\partial (c_2 M_2)}{\partial x} + \frac{\partial p_2}{\partial x} - 2\rho_1 c_1^2 M_1 \frac{\partial M_1}{\partial x} \tag{11}$$

because ρ_1, p_1, and c_1 are, to first order, constant.

To evaluate equation (11) in terms of the upstream density, sound speed, and Mach number, the well-known shock jump relations are used. (See ref. 10.) These relations are presented for completeness. The second equality refers to an ideal gas with the ratio of specific heats, $\gamma = 1.4$.

$$\frac{p_2}{p_1} - \frac{2\gamma M_1^2 - (\gamma - 1)}{\gamma + 1} = \frac{7M_1^2 - 1}{6} \tag{12}$$

$$\frac{\rho_2}{\rho_1} = \frac{(\gamma + 1)M_1^2}{(\gamma - 1)M_1^2 + 2} = \frac{6M_1^2}{M_1^2 + 5} \tag{13}$$

$$\frac{u_2}{u_1} = \frac{(\gamma - 1)M_1^2 + 2}{(\gamma + 1)M_1^2} = \frac{M_1^2 + 5}{6M_1^2} \tag{14}$$

To compute the monopole source term of Lighthill's equation, the derivatives of the downstream pressure, density, and velocity are required. Taking the first derivative with respect to x, for the case of $\gamma = 1.4$, results in

$$\frac{\partial p_2}{\partial x} = \frac{7}{3} p_1 M_1 \frac{\partial M_1}{\partial x} = \frac{5}{3}\rho_1 c_1^2 M_1 \frac{\partial M_1}{\partial x} \tag{15}$$

$$\frac{\partial (c_2 M_2)}{\partial x} = \frac{c_1}{6}\frac{k(M_1^2 - 5)}{M_1^2}\frac{\partial M_1}{\partial x} \tag{16}$$

$$\frac{\partial \rho_2}{\partial x} = 60\rho_1 \frac{M_1}{\left(5 + M_1^2\right)^2}\frac{\partial M_1}{\partial x} \tag{17}$$

where $\partial M_1/\partial x = -M_s k \sin(\omega t - kx)$.

Substituting equations (12), (13), and (14) into equation (11) results in

$$\Delta\left(\frac{\partial T_{11}}{\partial x}\right) = -60\rho_1 c_\infty^2 \frac{M_1}{\left(M_1^2 + 5\right)^2}\frac{\partial M_1}{\partial x}$$

$$= -60\rho_1 c_\infty^2 \frac{M_1 M_s k}{\left(M_1^2 + 5\right)^2}\sin(\omega t - kx) \tag{18}$$

Substituting $M_1 = M_0 - M_s \cos(\omega t - kx)$ and keeping only terms of order M_s, results in

$$\Delta\left(\frac{\partial T_{11}}{\partial x}\right) = 60\rho_1 c_\infty^2 \frac{M_0 M_s k}{\left(M_0^2 + 5\right)^2} \sin(\omega t - kx) \tag{19}$$

Equation (19), normalized by $60\rho_1 c_\infty^2 k \sin(\omega t - kx)$, is plotted as a function of M_0 (for constant wave number) in figure 6.

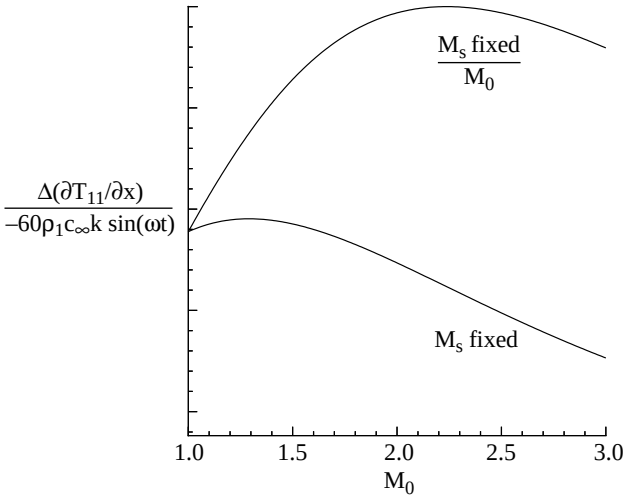

Figure 7. Normalized monopole component of source term sound generated by sinusoidally oscillating shock.

Two cases are shown in this figure. One curve represents the source term when the ratio of perturbation Mach number to upstream Mach number M/M_0 is held fixed. The other curve represents the source term for a fixed perturbation Mach number M_s. Clearly, the monopole source term of Lighthill's equation reaches a maximum value. To determine the exact location at which it maximizes, the first derivative of equation (18) with respect to M_0 is determined and set equal to zero. The value of M_0 for which this derivative is zero, when M is fixed, is found to be $M_0 = \sqrt{5/3} \approx 1.29$. The value of M_1 for which $(\partial/\partial M_0)\Delta(\partial T_{11}/\partial x) = 0$, when M/M_0 is fixed, is found to be $M_0 = \sqrt{5} \approx 2.24$.

Thus, the monopole source term reaches a maximum when, for constant shock velocity amplitude and constant disturbance wave number, $M_0 = \sqrt{5/3}$. When the ratio of the shock velocity amplitude to the presoak Mach number is held constant, the source term maximizes at $M_0 = \sqrt{5}$ for a fixed wave number.

For an acoustic disturbance, the wave number varies with upstream Mach number,

$$\begin{aligned} k &= \frac{\omega}{c_1(1 + M_1)} \\ &= \frac{\omega}{c_1(1 + M_0)} + \frac{\cos(kx - \omega t)}{(1 + M_0)^2} M_s + O(M_s)^2 \end{aligned} \tag{20}$$

The wave number may be approximated by $k = \omega/c_1(1 + M_0)$ and substituted into equation (19) while maintaining a truncation error of the order of $(M_s)^2$. Furthermore, if the sound speed approaching infinity is taken to be the stagnation sound speed, the relationship between c_1 and c_∞ is

$$\begin{aligned} c_1 &= c_\infty \sqrt{\frac{5}{5 + M_1^2}} \\ &= c_\infty \sqrt{\frac{5}{5 + M_0^2}} \left[1 + \frac{M_0 \cos(\omega t - kx)}{5 + M_0^2} M_s \right] + O\left(M_s^2\right) \end{aligned} \tag{21}$$

Thus, the monopole source term for $k = k(M_0)$ is

$$\Delta\left(\frac{\partial T_{11}}{\partial x}\right) = \frac{-60\rho_1 c_\infty \omega M_0 M_s \sin(\omega t - kx)}{\sqrt{5}\left(M_0^2 + 5\right)^{3/2} 1 + M_0} \tag{22}$$

Equation (22) normalized by $-60\rho_1 c_\infty \omega M_s \sin(\omega t - kx)$ is plotted in figure 8.

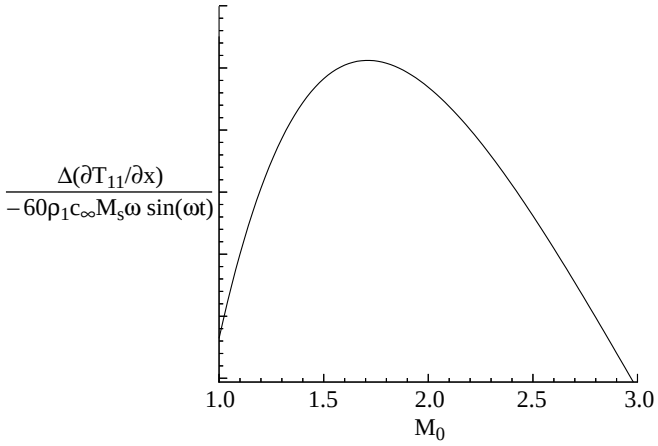

Figure 8. Normalized strength of monopole component of source term for sinusoidally oscillating shock.

Dipole source term. Consider now the dipole term of equation (8). This term can be written

$$\frac{\partial}{\partial x}[\Delta T_{11}\delta(x - x_x)] = \Delta T_{11}\delta'(x - x_s) \tag{23}$$

since the jump across the shock is not a function of x. Thus, the jump in T_{11} is of interest.

$$\Delta T_{11} = \rho_2 u_2^2 + p_2 - \rho_2 c_\infty^2 - \left(\rho_1 u_1^2 + p_1 - \rho_1 c_\infty^2\right) \tag{24}$$

But, from the unsteady jump relations (see appendix A for derivation)

$$\begin{aligned} \rho_2(u_2 - u_s) &= \rho_1(u_1 - u_s) \\ \rho_2 u_2(u_2 - u_s) + p_2 &= \rho_1 u_1(u_1 - u_s) + p_1 \end{aligned} \tag{25}$$

The change in pressure across the shock can be found with

$$p_2 - p_1 = \rho_1(u_1 - u_s)(u_1 - u_2) \tag{26}$$

Substituting equation (26) into equation (24) and neglecting higher order terms in u_s, results in

$$\Delta T_{11} \approx -(\rho_2 - \rho_1)c_\infty^2 \tag{27}$$

Therefore, upon substitution of equation (13) into equation (27) and simplification, the following expression for the dipole source term is obtained:

$$\Delta T_{11} = -5\rho_1 c_\infty^2 \left(\frac{M_1^2 - 1}{M_1^2 + 5} \right) \tag{28}$$

Substituting $M_1 = M_0 - M_s \cos(\omega t - kx)$ into equation (28) and neglecting terms of order M_s^2 and higher, results in

$$\Delta T_{11} = \frac{-5\rho_1 c_\infty^2}{M_0^2 + 5} \left[(M_0^2 - 1) - \frac{12 M_s M_0 \cos(\omega t - kx)}{M_0^2 + 5} \right] \tag{29}$$

Unlike the monopole term, the dipole term contains both zeroth and first order terms in M_s. Also, the wave number affects both the amplitude and the phase of the monopole term, while it affects only the phase of the dipole term. However, the monopole term and the first order component of the dipole term are identical except for the phase and the multiplicative factor of the wave number.

In figure 9, there are no local extrema for the dipole source term when the flow is supersonic. This lack of extrema can be verified analytically by taking the derivative of equation (28) with respect to M_0 as for the monopole case.

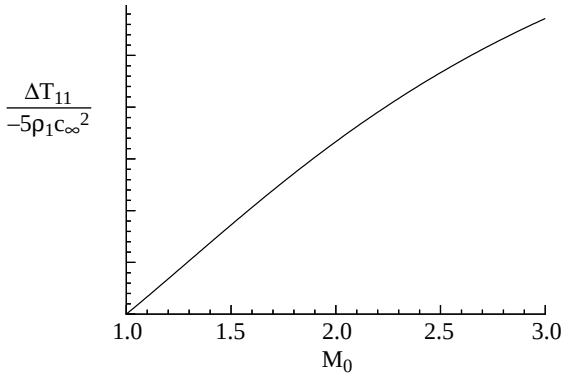

Figure 9. Normalized strength of dipole component of source term for sinusoidally oscillating shock.

Quadrupole source term. Finally, consider the quadrupole component of equation (8). The quadrupole term requires that the second ordinary derivative of the stress tensor component T_{11} with respect to x be evaluated. Thus,

$$\begin{aligned} \frac{\partial^2 T_{11}}{\partial x^2} &= \frac{\partial}{\partial x}\left(2\rho u \frac{\partial u}{\partial x} + u^2 \frac{\partial \rho}{\partial x} + \frac{\partial p}{\partial x} - c_\infty^2 \frac{\partial \rho}{\partial x} \right) \\ &= 2\rho u \frac{\partial^2 u}{\partial x^2} + 4u \frac{\partial u}{\partial x}\frac{\partial \rho}{\partial x} + 2\rho \left(\frac{\partial u}{\partial x} \right)^2 + (u^2 - c_\infty^2)\frac{\partial^2 \rho}{\partial x^2} + \frac{\partial^2 p}{\partial x^2} \end{aligned} \tag{30}$$

The evaluation of equation (30) upstream of the shock is simple, since the derivatives in p, ρ, and c are high order and hence can be neglected. The evaluation of equation (30) upstream is

$$\left.\frac{\partial^2 T_{11}}{\partial x^2}\right|_1 = 2\rho_1 c_1^2\left[\left(\frac{\partial M_1}{\partial x}\right)^2 + M_1\frac{\partial^2 M_1}{\partial x^2}\right] \tag{31}$$

Substituting $M_1 = M_0 - M_s\cos(\omega t - kx)$ and neglecting higher order terms in M_s, this expression reduces to

$$\left.\frac{\partial^2 T_{11}}{\partial x^2}\right|_1 = 10\rho_1 c_\infty^2 k^2\frac{M_0 M_s\cos(\omega t - kx)}{5 + M_0^2} \tag{32}$$

For an acoustic upstream disturbance for which the wave number is a function of Mach number, this becomes

$$\left.\frac{\partial^2 T_{11}}{\partial x^2}\right|_1 = 2\rho_1\omega^2\frac{M_0 M_s\cos(\omega t - kx)}{\left(5 + M_0^2\right)(1 + M_0)^2} \tag{33}$$

The evaluation of the quadrupole term downstream of the shock is more complicated since the second derivatives with respect to x of ρ_2, u_2, and p_2 are required. The second derivatives of the variables in equations (12), (13), and (14) are

$$\frac{\partial^2\rho_2}{\partial x^2} = \frac{60\rho_1}{\left(5 + M_1^2\right)^3}\left[5 - 3M_1^2\left(\frac{\partial M_1}{\partial x}\right)^2 + \left(5M_1 + M_1^3\right)\frac{\partial^2 M_1}{\partial x^2}\right] \tag{34}$$

$$\frac{\partial^2 p_2}{\partial x^2} = \frac{5}{3}c_1^2\rho_1\left[\left(\frac{\partial M_1}{\partial x}\right)^2 + M_1\frac{\partial^2 M_1}{\partial x^2}\right] \tag{35}$$

$$\frac{\partial^2 u_2}{\partial x^2} = \frac{c_1}{6M_1^3}\left[10\left(\frac{\partial M_1}{\partial x}\right)^2 - \left(5M_1 - M_1^3\right)\frac{\partial^2 M_1}{\partial x^2}\right] \tag{36}$$

where $\partial M_1/\partial x = -kM_s\sin(\omega t - kx)$, and $\partial^2 M_1/\partial x^2 = k^2 M_s\cos(\omega t - kx)$. Substituting equations (35), (34), and (36) into equation (30) provides

$$\left.\frac{\partial^2 T_{11}}{\partial x^2}\right|_2 = 2\rho_1 c_1^2\left[\left(\frac{\partial M_1}{\partial x}\right)^2 + M_1\frac{\partial^2 M_1}{\partial x^2}\right] + 12\rho_1 c_\infty^2\left[\frac{M_1^4 + 20M_1^2 - 25}{\left(5 + M_1^2\right)^3}\right]\left(\frac{\partial M_1}{\partial x}\right)^2 + 12\rho_1 c_\infty^2\left[\frac{-5M_1}{\left(5 + M_1^2\right)^2}\right]\frac{\partial^2 M_1}{\partial x^2} \tag{37}$$

Substituting $M_1 = M_0 - M_s\cos(\omega t - kx)$ and neglecting higher order terms results in

$$\left.\frac{\partial^2 T_{11}}{\partial x^2}\right|_2 = 10\rho_1 c_\infty^2 k^2\frac{M_0 M_s}{\left(5 + M_0^2\right)^2}\left(M_0^2 - 1\right)\cos(\omega t - kx) \tag{38}$$

Substituting in equation (20) for $k = k(M_0)$, the quadrupole term becomes

$$\left.\frac{\partial^2 T_{11}}{\partial x^2}\right|_2 = 10\rho_1\omega^2 \frac{M_0 M_s}{\left(5 + M_0^2\right)1 + M_0}(M_1 - 1)\cos(\omega t - kx) \tag{39}$$

Note that the quadrupole source term contains only first order terms (and higher) in M_s and goes to zero as $M_0 \to 1$. Also note that the quadrupole and dipole source terms have the same phase.

Evaluation of Acoustic Pressure

The previous section describes expressions for the monopole, dipole, and quadrupole source terms of Lighthill's equation for shock motion in one dimension. To make statements regarding the relative importance of these components to the far field sound, Green's function is used to solve for the far field acoustic pressure. For this analysis, it is assumed that only the first order terms in perturbation Mach number M_s are necessary to determine the relative importance of the monopole, dipole, and quadrupole terms, that the observer is located in the far field, and that the shock is a finite disk in a plug flow (fig. 10). The flow outside the plug is ambient and is characterized by the density ρ_∞ and the sound speed c_∞. For the analysis presented here, contributions of the interface between the plug flow and ambient medium to the far field sound are also neglected.

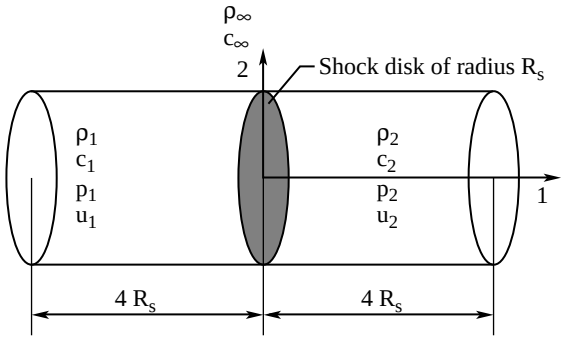

Figure 10. Shock disk in plug flow.

Pressure From Monopole Source

To evaluate the far field sound that results from the monopole source, a cylindrical coordinate system is set up with the origin at the shock disk center (fig. 11). The position of the source point along the disk is denoted by **y** and the position to the observer is denoted by **x**. The magnitude of the vector connecting the source point and the observer point $\mathbf{R} = \mathbf{x} - \mathbf{y}$ is denoted by R and is determined by geometrical arguments to be

$$R = \sqrt{r_0^2 + \sigma^2 - 2r_0\sigma \sin\theta \cos(\phi - \chi)} \tag{40}$$

where r is the radial coordinate, σ is the radial coordinate to the source point, ϕ is the observer angle about the axis of symmetry, and χ is the angle to the source point in the plane of the shock disk.

Making the far field approximation $\sigma^2/r_0^2 \to 0$ and employing the binomial expansion, this simplifies to

$$R \approx r_0\left[1 - \frac{\sigma}{r_0}\sin\theta \cos(\phi - \chi)\right] \tag{41}$$

where r_0 is the distance from the observer to the center of the shock, σ is the radial coordinate to the source point, θ is the angle from the jet axis to the observer, ϕ is the observer angle about the axis of

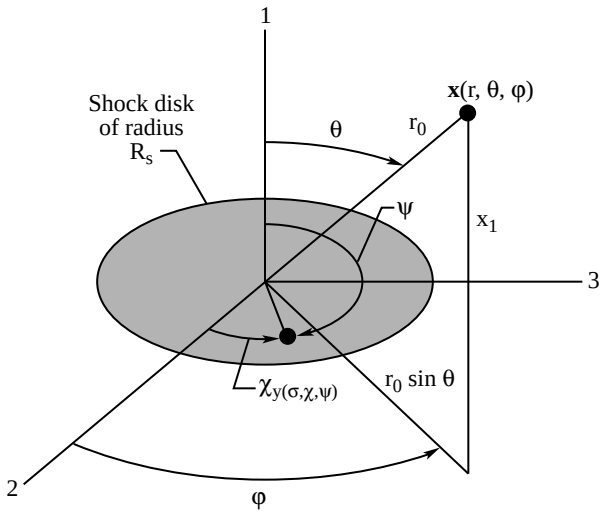

Figure 11. Coordinate system used in evaluation of surface integrals.

symmetry, and χ is the angle to the source point in the plane of the shock disk (fig. 11). To solve for the far field acoustic pressure from the monopole component of the source term of Lighthill's equation, the source term is multiplied by the free space Green's function and integrated over the source volume V and time τ

$$p_M(\mathbf{x},t) = \frac{-1}{4\pi}\int_V\int_\tau 60\rho_1 c_\infty^2 \frac{M_0 M_s k}{\left(M_0^2+5\right)^2}\sin(\omega\tau - ky_1)\delta(y_1 - y_{1s})\frac{\delta\left(\tau - t + \frac{R}{c_\infty}\right)}{R}\,dV\,d\tau \tag{42}$$

where $y_{1s} = 0$ is the shock position, and $dV = dy_1\sigma\,d\sigma\,d\chi$ is the incremental volume. Making the far field assumption that $1/R \approx 1/r_0$, and integrating over y_1,

$$p_M(\mathbf{x},t) = \frac{-1}{4\pi r_0}\int_{A_s}\int_\tau 60\rho_1 c_\infty^2 \frac{M_0 M_s k}{\left(M_0^2+5\right)^2}\sin(\omega\tau - ky_{1s})\delta\left(\tau - t - \frac{R}{c_\infty}\right)dA_s\,d\tau \tag{43}$$

where A_s is the shock area. Integrating over source time τ,

$$p_M(\mathbf{x},t) = \frac{-1}{4\pi r_0}\int_{A_s} 60\rho_1 c_\infty^2 \frac{M_0 M_s k}{\left(M_0^2+5\right)^2}\sin\left(\omega t - \frac{R}{c_\infty} - ky_{1s}\right)dA_s$$

$$= \frac{-60\rho_1 c_\infty^2}{4\pi r_0}\frac{M_0 M_s k}{\left(M_0^2+5\right)^2}\int_0^{R_s}\int_0^{2\pi}\sin\left\{\omega t - \left[r_0 - \frac{\sigma\sin\theta\cos(\phi-\chi)}{c_\infty - ky_{1s}}\right]\right\}\sigma\,d\sigma\,d\chi \tag{44}$$

Integrating with the aid of expressions 3.719-2 and 3.715-13 in reference 11, the analytical expression for the monopole source pressure is

$$p_M(x,t) = \frac{-30\rho_1 c_\infty^3 k M_0 M_s}{\left(M_0^2+5\right)^2 r_0}\frac{R_s}{\omega\sin\theta}J_1\left(R_s\sin\theta\frac{\omega}{c_\infty}\right)\sin\left(\omega t - \frac{\omega r_0}{c_\infty}\right) \tag{45}$$

where J_1 is the first order Bessel function of the first kind.

Pressure From Dipole Source

Again using the Green's function approach to solve for the pressure due to the dipole component of the source term in Lighthill's equation

$$p_D(\mathbf{x},t) = \frac{1}{4\pi}\int_V \int_\tau \frac{-5\rho_1 c_\infty^2\left(M_0^2-1\right)}{\left(M_0^2+5\right)^2}\delta'(y_1-y_{1s})\frac{\delta\left(\tau-t+\frac{R}{c_\infty}\right)}{R}$$

$$+\frac{60\rho_1 c_\infty^2 M_s M_0}{\left(M_0^2+5\right)^2}\cos(\omega\tau-ky_1)\delta'(y_1-y_{1s})\frac{\delta\left(\tau-t+\frac{R}{c_\infty}\right)}{R}\,dV\,d\tau \tag{46}$$

Making the far field approximation $1/R \approx 1/r_0$, integrating the first term over τ, and using the fact that (ref. 9)

$$\int f(y_1)\delta'(y_1-y_{1s})\,dy_1 = -\left(\frac{df}{dy_1}\right)_{y_{1s}} \tag{47}$$

The integral of the first term goes to zero. Making the far field approximation and integrating the second term over τ yields

$$p_D(\mathbf{x},t) = \frac{1}{r_0}\int_V \frac{60\rho_1 c_\infty^2 M_s M_0}{\left(M_0^2+5\right)^2}\cos\left[\omega\left(t-\frac{R}{c_\infty}\right)-k_{y1}\right]\delta'(y_1-y_{1s})\,dV \tag{48}$$

Integrating over y_1 with equation (47) results in

$$p_D(\mathbf{x},t) = \frac{1}{r_0}\frac{60\rho_1 c_\infty^2 M_s M_0}{\left(M_0^2+5\right)^2}\int_{A_s} -\frac{d}{dy_1}\left\{\cos\left[\omega\left(t-\frac{R}{c_\infty}\right)-ky_1\right]\right\}\Bigg|_{y_1=0} dA_s$$

$$= \frac{1}{r_0}\frac{60\rho_1 c_\infty^2 M_s M_0}{\left(M_0^2+5\right)^2}\int_{A_s}\sin\left[\omega\left(t-\frac{R}{c_\infty}\right)-ky_1\right]\left(-k-\frac{\omega}{c_\infty}\frac{\partial R}{\partial y_1}\right)dA_s \tag{49}$$

where $\partial R/\partial y_1 = -\cos\theta$ and $dA_s = \sigma\, d\sigma\, d\chi$. Integrating over the shock area, the expression for the dipole source contribution to the far field sound is

$$p_D(\mathbf{x},t) = \frac{-30\rho_1 c_\infty^3 M_s M_0}{\left(M_0^2+5\right)^2 r_0}\left(k-\frac{\omega}{c_\infty}\cos\theta\right)\sin\left[\omega\left(t-\frac{r_0}{c_\infty}\right)\right]\frac{R_s}{\omega\sin\theta}J_1\left(\frac{R_s\omega\sin\theta}{c_\infty}\right) \tag{50}$$

Note that

$$p_D(\mathbf{x},t) = p_M(\mathbf{x},t)\left(1-\frac{\omega\cos\theta}{c_\infty k}\right) \tag{51}$$

Pressure From Quadrupole Source

Using Green's function, the contribution of the downstream part of the quadrupole source term to the far field sound is

$$p_Q(\mathbf{x},t) = \int_V \int_\tau 10\rho_1 c_\infty^2 k^2 \frac{M_0 M_s \left(M_0^2 - 1\right)}{\left(M_0^2 + 5\right)^2} \frac{\delta\left(\tau - t + \frac{R}{c_\infty}\right)}{R} \cos(\omega\tau - k y_1)\, dV\, d\tau \tag{52}$$

where $R = \sqrt{r_0^2 + y_1^2 + \sigma^2 - 2r_0 y_1 \cos\theta - 2r_0\sigma \sin\theta \cos\chi}$. Making the far field approximation that $\sigma^2/r_0^2 \approx 0$ and $y_1^2/r_0^2 \approx 0$ and using the binomial expansion $R \approx r_0[1 - (y_1/r_0)\cos\theta - (\sigma/r_0)\sin\theta\cos\chi]$. Note that in integrating the quadrupole term, the integral is over the entire source volume since there are no delta functions that limit the integral to the surface. The integration over the entire source volume provides a challenge for this model because integrating over an infinite volume does not correspond to physical jet flows. Therefore, for this analysis, the volume term is limited to a length $-4R_s \le y_1 \le 4R_s$ along the axial coordinate. This range is selected to approximately correspond to average shock spacing in supersonic nozzles (ref. 12). Therefore, for integration of the downstream quadrupole term, the integration limits are $0 \le y_1 \le 4R_s$. Attempts at obtaining an analytical expression for this integral were unsuccessful. Therefore, numerical integration is used to evaluate the quadrupole term.

To simplify the comparisons and to isolate the sound generated downstream of the sound field, only the region downstream of the shock is considered in the volume integration. For the purposes of determining the relative importance of the monopole, dipole, and quadrupole terms it is also assumed that the source is compact. That is, the wavelength of the sound is large compared with the source size. This use of the compact assumption allows an analytical expression for the quadrupole term to be obtained, since R in the argument of the cosine term in equation (52) reduces to r_0.

Employing the compact source assumption, the analytical expressions for the monopole, dipole, and quadrupole terms are found to be

$$p_M(\mathbf{x},t) = \frac{-15\rho_1 c_\infty^2 k A_s M_0 M_s}{\left(M_0^2 + 5\right)^2 r_0 \pi} \sin\left(\omega t - \frac{\omega r_0}{c_\infty}\right) \tag{53}$$

$$p_D(\mathbf{x},t) = p_M(\mathbf{x},t)\left(1 - \frac{\omega \cos\theta}{c_\infty k}\right) \tag{54}$$

$$p_Q(\mathbf{x},t) = \frac{-5\rho_1 c_\infty^2 k A_s M_0 M_s}{\left(M_0^2 + 5\right)^2 r_0 \pi} (M_0^2 - 1) \sin(kR_s) \cos\left(\omega t - \frac{\omega r_0}{c_\infty} - kR_s\right) \tag{55}$$

Figure 12 shows the normalized acoustic root-mean-square pressure of the monopole, dipole, and quadrupole terms for an observer located 100 shock disk radii ($r_0 = 100$) away from the mean shock position at an angle of $\theta = \pi/4$ from the jet axis. For ease of comparison, the root-mean-square pressure is normalized by the constant multiplicative factor of the monopole, dipole, and quadrupole pressure terms

$$\frac{15\rho_1 c_\infty^2 k A_s M_0 M_s}{\pi r_0 \left(M_0^2 + 5\right)^2}$$

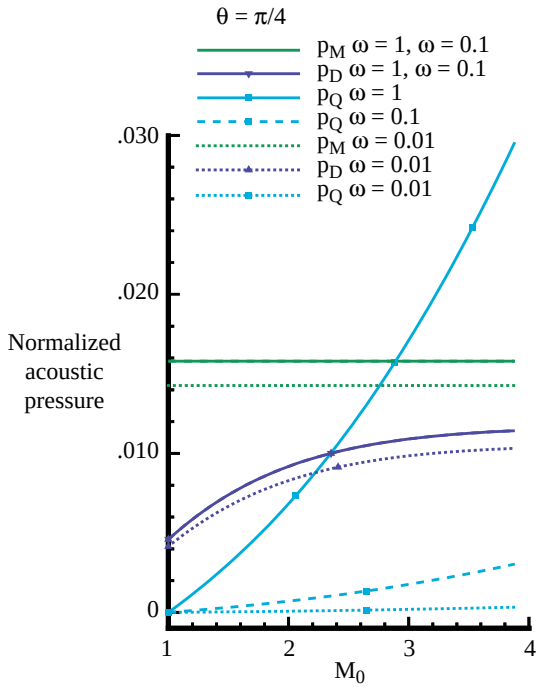

Figure 12. Far field pressure of monopole, dipole, and quadrupole terms in the Lighthill's analysis of shock noise for three frequencies.

The flow variables are normalized with respect to the sound speed c_∞, the shock disk radius R_s, and the upstream density ρ_1. For these comparisons, the wave number k varies with the mean flow Mach number as described in equation (20). There are several features in figure 12. First, the quadrupole term increases with mean flow Mach number more rapidly with increasing frequency. The dipole terms increase with mean flow Mach number. The variation in the monopole terms is an order of magnitude smaller than the variation in the dipole terms. Although difficult to see on this scale, the monopole terms peak and then decrease with increasing Mach number. The monopole terms dominate for the low frequencies over the entire Mach number range and for the high frequency case at low Mach number. For the case $\omega = 1$, the quadrupole term begins to dominate at about $M_0 = 2.8$. At low frequencies (for which the source is highly compact), the contribution of the quadrupole terms is negligible over the Mach number range considered in the analysis. The wavelength of the sound is

$$\lambda = \frac{2\pi c_\infty \sqrt{5}(1 + M_0)}{\omega\sqrt{5 + M_0^2}} \tag{56}$$

Thus, low frequencies correspond to highly compact sources. For example for $\omega = 1$, the wavelength over the range of $1 \le M_0 \le 3$ is $11.5 \le \lambda \le 15$. The range of wavelengths is not much larger than the source size $4R_s = 4$, and the compact assumption begins to break down. The range of wavelength for a source frequency of $\omega = 0.1$ is $115 \le \lambda \le 150$ and the compact assumption is valid.

Figure 13 shows the effect of observer position on the root-mean-square pressure of the monopole, dipole, and quadrupole terms. The results shown are for an observer located at 100 shock disk radii away from the mean shock position, at angles of $\theta = 0$, $\pi/4$, and $\pi/2$ from the jet axis. The monopole and quadrupole terms are unaffected by the change in observer position. The term p_M at all observer positions shown changes only modestly about a value of approximately 0.016 and p_Q increases with mean flow Mach number from 0 at $M_0 = 1$ to approximately 0.003 at $M_0 = 3.8$. The dipole component is affected by the observer position. The dipole term is stronger at observer angles closely aligned to the

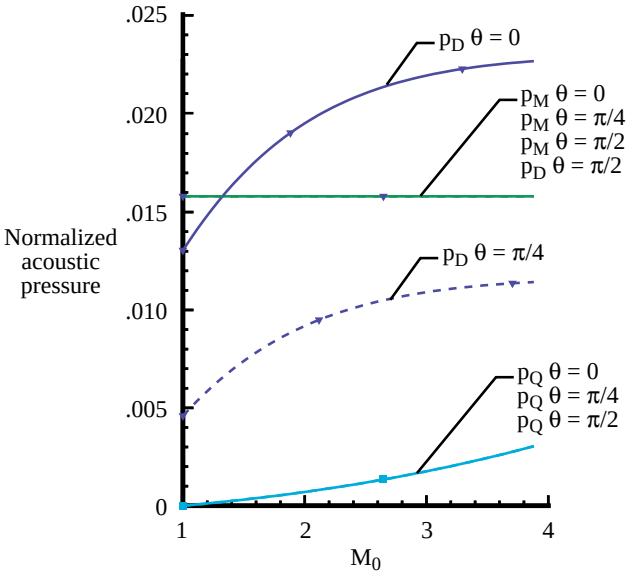

Figure 13. Field pressure of monopole, dipole, and quadrupole terms in the Lighthill's analysis of shock noise for three observer angles for $\omega = 0.1$.

jet axis, which is consistent with directivity patterns typical of dipoles. In addition, the dipole term reduces to the monopole term at an observer position of $\theta = \pi/2$.

Summary of Chapter 1

Detailed analysis and direct numerical simulation of the sound generated by realistic supersonic jet flows are currently impractical. To gain insight into the sound generating mechanisms of such a complicated flow structure, the elements considered to be essential to the sound-generation process are modeled. Four elements were identified: Flow past a wavy wall, vortex and vortex interaction, sound and shock interaction, and vortex and shock interaction. Because the focus of this work is on noise generation in shocked flows, the last two of these elements will be examined numerically in chapters 3 and 4.

This section presented an analysis of the source terms for Lighthill's equation for a model of an oscillating shock. The results presented for the acoustic pressure are accurate to first order in the perturbation Mach number and are valid only for an observer in the far field. The figures presented are valid for situations in which the source is compact. The analysis shows that the monopole, dipole, and quadrupole terms are all potentially important in shock noise generation. The term that dominates in a particular situation depends upon the observer position, the frequency, and the mean flow Mach number. For the cases tested here, the monopole term dominates for low frequencies over the entire range of Mach numbers studied. Both the monopole and dipole terms are significantly larger than the quadrupole term at low frequency. At high frequencies, the quadrupole term dominates at high Mach number.

Chapter 2

Numerical Methods and Issues

The direct simulation of sound generation in shocked flows is challenging because high accuracy is required to resolve the acoustic portion of the solution, while dissipation is required to maintain stability at the shock. Because shock-generated sound places high demands on the algorithm, care must be exercised in the selection of the scheme used in the simulations. Two algorithms are used in this report.

The first is MacCormack's scheme, which is second order accurate in time and space. It is used as a baseline in scheme comparisons because of its computational efficiency and simplicity. However, Gibbs' oscillations can occur in the vicinity of the moving shock, even with added artificial dissipation. MacCormack's scheme, as it is implemented in this work, is described in the introduction of the section entitled "Numerical Error Generated by a Slowly Moving Shock in a Duct."

The essentially nonoscillatory scheme is used in most of the calculations presented in this report. It was chosen because it allows for high-order accuracy in smooth regions of the flow while minimizing oscillations around discontinuities in the solution by adaptive stenciling. Second, third, fourth, and fifth order accurate implementations of the ENO scheme were used during the course of this research. The scheme is described in the section entitled "Analysis of Exact Solution."

The section "Extracting Acoustics From Aerodynamic Flow" examines the calculation of shocked flows. There is an additional oscillatory phenomenon which manifests itself when the shock wave is moving slowly relative to the mesh. This additional phenomenon has been observed and described and has been quantified for high-order schemes (refs. 13 and 14). Much of the content of this section has been published previously by the author, but is included here for completeness (ref. 14).

A high degree of accuracy is required to perform acoustic calculations. High accuracy can be obtained by using many cells (or grid points) in a low-order accurate scheme, or by using fewer cells (or grid points) in a higher order accurate scheme. A method of determining which approach is most economical is outlined in the section entitled "Economics of Higher Order Schemes." The result shows that the most economical approach depends on the degree of accuracy required. For acoustic calculations where the degree of accuracy required is on the order of 10^{-7}, the third order ENO scheme proves to be most economical. Hence, this is the scheme used in most of the calculations in chapters 4 and 5.

The section entitled "Extracting Acoustics From Aerodynamic Flow" presents information about the extraction of acoustic phenomena from aerodynamic flows. The separation of acoustics from aerodynamics cannot be performed in the near field, and thus the properties of acoustic waves in the far field are given. The implications of these properties on setting up and running a calculation for sound generation are then described. Some methods of analyzing the acoustics are provided.

Algorithms

MacCormack's Scheme

The classical MacCormack's scheme is employed in this research because it is efficient and has been used extensively in computational aeroacoustics (refs. 15, 16, and 17). MacCormack's scheme is described in many textbooks, but for completeness the algorithm is briefly outlined here (refs. 18 and 19).

Consider the system of hyperbolic equations

$$\frac{\partial \mathbf{U}}{\partial t} + \frac{\partial \mathbf{F}}{\partial x} = 0 \tag{57}$$

where $\mathbf{U}$ is a vector of J components, x is the streamwise direction coordinate, t is time, and $\mathbf{F}$ is a J component flux function of $\mathbf{U}$. A simple example of such a system of equations is the Euler equations. MacCormack's scheme approximates the solution to equation (57) by a two step predictor and corrector technique. For each component of the $\mathbf{U}$ vector, the predictor step is

$$\bar{\mathbf{U}}_j^{n+1} = \mathbf{U}_j^n - \frac{\Delta t}{\Delta x}\left(\mathbf{F}_{j+1}^n - \mathbf{F}_j^n\right) \tag{58}$$

and the corrector step is

$$\mathbf{U}_j^{n+1} = \frac{1}{2}\left[\mathbf{U}_j^n + \bar{\mathbf{U}}_j^{n+1} - \frac{\Delta t}{\Delta x}\left(\bar{\mathbf{F}}_j^n - \bar{\mathbf{F}}_{j-1}^n\right)\right] \tag{59}$$

where the superscript n represents the nth time level, the subscript j represents the jth cell, and $\bar{\mathbf{F}}$ represents the flux function $\mathbf{F}$ evaluated at the predictor value $\bar{\mathbf{U}}$.

MacCormack's scheme is second order accurate in space and time. Analysis of the stability of MacCormack's scheme with discussion about the amplification and dispersion factors can be found in textbooks such as references 18 and 19.

MacCormack's scheme as presented in equations (58) and (59) experiences difficulty maintaining stability when applied to shocked flows. Therefore, additional artificial dissipation is required. In this algorithm, artificial viscosity of the Jameson type is added to the right hand side of the predictor step (ref. 15). The corrected numerical flux is defined by

$$\mathbf{F}_{j+1}^n - \mathbf{F}_j^n - \mathbf{F}^{AV} \tag{60}$$

$$\mathbf{F}^{AV} = \varepsilon_{i+1/2}^{(2)}(\mathbf{U}_{i+1} - \mathbf{U}_i) - \varepsilon_{i+1/2}^{(4)}(\mathbf{U}_{i+2} - 3\mathbf{U}_{i+1} + 3\mathbf{U}_i - \mathbf{U}_{i-1}) \tag{61}$$

and

$$\begin{aligned} \varepsilon_{i+1/2}^{(2)} &= K^{(2)}(|u| + c)_i \max(\nu_i, \nu_{i+1}) \\ \varepsilon_{i+1/2}^{(4)} &= \max\left[0, K^{(4)}(|u| + c)_i - \varepsilon_{i+1/2}^{(2)}\right] \end{aligned} \tag{62}$$

where

$$\nu_i = \frac{|p_{i+1} - 2p_i + p_{i-1}|}{p_{i+1} + 2p_i + p_{i-1}} \tag{63}$$

Here p is the pressure, u is the flow velocity, and c is the speed of sound. In the calculations presented here, the coefficients are defined $K^{(2)} = 1/4$ and $K^{(4)} = 1/256$.

The pressure term in $\varepsilon^{(2)}$ is generally of second order in smooth regions of flow, the $\varepsilon^{(4)}$ term dominates, and the artificial dissipation is fourth order. Near discontinuities, however, the pressure term reduces to zeroth order, the $\varepsilon^{(2)}$ term dominates, and the artificial dissipation is second order.

MacCormack's scheme has numerical damping and dispersion properties since the stencils are used throughout the computation. The numerical properties of the scheme are documented in many textbooks (ref. 18).

Because the stencil that is used in the ENO scheme changes spatially as well as temporally, the damping and dispersion properties of the ENO scheme are a function of the particular calculation being performed. It is not possible to examine these error properties in the traditional manner. Therefore, discussion of the properties will focus on specific cases that were studied in this paper. For the reader interested in a more quantitative error analysis of the ENO scheme, a recent study of the difficulties in obtaining globally high-order-accurate solutions in the simulation of shock-induced sound is recommended (ref. 21).

ENO Scheme

The class of ENO schemes is chosen because high accuracy is achieved in smooth portions of the flow, while spurious oscillations around flow discontinuities such as shocks are bounded (ref. 22). A brief discussion of the properties of ENO schemes is given below, but interested readers are referred to references 22 and 23 for details.

An ENO solution operator E_h is rth order accurate in the sense of local truncation error

$$E_h U^n = U^{n+1} + O(h^{r+1}) \tag{64}$$

where $U(x)$ is the sufficiently smooth exact solution, and h is the cell spacing. The distinguishing property of ENO schemes is that spurious oscillations near discontinuities in U are bounded. For the one-dimensional scalar case, this can be written

$$TV(E_h U) = TV(U) + O(h^{1+q}) \tag{65}$$

for some $q > 0$, where $TV(U)$ is the total variation of U as a function of x, defined as $TV(U) = \sum_i |U_{i+1} - U_i|$ for a discrete solution to a scalar conservation law.

Bounding oscillations near discontinuities is accomplished in ENO schemes through an adaptive stencil. Because the stencil used for discretizing the differential equations adapts to the solution, schemes based on the ENO property may be thought of as adaptive filters or nonlinear algorithms.

The ENO schemes minimize numerical oscillations around discontinuities by using data from the smoothest part of the flow. At each cell, a searching algorithm determines which portion of the surrounding flow is smoothest. The stencil spanning this portion of the flow is then used to construct a higher order accurate, conservative interpolation to determine the variables at the cell interfaces.

In this particular finite-volume implementation, the interpolation operator is applied to the cell-averaged characteristic variables and the accuracy in space and time is third order. Time integration is accomplished by a third order, three stage Runge-Kutta scheme, which is discussed by Shu and Osher (ref. 23). The algorithm is applied to the conservation law form of the equations so that shocks are captured in the computations and no shock fitting is required to enforce the Rankine-Hugoniot jump relations across shocks that appear in the solution.

Stencil biasing parameters. The ENO schemes can achieve high-order accuracy in smooth regions and capture shocks without oscillations by adaptive stenciling. As the ENO schemes were originally presented in reference 22, the stencil shifts freely with any detection of a numerical gradient. The direction of the stencil shift is determined by the magnitudes of the neighboring divided differences. The stencil shifts away from the larger differences. However, a loss of accuracy can occur when this freely adaptive algorithm is used (refs. 24 and 25). Shu has suggested that the stencil be biased towards a preferred stencil, the one that makes the scheme stable in the sense of linear stability analysis (ref. 26). The stencil is allowed to shift only when one neighboring difference is larger than the other by some factor. This factor will be referred to as the “bias” parameter.

This biasing can be accomplished by implementing a factor in the search stencil. To explain how biasing is used to affect the stencil, let Δ_i^k denote the operator that yields the kth forward difference on a stencil of $k + 1$ cells with a left index i, which is defined recursively by

$$\begin{aligned} \Delta_i^1 \bar{u} &= \bar{u}_{i+1} - \bar{u}_i \\ \Delta_i^k \bar{u} &= \Delta_{i+1}^{k-1} \bar{u} - \Delta_i^{k-1} \bar{u} \qquad\qquad k = 2,3,\ldots \end{aligned} \tag{66}$$

The algorithm begins by setting $j^1(i) = i$. This one-cell stencil results in a piecewise constant reconstruction that is spatially first order accurate. To choose $j^{k+1}(i)$, $k = 1,...,r-1$, the two stencils considered as candidates are those obtained by annexing a cell to the left or right of the previously determined cell. The stencil that is selected is the one in which the kth difference is smaller in magnitude

$$j^{k+1}(i) = \begin{cases} j^k(i) - 1, & \text{if } \sigma_L \left|\Delta_L^k \bar{u}\right| < \sigma_R \left|\Delta_R^k \bar{u}\right| \\ j^k(i), & \text{otherwise} \end{cases} \tag{67}$$

where $\Delta_L^k \bar{u}$ and $\Delta_R^k \bar{u}$ are the kth differences obtained by annexing the cell to the left or right of the previously determined stencil, respectively, $(\sigma_L, \sigma_R) = (1, \bar{\sigma})$ or $(\bar{\sigma}, 1)$ for biasing to the left or right, respectively, with $\bar{\sigma} > 1$.

Even when a bias parameter is used, there may be a loss of accuracy when all the numerical gradients in a region are small; however, some are orders of magnitude larger than others. Atkins has suggested another parameter, which serves as a threshold, to force the shift to the preferred stencil whenever neighboring differences are small, regardless of their relative magnitudes (ref. 27). This parameter will be referred to as the threshold parameter.

The threshold parameter is implemented as

$$\text{if } \left|\Delta_L^k \bar{u}\right| < \varepsilon \text{ and } \left|\Delta_R^k \bar{u}\right| < \varepsilon \text{ then } j^{k+1}(i) = j_S^{k+1}(i) \tag{68}$$

where ε is a small parameter and $j_S^k(i)$ identifies the stencil obtained by annexing the kth cell in the linearly stable direction.

The results presented in this paper used the definitions cited in references 25 and 26.

ENO flux computation. The ENO schemes of the Godunov type rely upon the solution of the Riemann problem to calculate numerical fluxes. Two methods of computing the fluxes across the cell interfaces are evaluated in this report. The first method was developed by Roe and the second was developed by Osher and Solomon (refs. 28 and 29).

Consider a system of hyperbolic equations

$$\frac{\partial \mathbf{U}}{\partial t} + \frac{\partial \mathbf{F}}{\partial x} = 0 \tag{69}$$

where $\mathbf{U}$ is a vector of J components, t is time, x is the streamwise direction coordinate, and $\mathbf{F}$ is a J component differentiable function of $\mathbf{U}$.

Roe's approximate Riemann solver determines the change in flux by finding a mean Jacobian matrix $\tilde{A}$ which satisfies

$$\Delta \mathbf{F} = \tilde{A} \Delta \mathbf{U} \tag{70}$$

where Δ represents the difference between any two states in solution space. The matrix $\tilde{A}$ is required to have a complete set of right eigenvectors and reduce to the exact Jacobian matrix when the states to the left and the right are equal $\bar{A}(\mathbf{U},\mathbf{U}) = (\partial \mathbf{F}/\partial \mathbf{U})\mathbf{U}$. If $\tilde{\lambda}_{(j)}$, $\tilde{r}^{(j)}$, and δw_j are the jth eigenvalue, the right eigenvector, and the inner product of the jth left eigenvector with $\Delta \mathbf{U}$, respectively, equation (70) can be written

$$\Delta \mathbf{F} = \sum_{j=1}^{J} \tilde{r}^{(j)} \tilde{\lambda}_{(j)} \delta w_j \tag{71}$$

The flux at the cell interface is written

$$f = \frac{1}{2}(\mathbf{F}_L + \mathbf{F}_R) - \frac{1}{2}\sum_j \left|\tilde{\lambda}_{(j)}\right| \delta w_j \tilde{r}^{(j)} \tag{72}$$

where $\mathbf{F}_L$ and $\mathbf{F}_R$ are the values of the fluxes to the left and right of the interface, respectively. Roe gives the expressions for $\tilde{\lambda}$, $\tilde{r}$, and δw_j for the Euler equations in reference 28.

Osher's approximate Riemann solver computes fluxes in state space rather than physical space. The flux difference between the left and right states is written

$$\Delta\mathbf{F} = \int_{\mathbf{U}_L}^{\mathbf{U}_R} \frac{\partial \mathbf{F}}{\partial \mathbf{U}} \, d\mathbf{U} \tag{73}$$

where the integral is evaluated along an arbitrary path Γ in state space.

The flux at the cell interface is given by

$$f = \frac{1}{2}(\mathbf{F}_L + \mathbf{F}_R) - \frac{1}{2}\sum_j \int_{\Gamma(j)} \left|\lambda_{(j)}\right| r^{(j)} \, d\mathbf{U} \tag{74}$$

The evaluation of the integral in equation (74) requires knowledge of the states along each subpath $\Gamma(j)$ and any sonic states that occur. Osher and Solomon solve for these states explicitly for the Euler equations (ref. 29).

Numerical Error Generated by a Slowly Moving Shock in a Duct

Introduction

The numerical treatment of unsteady shocks is challenging. In addition to the usual concerns of stability and accuracy, there are conflicting requirements with the calculation of the shock region. While it is desirable to resolve the shock crisply by minimizing the smearing effect of artificial dissipation at the shock, some artificial dissipation is required at the shock to minimize or eliminate the oscillations that occur when attempting to resolve a discontinuity on a finite mesh. There is an additional oscillatory phenomenon that can manifest itself in the computation of slowly moving shocks. This additional oscillation that results from the unsteadiness slowly moving shocks is discussed in references 13, 30, and 31 and is investigated here to determine the nature of the spurious oscillations and the effect that these spurious oscillations have on computing sound.

To simplify the analysis and better isolate difficulties in the numerical calculations, only one-dimensional and quasi-one-dimensional flows will be treated here. Thus, vorticity waves will not appear and emphasis will be on predicting the acoustic and entropy waves. The model problem to be investigated is a shock moving at a constant velocity in a one-dimensional flow field.

Spurious oscillations in unsteady computations of slowly moving shocks have been described by Woodward and Colella, who observed the oscillations in computations of high-pressure ratio ($p_2/p_1 > 10^5$) shocks (ref. 30). These oscillations appear when the speed of the shock relative to the mesh is small compared to the maximum flow speed at the shock. Woodward and Colella suggested that additional numerical dissipation be added to the scheme at the shock and explained that the reason for this spurious numerical behavior is that the shock transition layer alternates between being thick and thin as it passes through the mesh.

Roberts has noted that the oscillation phenomenon is not observed in discontinuous solutions of scalar equations (ref. 13). Roberts explains the oscillation in terms of the discrete shock structure. He shows that among first order flux-difference splitting schemes, Osher's approximate Riemann solver provides the smallest oscillations because the unsteadiness of the numerical shock structure in state

space most closely approximates the true shock structure. Roberts observed the spurious oscillation phenomenon in calculations for shock pressure ratios as low as 1.2 in calculations that used first order flux-difference splitting schemes.

Lindquist and Giles observed spurious oscillations in computations that used a Jameson style Runge-Kutta scheme with blended second- and fourth-difference artificial dissipation and also with a van Leer flux vector splitting algorithm for shock pressure ratios $1.5 < p_2/p_1 < 2.1$ (ref. 31). They described the oscillations in terms of the changing shock shape as the shock traverses the computational mesh and found, as did Woodward and Colella, that the spurious oscillations could be reduced by smearing the shock over more computational cells.

Spurious oscillations have been observed during the course of this research in computations that used the classical MacCormack's scheme, a high-order accurate essentially nonoscillatory (ENO) scheme, and an implementation of Jameson's Runge-Kutta scheme, which employs a symmetric total variation diminishing (TVD) matrix dissipation. Because the interest here is to compute sound generated by shocks and shock and fluid interactions, artificial dissipation is not explicitly increased over the solution domain because of the deleterious effect on the generation and the propagation of sound in the solution. This lack of increase of artificial dissipation has created some difficulties because the spurious oscillations are preserved in the high-order accurate flow computations.

The ENO schemes of Godunov rely upon the Riemann solver for the calculation of numerical fluxes. The effect that two Riemann solvers have on the spurious oscillations will be described in this section. In addition, because ENO schemes use an adaptive stencil to reduce spurious oscillations, modifications of this adaptive procedure will be examined. Finally, the effects of shock pressure ratio, Courant number, grid spacing, and shock speed on the amplitude and the frequency of the spurious numerical oscillations will be described.

Analysis of Exact Solution

The governing equations for the inviscid, compressible flow in a constant area duct are assumed to be the one-dimensional Euler equations

$$\frac{\partial \mathbf{U}}{\partial t} + \frac{\partial \mathbf{F}}{\partial x} = 0 \tag{75}$$

where $\mathbf{U}$ is the vector of conserved variables $[\rho, \rho u, \rho e]^T$, t is time, x is streamwise direction coordinate, and $\mathbf{F}$ is the flux vector, $[\rho u, \rho u^2 + p, (\rho e + p)u]^T$ where ρ is density, u is velocity, e is total energy per unit mass, and p is pressure.

Consider these equations along the duct length $0 \le x \le L$ for $t > 0$ with the initial condition

$$\mathbf{U}(x,0) = \begin{cases} \mathbf{U}_1 & x < x_s \\ \mathbf{U}_2 & x > x_s \end{cases} \tag{76}$$

where the constant states 1 and 2 represent the flow upstream and downstream of a shock, respectively, and x_s is the shock position.

If these equations are integrated along the duct, then

$$\frac{d}{dt}\int_0^L \mathbf{U}\, dx + \mathbf{F}[\mathbf{U}(L,t)] - \mathbf{F}[\mathbf{U}(0,t)] = 0 \tag{77}$$

One solution is the trivial case, $\mathbf{U}_1 = \mathbf{U}_2$. The nontrivial solution to this equation with the initial condition as described in equation (75) is a flow field with a shock moving at constant velocity u_s, which satisfies

$$\mathbf{F}(\mathbf{U}_2) - \mathbf{F}(\mathbf{U}_1) = u_s(\mathbf{U}_2 - \mathbf{U}_1) \tag{78}$$

Equation (78) follows directly from equation (77) for constant area states on either side of the shock. The solution $\mathbf{U}_1 = \mathbf{U}_2$ also satisfies equation (78).

Results

The unsteady, compressible, inviscid flow in the duct is solved by numerical integration of the one-dimensional Euler equations. All variables in the supersonic flow field at the inflow boundary are prescribed. The static pressure at the downstream (subsonic) boundary is prescribed. Variables are normalized by the duct length, stagnation pressure, and stagnation sound speed. Control over the shock velocity is obtained by making a transformation $u = u - u_s$, where u_s is the prescribed shock velocity, so that a positive shock velocity moves the shock to the left of the computational domain.

Computations have been performed over a range of shock pressure ratios and shock speeds, but in the interest of brevity, only one typical calculation is shown here. The calculations were performed on a 512-cell grid at a Courant number of 1. Unless noted otherwise, calculations are performed using Roe's flux solver. Both the bias parameter and threshold parameter are "on," meaning that the stencil is biased towards the preferred one and a threshold limit is set. The values of the biasing parameters that were used in these calculations (eqs. (68) and (69)) are $\bar{\sigma} = 2$ and $\varepsilon = 10^{-3}$. Figure 14 illustrates the spurious oscillations observed with the third order ENO scheme for a case in which the pressure ratio across the shock is 10.33 and the shock is moving to the left at a speed of 0.05. Figure 14 shows the pressure and entropy distributions in the duct after the shock has moved 15 percent of the duct length. Entropy is measured by the quantity $s = p/\rho^{\gamma}$. Although there were no oscillations at the shock in the initial shock position, once the shock begins to move spurious waves develop in the flow solution. The oscillation is seen primarily in the entropy wave; the pressure wave is relatively unaffected.

The spurious error is due to the discrete motion of the shock moving through the mesh. When the shock is located at a cell interface, it is extremely thin. As it moves through the cell interior, it smears out, weakens in strength, and entropy and pressure waves convect downstream. If the shock-passing frequency is defined as the frequency associated with the shock passing through a cell

$$f_{\text{shock}} = \frac{u_s}{\Delta x} \tag{79}$$

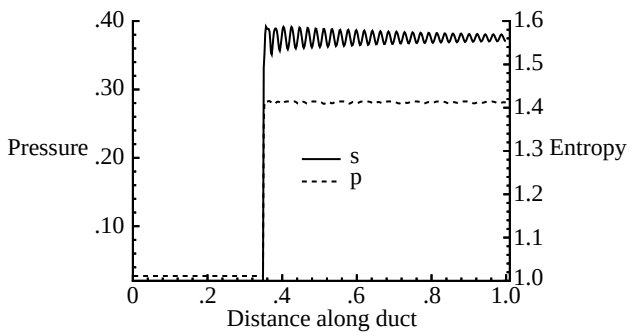

Figure 14. Pressure and entropy as functions of distance along duct. Shock speed = 0.05; shock pressure ratio = 10.33.

where Δx is the grid spacing and u_s is the shock speed relative to the grid. The wavelengths associated with the pressure and entropy waves λ_p and λ_s are determined by

$$\lambda_p = \frac{u_2 + a_2}{f_{\text{shock}}} = \frac{(u_2 + a_2)\Delta x}{u_s} \tag{80}$$

$$\lambda_s = \frac{u_2}{f_{\text{shock}}} = \frac{u_2 \Delta x}{u_s} \tag{81}$$

where u_2 and a_2 are the downstream velocity relative to the shock and sound speed, respectively. When adequately resolved on the mesh, the spurious pressure and entropy waves measured in the numerical computations compare well with the wavelengths λ_p and λ_s described by equations (80) and (81). For example, the wavelength λ_s of the entropy wave in figure 14 is computed as $\lambda_s \approx 0.550 \cdot 0.00195/0.05 \approx 0.021$. Inspection of figure 14 verifies this result.

A series of calculations for the same shock strength of $p_2/p_1 = 10.333$ illustrates the effect of shock speed on the behavior of the spurious oscillations. These calculations were performed on a 512-cell grid at a Courant number of 1.0. Figure 15 shows the entropy distributions in the tube after the shock has moved to the left for a normalized time of 3.0 for shock speeds of 0.02, 0.05, and 0.15. For clarity, the entropy distributions are offset by a constant value of 0.1. The entropy upstream of the shock is 1.0. The wavelengths of the perturbations downstream of the shock are consistent with equation (81). The long wavelength disturbances at the lowest shock speeds are only slightly damped downstream of the shock, while the short wavelength disturbances at high shock speeds are damped very quickly by the dissipation in the scheme. This, of course, explains why these disturbances are not seen when the shock speed through the mesh is comparable to the flow speed.

Figure 16 shows the pressure distributions in the tube after the shock has moved to the left for a normalized time of 3.0 for shock speeds of 0.02, 0.05, and 0.15. For clarity, the pressure distributions are offset by a constant value of 0.05. The pressure upstream of the shock is approximately 0.027. Small perturbations are visible in the pressure distribution downstream of the shock and the wavelengths of these perturbations are consistent with equation (81). The long wavelength disturbances at the lowest shock speeds are only slightly damped downstream of the shock, while the short wavelength disturbances at high shock speeds are damped very quickly by the dissipation in the scheme.

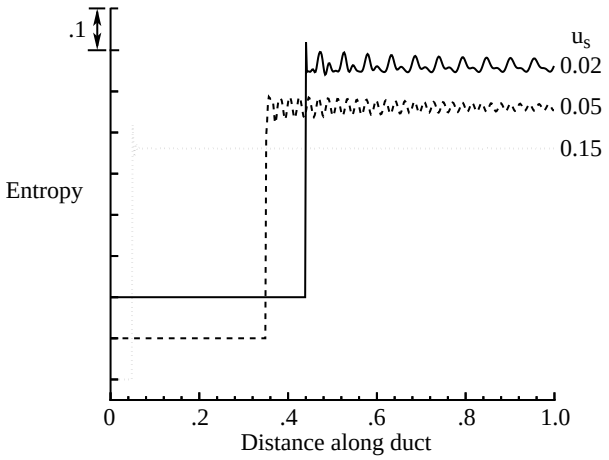

Figure 15. Entropy as a function of distance along duct and shock speed. Shock speed = 0.02, 0.05, and 0.15; shock pressure ratio = 10.33.

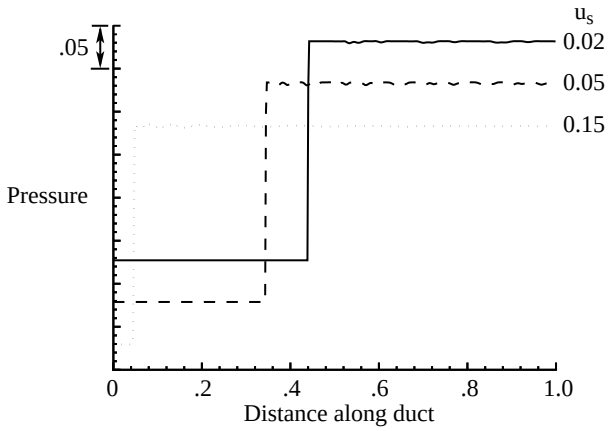

Figure 16. Pressure as a function of distance along duct and shock speed. Shock speed = 0.02, 0.05, and 0.15; shock pressure ratio = 10.33.

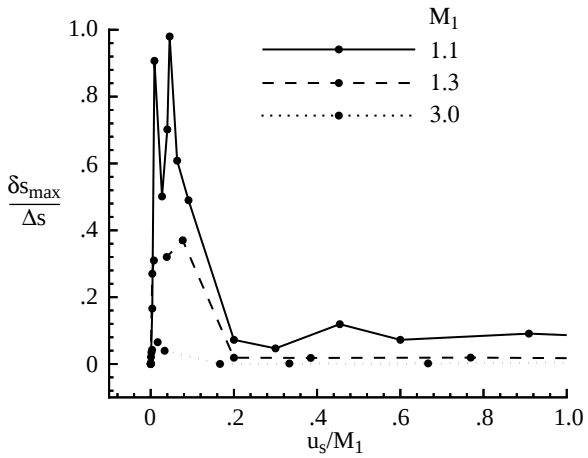

Figure 17. Effect of shock velocity on spurious entropy.

Effect of shock speed. Figure 17 summarizes the effect of the shock velocity relative to the grid on the maximum amplitude of the spurious entropy. The ratio of the magnitude of maximum zero-to-peak entropy error amplitude to the jump in entropy across the shock is plotted as a function of the ratio of the shock velocity (normalized by upstream stagnation sound speed) to upstream Mach number. These calculations were performed for a shock moving to the right at shock speeds from 0 to 5.0 on a 256-cell mesh. The spurious entropy amplitude is machine zero when the shock is stationary relative to the grid. The amplitude increases to a maximum when $0.005 < u_s/M < 0.1$ and decreases as the ratio of u_s/M increases further.

Figure 18 summarizes the effect of the shock velocity relative to the grid on the maximum amplitude of the spurious pressure. The ratio of the magnitude of maximum zero-to-peak pressure error amplitude to the shock strength is plotted as a function of the ratio of the shock velocity (normalized by upstream stagnation sound speed) to upstream Mach number. These calculations were performed for a shock moving to the right at shock speeds from 0 to 5.0 on a 256-cell mesh. The results show that the maximum pressure amplitude is relatively independent of the shock speed and that the maximum error in the downstream pressure relative to the shock strength is less than 0.15 percent for all cases studied.

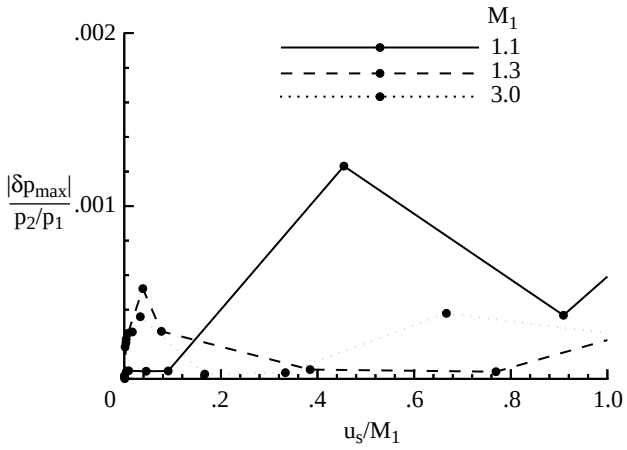

Figure 18. Effect of shock velocity on spurious pressure.

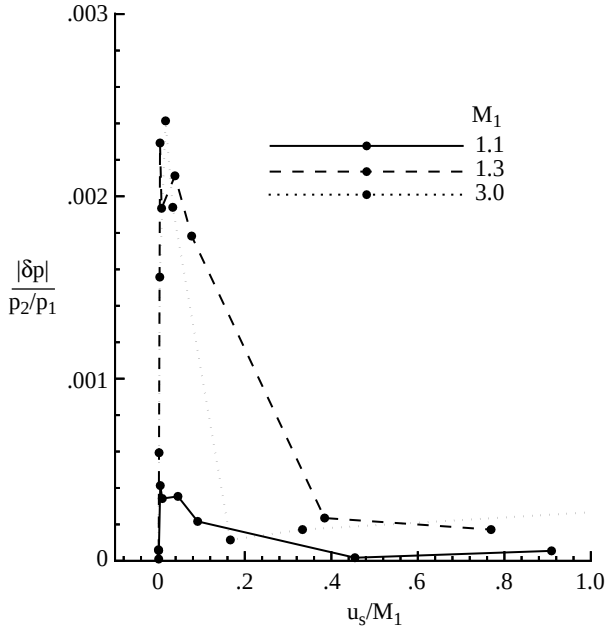

Figure 19. Effect of shock velocity on spurious pressure measured approximately 50 cells downstream of shock.

Figure 19 shows the zero-to-peak pressure error at a location approximately 50 cells downstream of the shock. This figure shows that for faster moving shocks, the amplitude of the pressure error is more rapidly damped. This rapid damping is consistent with the observations illustrated in figure 16, which relates the wavelength of the spurious pressure with the shock speed.

Because the amplitude of the error introduced by a slowly moving shock is manifest primarily in entropy, further discussion will focus on this flow variable in the section entitled “Effect of Stencil Biasing Parameters.”

Effect of shock strength. Figure 17 also illustrates that the magnitude of the maximum spurious entropy amplitude is a function of shock pressure ratio. As the shock strength increases, the magnitude of entropy error relative to the static entropy jump decreases. In the weak shock case $M = 1.1$, the spurious oscillations are close to 100 percent of the static jump in entropy over a range of shock speeds. This large percentage is because for the weak shock cases, the entropy jump across the shock is very small.

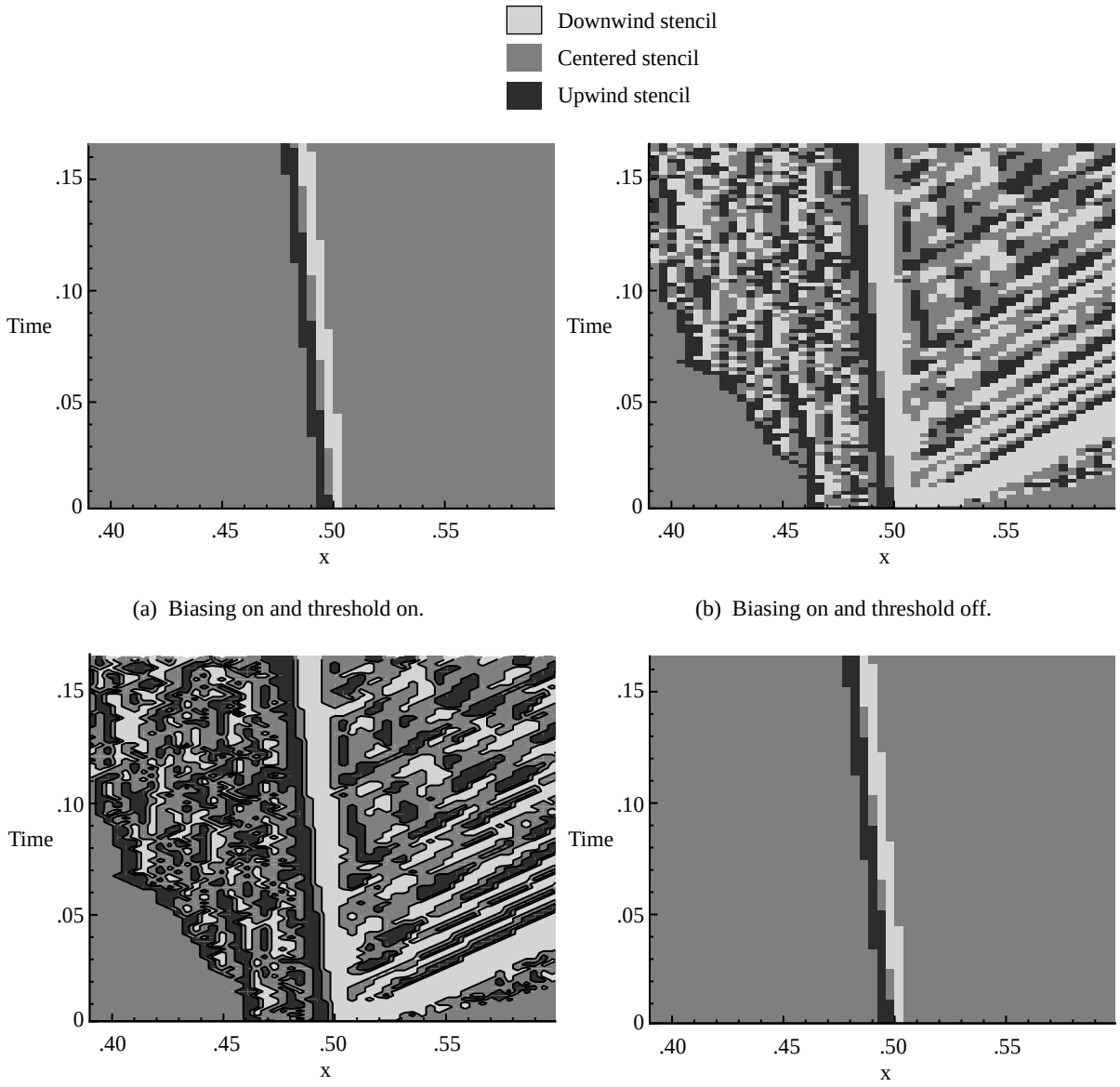

(a) Biasing on and threshold on.

(b) Biasing on and threshold off.

(c) Biasing off and threshold off.

(d) Biasing off and threshold on.

Figure 20. Effect of stencil-biasing parameter and threshold parameter on stencil for 256 cells.

The absolute levels of maximum entropy error are actually orders of magnitude higher for the higher Mach number flows. For example at $u_s/M = 0.04$, the absolute levels of maximum entropy error are $\delta s_{max} = 0.00033$, 0.0039, and 0.097 for Mach numbers $M = 1.1$, 1.3, and 3.0, respectively.

Effect of Courant number. A sequence of calculations was performed with Courant numbers between 0.1 and 1.0 (the stability limit) to determine the effect of Courant number on the spurious entropy. Neither the amplitude nor the wavelength of the spurious oscillations is found to be sensitive to the Courant number. This lack of sensitivity is consistent with the results reported by Roberts for flux-difference splitting schemes (ref. 13).

Effect of stencil biasing parameters. In this section the effects of the stencil biasing parameters on the spurious entropy are investigated. To illustrate the effects of these parameters on the algorithm, figure 20 shows a space and time diagram of the stencil that was used in the ENO algorithm for four

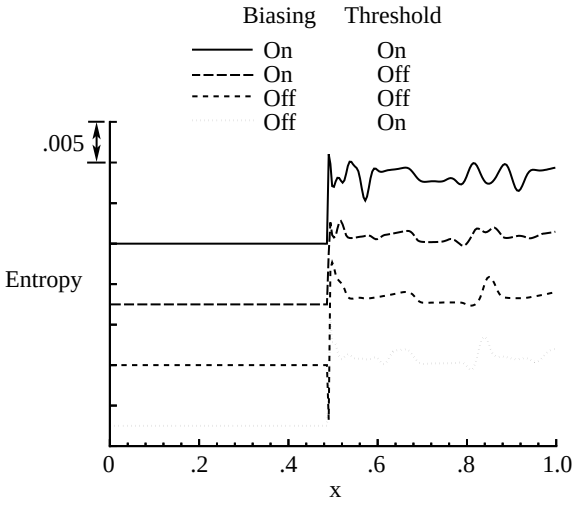

Figure 21. Entropy as a function of duct distance for combinations of biasing and threshold parameters for 256 cells.

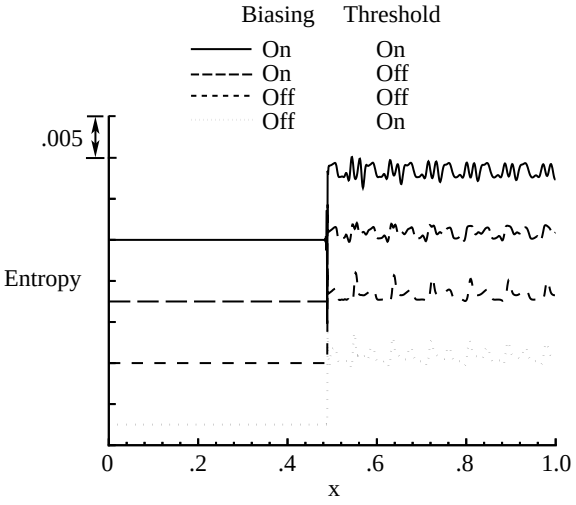

Figure 22. Entropy as a function of duct distance for combinations of biasing and threshold parameters for 1024 cells.

combinations of stencil biasing parameters. These combinations are (a) threshold on and bias on, (b) threshold off and bias on, (c) threshold off and bias off, and (d) threshold on and bias off. For clarity, the space and time diagrams are limited to the region near the shock and the total number of cells in the computations was reduced to 256. The shock is initially located at $x = 0.5$ and moves with a velocity of 0.01 to the left. The upstream Mach number is 1.3. For cases (a) and (d), the threshold is on and a centered stencil is used for the majority of the computational space. The centered stencil is the linearly stable stencil. Cells on either side of the shock use downwind or upwind stencils as appropriate. For cases (b) and (c), the threshold parameter is off and there is a great deal more stencil shifting in the smooth regions of the flow. Note that the stencils in these two cases follow entropy and acoustic wave paths downstream of the shock. The stencil traces for these wave paths have slopes corresponding to acoustic and convecting wave speeds.

Effect of mesh spacing. The effect of mesh spacing is illustrated in figures 21 and 22. The results presented in figures 21 and 22 are for a shock moving to the left at a speed of $u_s = 0.01$ with an upstream

Mach number of 1.3. The difference in the results occurs because of the difference in discretization. A 256-cell mesh was used to obtain the results of figure 21, while a 1024-cell mesh was used to obtain the results of figure 22. The entropy distributions in figures 21 and 22 are offset by a constant of 0.0075 and the numerical values of entropy are removed from the vertical axis for clarity. Refining the mesh reduces the magnitude of entropy oscillation and shows the effect of the biasing parameters more distinctly. Each combination of biasing parameters has a unique spurious entropy pattern. Case (a) is highly oscillatory with multiple frequencies per wavelength of the oscillation. Case (b) has the smallest amplitude of entropy peaks. Case (c) has the fewest peaks per period of spurious oscillation, but the amplitude of the largest peak is high. Case (d) has large entropy peaks as well as multiple frequencies per oscillation. Although all of the results show significant entropy error, the results obtained by biasing the stencil and turning the threshold off (case (b)) provide the lowest amplitude of entropy error.

Another effect of the mesh spacing is the reduction in the wavelength of the spurious entropy. In figure 21, the wavelength of spurious entropy computed by equation (81) is $\lambda_s \approx 0.34$. Refining the mesh in figure 22 reduces this wavelength to $\lambda_s \approx 0.086$. The number of points per wavelength of the spurious entropy wave is the same for both computations, since u_2/u_s is constant.

Figure 23 shows the effect of Roe and Osher flux solvers on the spurious entropy. The result is shown for case (b) because other cases had similar results. The effect of the Osher solver on the spurious entropy was to remove one of the peaks in the entropy wave for each oscillation wavelength that was seen in the Roe solver results.

Calculations of supersonic jet noise will often have shocks moving slowly relative to the grid. Although the results presented thus far have shown that spurious entropy exists in calculations with slowly moving shocks, it has also been noted that spurious pressure waves are very small in amplitude.

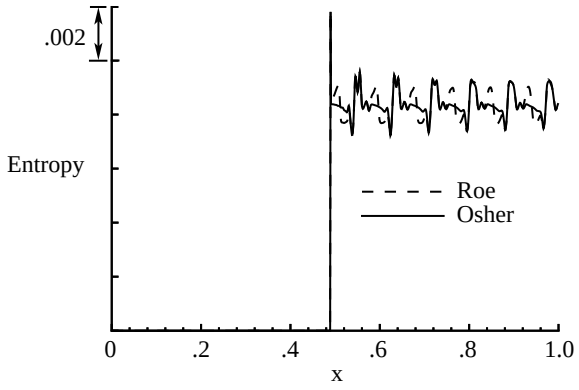

Figure 23. Entropy as a function of distance along duct length for Roe and Osher flux solvers for biasing on and threshold off.

Economics of Higher Order Schemes

The desired accuracy in a computational solution determines whether it is more economical to use a second order scheme with many grid points or a high-order scheme with fewer grid points. Figure 24 illustrates how the cost of implementing these algorithms, as measured by CPU seconds per time step, varies as a function of the solution error.

This figure is constructed in the following manner. The quasi-one-dimensional Euler equations described in detail in chapter 4 are solved for the nozzle problem. Grid refinement studies for the second, third, and fourth order ENO algorithms are performed on a Cray 2 computer. For each successively refined spatial discretization, the error in Mach number is computed for a steady isentropic flow in a converging-diverging nozzle. In addition, CPU seconds per time step is measured for the solution on each mesh. The relationships of error and CPU time as functions of grid spacing are then combined

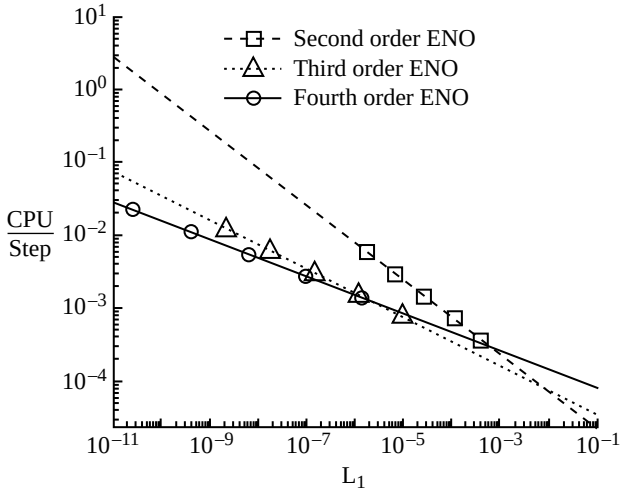

Figure 24. Computational time per step as a function of L_1 error for second, third, and fourth order ENO schemes.

to construct the figure. Because the temporal and spatial accuracy properties are equivalent for these algorithms, the trends presented in figure 24 will be similar whether the accuracy computations are performed on steady or unsteady flows. The error in figure 24 is measured in the L_1 norm, defined by

$$\frac{\sum_{n=1}^{N} \left| M(x_n) - \hat{M}(x_n) \right|}{N} \tag{82}$$

where $M(x)$ is the exact value, $\hat{M}(x)$ is the numerical approximation, and N is the number of discrete values in the numerical solution.

Figure 24 shows that when an error of the order of 10^{-1} is acceptable, the second order scheme is more efficient than the fourth order scheme by almost an order of magnitude. If an error on the order of only 10^{-6} is acceptable, then the higher order schemes are an order of magnitude more efficient. Note that continually increasing the order of accuracy in a scheme does not necessarily result in a significant reduction in CPU time, even at very low acceptable levels of error. Figure 24 shows that for the ENO scheme, most of the benefit is realized in moving from second to third order in the range of error norms considered.

It should be noted that the results of figure 24 are particular to the quasi-one-dimensional ENO algorithms used in this study. Figure 24 will not apply to the implementation of all schemes, because the relative cost of obtaining high-order accuracy for different algorithms will vary. However, the procedure for determining the relationship of computer cost as a function of acceptable error for different algorithms will be the same.

Extracting Acoustics From Aerodynamic Flow

Acoustics Defined

To be able to extract acoustics from an aerodynamic flow, it is important to define the characteristics of the acoustic waves. For the purposes of this paper, acoustic waves have the following characteristics:

1. Acoustic waves propagate to the far field at the sum of the local velocity and sound speeds.

2. Acoustic waves are isentropic.

3. Acoustic waves are small amplitude.

It is often useful to consider geometrical spreading laws to find or categorize acoustic waves. For example, when the computation includes a region of uniform (or zero) mean flow velocity, acoustic pressure decays proportional to $1/r$ in three-dimensional flows and $1/\sqrt{r}$ in two-dimensional flows. There is no decay in pressure amplitude in one-dimensional flows. (Note that these decay properties are valid when wave steepening is negligible. The spreading characteristics of nonlinear waves are discussed in ref. 32.) Geometrical spreading relations are more difficult to interpret in complex flow fields.

The characteristics of acoustic waves can be readily measured in the far field where the amplitudes of the acoustic disturbances dominate those of the "hydrodynamic" (nonpropagating) disturbances. However, the application of these definitions near the source becomes more difficult. In fact, separating the acoustic disturbances from the hydrodynamic disturbances in the acoustic near field is not considered to be possible because these quantities do not exist independently (ref. 33). Both hydrodynamic and acoustic disturbances are heard by a near field observer, but because the hydrodynamic disturbances decay more rapidly with distance from the source than the acoustic disturbances, only the acoustic disturbances impact the far field.

Requirements for Acoustic Calculations

The characteristics of acoustic disturbances determine the requirements of the direct numerical simulations used. The numerical simulation must be highly accurate, have a large computational domain, and have a long time solution.

The small amplitude of the acoustic waves relative to the underlying mean flow and the large distances the acoustic waves travel require that the numerical simulation be high-order accurate and/or use a grid fine enough to sufficiently resolve the acoustic waves. The disparity of length and time scales typically of importance in acoustics makes accuracy an issue, since small scales are often important and cannot afford to be filtered from the computational solution. In addition, boundary conditions must be accurately imposed.

Because acoustic disturbances are defined as the propagating portion of the unsteady pressure field, calculation of acoustics requires a large computational domain. The computational domain must be large enough that the pressure field can be measured at least one acoustic wavelength away from the source. Acoustic wavelengths are often much larger than the source that generate the sound.

Long time calculations are necessary to compute at least one period of the far field sound if the acoustic signal is periodic. For nonperiodic signals, seven to ten cycles of the lowest frequency are required for reasonably accurate spectral estimates. (For a good description of accuracy in spectral estimates, see ref. 34.)

Summary of Chapter 2

The computation of slowly moving shock waves produces spurious, numerical entropy. The spurious entropy is a function of the algorithm used in the calculation, and as seen by the modifications made to the ENO scheme, even slight changes in a basic algorithm can produce marked changes in the structure of the spurious entropy. This phenomenon has been observed by the authors in implementing the MacCormack's scheme, ENO schemes, and a matrix dissipation Runge-Kutta scheme. It has also been observed by others who were using flux vector splitting schemes (ref. 31), flux-difference splitting schemes with Godunov, Roe, and Osher flux solvers (ref. 13), and PPM methods (ref. 30). Spurious entropy normalized by the entropy jump across the shock decreases with increasing shock strength and increasing shock velocity, but is insensitive to Courant number. The amplitude of spurious entropy perturbations is relatively unaffected by the flux solver used, but the Osher solver reduces the number of peaks in the spurious entropy wave form.

Because the amplitude of the spurious entropy wave is a function of the shock speed relative to the grid, the obvious method of eliminating the spurious entropy is to move the computational grid with the shock during the calculation. Although this grid is not difficult in one-dimensional problems, it is considered unreasonable for the multidimensional problems of practical interest, and was not implemented during the course of this research. Another approach to reducing the spurious entropy is to increase the dissipation of the algorithm, as suggested by Woodward and Colella (ref. 30). This increase in the dissipation was not implemented, because the added dissipation would affect the acoustic waves as well as the entropy. Acoustic pressure waves seem to be less sensitive to numerical errors generated by slowly moving shocks.

In the section "Economics of Higher Order Schemes," it was shown that the trade-off between the added cost of using higher order algorithms depends on the level of accuracy required. The analysis performed for sound in a converging-diverging nozzle showed that for a numerical error on the order of 10^{-6}, the third order ENO algorithm is most cost-effective. Therefore, the third order ENO algorithm is used for most of the work presented here.

Chapter 3

Interaction of Sound With a Planar Shock Wave

In this section the interaction of a sound wave with a shock is considered. This study is meaningful because it models the planar oscillation of a shock wave and shock waves in real aerodynamic flows are inherently unsteady.

In the first three sections, shock capturing formulations of MacCormack's and ENO schemes are applied to the governing equations of fluid dynamics for time dependent, shocked flow through a nozzle. These computations predict the amplification of sound by a shock and compare the solutions provided by the different algorithms. Validation of numerical results is always important, but is particularly important for these calculations because, although high-order schemes ensure high-order accuracy in smooth regions of the solution, they necessarily reduce to first order at the shock. Hence, accuracy is lost in the vicinity of the most important region of the solution: the sound source. Since a linear theory exists for this problem, numerical results are validated for the case of small amplitude acoustic waves incident on the shock. Much of the content in the first three sections was originally published by the author (ref. 35), but is included here for completeness.

The section entitled "Energy Analysis" includes an analysis of the disturbance energy associated with a sound wave passing through a shock. This analysis provides insight into the source of disturbance energy generated at the shock.

Analysis

Linear Theory

Within the context of linear theory, only entropy and acoustic waves may exist in a quasi-one-dimensional flow (ref. 35). In a fully linear flow, these waves are independent. However, when the flow field contains nonlinear features such as shock waves, the nonlinearity acts as a coupling mechanism between the linear waves. Thus, the presence of shock waves in a flow field makes it possible for a sound wave incident upon a shock to suddenly change its amplitude and generate an entropy wave.

Entropy is generated across the shock. For a steady flow, this change in entropy is independent of time. However, when a sound wave impinges upon the shock, the shock begins to oscillate, the change in entropy is no longer constant, and a periodic entropy wave is generated, which convects downstream at the local flow velocity. In addition, the impinging sound wave is amplified.

Linearized analyses of the interaction of small disturbances with shock waves have been made independently by Blokhintsev (ref. 36), Burgers (ref. 37), Moore (ref. 38), Chang (ref. 39), Kerrebrock (ref. 40), and Powell (ref. 41). A numerical study of the interactions of linear plane waves with shocks confirms the validity of the linear theory except possibly for waves with incidence angles near or beyond the critical angle (ref. 42).

Landau and Lifshitz report that the ratio of transmitted to incident sound waves determined by linear theory is

$$\frac{\delta p_2}{\delta p_1} = \frac{M_1 + 1}{M_2 + 1} \cdot \frac{2(\gamma - 1)M_1 M_2^2\left(M_1^2 - 1\right) - (M_1 + 1)\left[(\gamma - 1)\left(M_1^2 + 2\right)\right]}{2(\gamma - 1)M_2^2\left(M_1^2 - 1\right) - (M_2 + 1)\left[(\gamma - 1)\left(M_1^2 + 2\right)\right]} \tag{83}$$

where M_1 is the Mach number upstream of the shock (henceforth called the preshock Mach number), M_2 is the Mach number downstream of the shock, and γ is the ratio of specific heats of the fluid (ref. 43). Equation (83) and an expression for the ratio of static pressures p_2/p_1 are plotted with the ratio of specific heats $\gamma = 1.4$ in figure 25. Note that equation (83) predicts an amplification of the acoustic signal as it propagates through the shock wave for all preshock Mach numbers. This amplification is not surprising, since the mean flow pressure also increases across a shock. Note, however, that the ratio of the perturbation pressures $\delta p_2/\delta p_1$ is not the same as that for static pressures p_2/p_1.

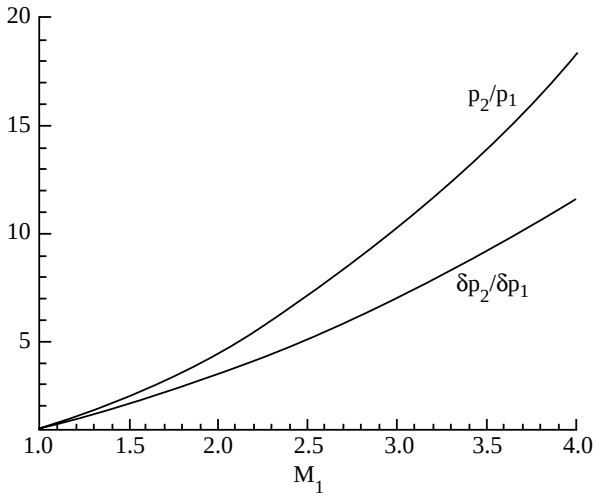

Figure 25. Ratios of static and perturbation pressures as functions of preshock Mach number.

Riemann Analysis

The results of the previous section entitled “Linear Theory” are based on linear theory in which disturbance amplitudes are assumed to be small. To determine the range for which the linear result is valid, the ratio of disturbance pressures across the shock may be computed by considering the iterative solution to the Riemann problem. The Riemann analysis is performed by considering the space and time diagram illustrated in figure 26. Initially a steady shock wave separates states 1 and 4. At some time Δt, a disturbance is introduced upstream of the shock which moves the shock and produces acoustic and entropy waves downstream. Knowing the initial states 1 and 4, the incident perturbation amplitude, and

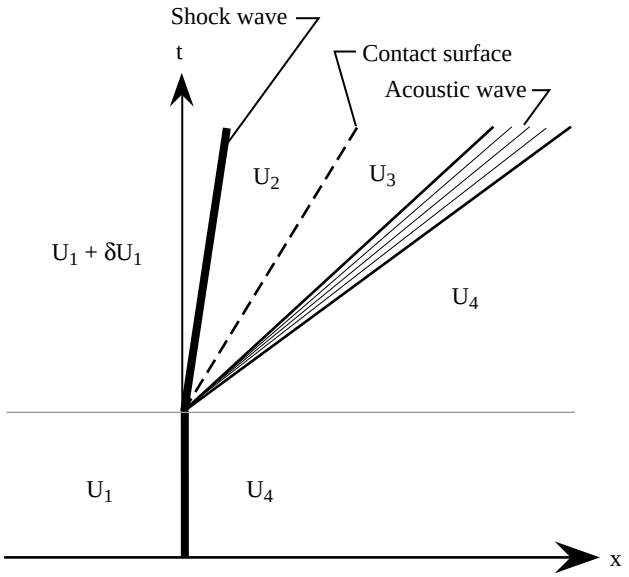

Figure 26. Quasi-steady Riemann problem analysis for sound and shock interaction.

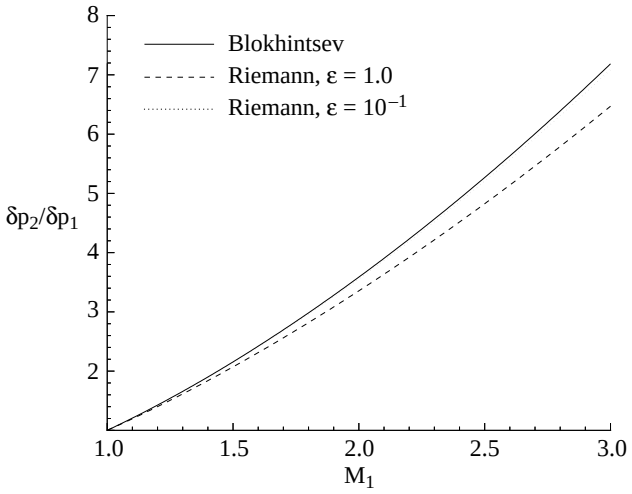

Figure 27. Pressure perturbation as function of upstream Mach number.

utilizing the facts that acoustic waves are isentropic and entropy waves introduce no pressure perturbation, the ratio of the perturbed states 2 and 3 may be found by numerical iteration. For an incident sound wave of pressure perturbation $\delta p_1 = \varepsilon p_1 \sin \omega t$, the ratio $\delta p_2/\delta p_1$ is of interest. The ratio $\delta p_2/\delta p_1$ is compared with the linear theory result in figure 27 for several perturbation amplitudes and shows excellent agreement for perturbation amplitudes less than $\varepsilon = 10^{-1}$. (Results for $\varepsilon \le 10^{-2}$ are visually indistinguishable from the results of Blokhintsev.) Even for perturbation amplitudes of $\varepsilon = 1.0$, there is only a 10-percent difference between solutions at $M = 3$.

Combining the expression for $\delta p_2/\delta p_1$ with the Rankine-Hugoniot shock jump relations, similar expressions for the fluctuations in density and entropy downstream, as well as for the shock velocity, can be calculated. These relations are plotted in figures 28 and 28. Figure 28 shows the relationship between the ratios of perturbation pressure, entropy, and density perturbations across the shock. These ratios were computed using a perturbation amplitude of $\varepsilon = 10^{-3}$. This figure shows that the pressure

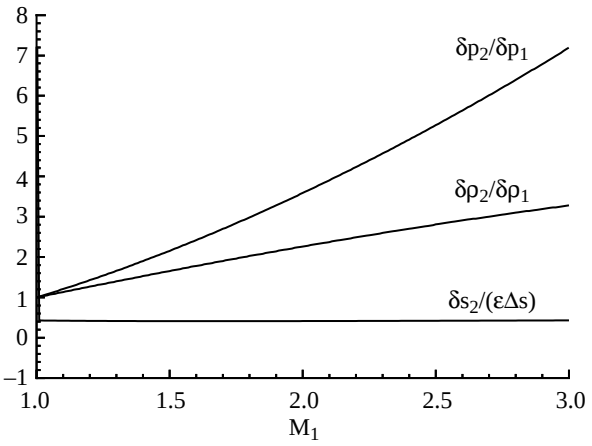

Figure 28. Perturbation ratios as a function of upstream Mach number.

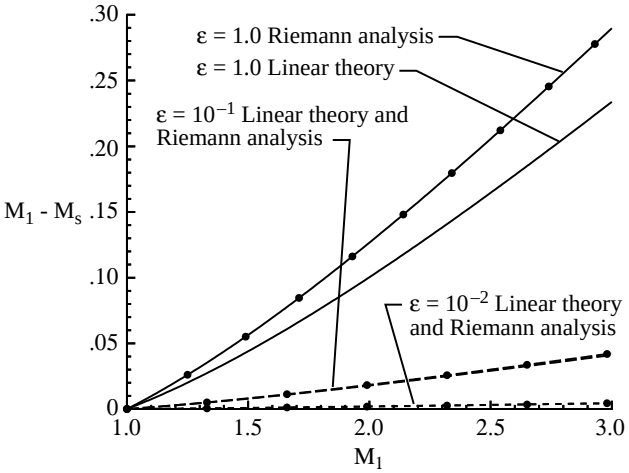

Figure 29. Shock speed number as a function of upstream Mach number.

fluctuation is significant over a wide range of Mach numbers. The entropy fluctuations downstream of the shock are very small; the quantity δ_s/Δ_s is on the order of ε, except near $M = 1$ where $\Delta_s \to 0$. Figure 29 shows the shock Mach number as a function of the upstream Mach number for several perturbation amplitudes. As expected, the results obtained for small perturbations ($\varepsilon \le 10^{-1}$) are indistinguishable from the results of the Riemann analysis, while there is a significant difference in the results obtained for the large perturbation ($\varepsilon = 1.0$). The shock motion increases with upstream Mach number and perturbation amplitude.

Model Problem

Governing Equations

The equations governing the unsteady quasi-one-dimensional flow in a nozzle are

$$\frac{\partial \mathbf{U}}{\partial t} + \frac{\partial \mathbf{F}}{\partial x} = \mathbf{Q} \tag{84}$$

where $\mathbf{U}$ is the vector of conserved variables $[\rho, \rho u, \rho e]^T$, t is time, x is the streamwise direction coordinate, $\mathbf{Q}$ is a source vector due to the area variation $[0, p\, dA/dx, 0]^T$, and $\mathbf{F}$ is the flux vector

$[\rho uA, \rho u^2 + p)A, (\rho e + p)uA]^T$, where A is the area of the nozzle, ρ is density, u is velocity, e is total energy per unit mass, and p is pressure.

Nozzle Shape

Consider a nozzle which is converging-diverging and designed for a linear Mach number distribution when flow is isentropic and fully expanded to produce supersonic velocity in the diverging section. The area distribution for such a nozzle is

$$A(x) = \left[\frac{1 + \frac{\gamma - 1}{2} M(x)^2}{\frac{\gamma + 1}{2}}\right]^{\frac{\gamma+1}{2(\gamma-1)}} \frac{1}{M(x)} \qquad 0 \le x \le 1 \tag{85}$$

For the computations performed here, the Mach number at the nozzle inlet is $M = 0.8$ and varies as a function of distance along the nozzle length

$$M(x) = (\alpha x + 0.8) \qquad 0 \le x \le 1 \tag{86}$$

where x is the distance along the nozzle, normalized by the nozzle length.

To simplify the application of boundary conditions at the inflow and outflow, the area distribution outside of the nozzle is held constant, that is

$$A(x) = A(x = 0) \qquad x \le 0 \tag{87}$$

$$A(x) = A(x = 1) \qquad x \ge 0 \tag{88}$$

Two Mach slopes are used in consideration of a range of practical significant preshock Mach numbers to keep the shock close to the center of the nozzle diffuser. The values of Mach slope α used in the calculations presented here and the corresponding preshock Mach numbers are presented in table 1.

A sketch of a nozzle with a Mach slope of 1 is shown in figure 30.

Table 1. Mach Slopes and Range of Preshock Mach Numbers

Mach slope	Preshock Mach number
1	1.4 to 1.8
2	2.0 to 2.6

Governing Equations and Boundary Conditions

The unsteady, compressible, inviscid flow in a nozzle of varying cross-sectional area is governed by the quasi-one-dimensional Euler equations (84). These equations are solved in conservation form so that shocks are automatically captured. Total pressure and entropy are prescribed upstream of the shock at the nozzle inlet and static pressure is prescribed downstream of the shock at the nozzle exit plane. Flow quantities are normalized by the upstream stagnation conditions and the nozzle length L. Finite wave conditions developed by Atkins and Casper are employed at the boundaries (ref. 44). These conditions are described in appendix C.

The first step in numerically modeling the interaction of a sound wave with a shock is to determine an accurate steady flow solution throughout the nozzle. To obtain sufficiently accurate unsteady results, the steady state residual is converged to several orders of magnitude smaller than the smallest perturbation amplitude to be investigated. Steady flows with residuals only one or two magnitudes smaller than the perturbation amplitude may introduce spurious entropy at the inflow boundary in the unsteady calculation.

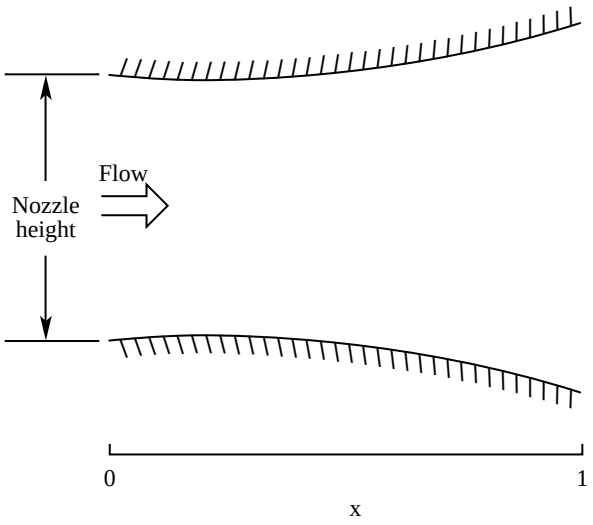

Figure 30. Nozzle geometry for Mach slope = 1.

To induce unsteady flow through the nozzle, the inflow boundary condition is perturbed sinusoidally and isentropically. The pressure perturbation is prescribed as

$$\delta p = \varepsilon p \sin \omega t \tag{89}$$

where ε and ω are the normalized amplitude and frequency of the perturbation, and p and t are the normalized pressure at the inflow boundary and time. The pressure perturbation introduces an acoustic wave at the nozzle inlet which propagates downstream at a velocity equal to the sum of the local velocity and sound speed. A range of perturbation amplitudes is selected so that linear as well as nonlinear waves can be investigated. The time dependent features of the flow are computed, and the effect of the shock on the sound wave is observed.

Algorithms

To admit discontinuous solutions, shock capturing formulations of MacCormack's and ENO algorithms described in chapter 2 are employed for the computations. Therefore, shock fitting methods that explicitly invoke the Rankine-Hugoniot jump relations across a shock are not required.

Results of Calculations

Unsteady Calculations

The results presented in this section are for the case of perturbation amplitude $\varepsilon = 0.01$ and frequency $\omega = 60$, which corresponds to an approximate wave number of 5.25. The calculations are performed on a grid of 128 cells, which corresponds to approximately 24 points per wavelength. The nozzle back pressure is prescribed so that a shock appears at $x = 0.6$ in the steady solution. For a nozzle with a Mach slope $\alpha = 1$, this condition corresponds to a preshock Mach number of 1.4.

Figure 31 shows the perturbation pressure, density, and velocity in the nozzle at a normalized time of π and the results provided by MacCormack's and the second, third, and fourth order ENO schemes. Perturbation quantities are determined by subtracting the mean flow quantities from their time dependent counterparts

$$\begin{aligned} \delta p(x,t) &= p(x,t) - p(x,0) \\ \delta \rho(x,t) &= \rho(x,t) - \rho(x,0) \\ \delta u(x,t) &= u(x,t) - u(x,0) \end{aligned} \tag{90}$$

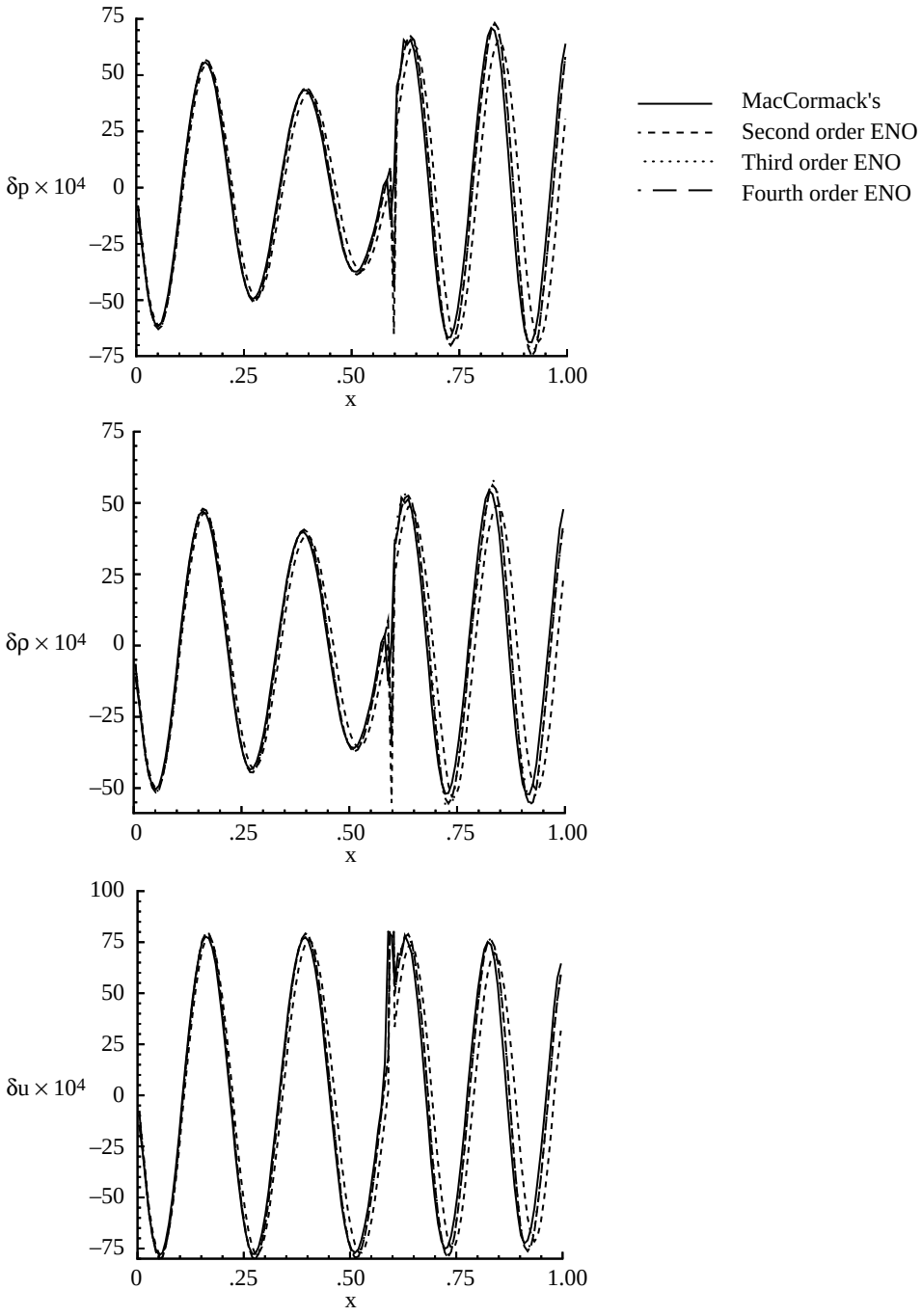

Figure 31. Pressure, density, and velocity perturbations along nozzle length.

where p is pressure, ρ is density, u is velocity, x is streamwise directional coordinate, and t is time.

The MacCormack's and the third and fourth order ENO schemes do an excellent job of predicting the perturbation pressure upstream of the shock where the flow is smooth. The second order ENO scheme, which behaves similar to a TVD scheme because it has only second order interpolation, has a slight leading phase error. At the shock, the ENO schemes do better at capturing the shock in fewer cells. The flow solutions differ more significantly downstream of the shock. The phase shift error is amplified and the wave amplitude is dissipated in the second order ENO results. The MacCormack

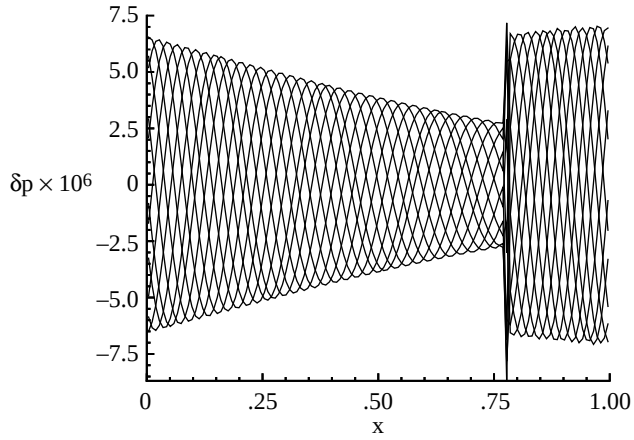

Figure 32. Pressure perturbation along nozzle. $\varepsilon = 10^{-5}$; $M_1 = 1.58$.

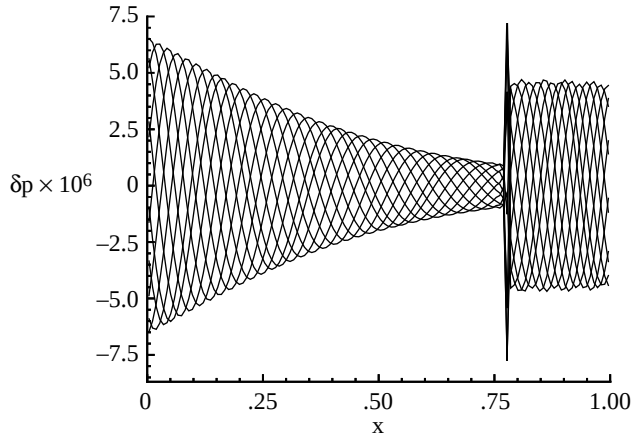

Figure 33. Pressure perturbation along nozzle. $\varepsilon = 10^{-5}$; $M_1 = 2.36$.

solution is slightly damped relative to the third and fourth order ENO solutions and has spurious oscillations on portions of the perturbations close to the shock. The difference in the solution between the third and fourth order ENO schemes is not graphically perceptible on this scale. Note that with mesh refinement all schemes (including MacCormack's and the second order ENO scheme) converge to the solutions produced by the higher order ENO schemes.

These results show that all the algorithms applied to this problem compute the perturbation quantities in the nozzle well. The third and fourth order ENO schemes provide the best solutions because they have no oscillations at the shock and less damping downstream. The cost of running high-order ENO is higher than second order ENO or MacCormack's scheme, however. The economics of high-order schemes is discussed in the section entitled "Economics of Higher Order Schemes."

Effect of Mach Number

Sound amplification by a shock wave is highly dependent upon the preshock Mach number. Figures 32 and 33 show a sequence of pressure perturbations moving through the nozzle for preshock Mach numbers of 1.58 and 2.36. A small amplitude perturbation of $\varepsilon = 10^{-5}$ is introduced at the inflow boundary. The perturbation maintains its sinusoidal shape throughout the nozzle. The amplitude decreases as the flow expands in the nozzle upstream of the shock. At the shock, it is amplified as the flow is

compressed and continues to increase gradually as the flow is compressed further. The amplification of the sound wave is much more significant at higher Mach number.

Comparison of Numerical Results With Linear Theory

To quantify the effect of Mach number on the perturbation amplification and validate the computations, the numerically determined pressure perturbation amplitude ratio is compared in figure 34 with the linear theory over a range of Mach numbers for perturbation amplitudes of $\varepsilon = 10^{-5}$ and $\varepsilon = 10^{-2}$. The first amplitude is small enough to be well within the validity of the linear theory. The second amplitude approaches the limit of linear theory validity, particularly for lower Mach numbers where the shock is weak and may undergo large excursions. The normalized acoustic perturbation wave number at the inflow boundary is set to 4. Results for Mach numbers between 1.4 and 2.6 are presented here. The computations have from 22 to 27 cells per wavelength. Table 2 lists the cells per wavelength for the cases presented in this paper.

Figure 34 compares the numerical results with linear theory. The third order ENO scheme and linear theory match extremely well for the very small amplitude perturbation of $\varepsilon = 10^{-5}$. The differences between numerical solutions and linear theory become more pronounced at the higher perturbation amplitude of $\varepsilon = 10^{-2}$. Some discrepancy between the linear theory and numerical results is not surprising since nonlinearities may become important at this perturbation amplitude. Because the shock in the MacCormack solution is spread over several cells, determination of the ratio $\delta p_2 / \delta p_1$ is more difficult, particularly when the shock is located close to the end of the nozzle. This difficulty is why no MacCormack result is shown for $M = 2.6$.

Table 2. Preshock Mach Number and Minimum Cells per Wavelength for Calculations

Preshock Mach number	Minimum cells per wavelength
1.4	26.92
1.58	26.18
1.7	25.75
2.0	23.52
2.36	22.50
2.6	22.13

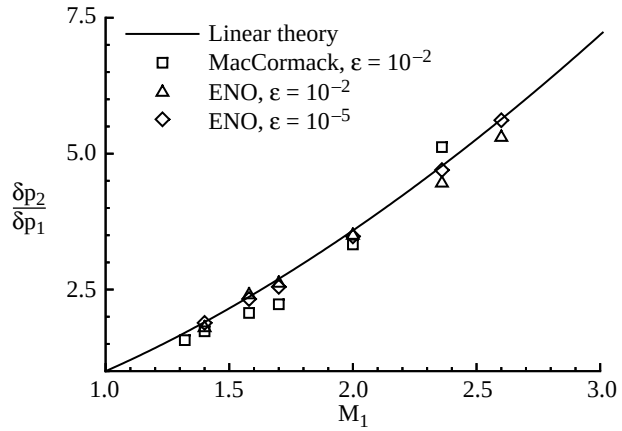

Figure 34. Perturbation ratio as a function of preshock Mach number.

Energy Analysis

The previous sections have shown that according to linear theory and numerical computation, sound pressure is amplified as a sound wave passes through a shock. This section will address the issue of whether acoustic energy is generated in the interaction process.

To address this issue, consider Myers' energy corollary (ref. 45). Myers' energy corollary is an exact equation governing the transport of energy associated with an arbitrary flow field. This corollary describes the acoustic energy in general situations where the linear description of energy is inadequate. Clearly, with the highly nonlinear flow field associated with sound and shock interaction, such an approach is warranted here.

For a one-dimensional flow in which viscous effects are negligible, Myers' corollary reduces to

$$\frac{\partial E}{\partial t} + \frac{\partial W}{\partial x} = -D \tag{91}$$

where E is energy density, t is time, W is disturbance energy flux, and x is streamwise direction coordinate and the disturbance energy density divided by area is defined

$$\frac{E}{A} = \frac{1}{2}\rho\left(u^2 - u_0^2\right) + \rho_0 u_0 \cdot (u_0 - u) - \rho T_0 (s - s_0) - (p - p_0) + \rho(h - h_0) \tag{92}$$

where A is the cross-sectional area of the duct, T is the absolute temperature, h is the enthalpy, s is entropy, ρ is density, p is pressure, and u is velocity. The subscript 0 represents the undisturbed state. The disturbance energy flux divided by area is

$$\frac{W}{A} = (\rho u - \rho_0 u_0)[h - h_0 - T_0(s - s_0)] + \rho_0 u_0 (T - T_0)(s - s_0) \tag{93}$$

and the disturbance energy source divided by area is

$$\frac{D}{A} = -(\rho u - \rho_0 u_0)(s - s_0) \cdot \nabla T_0 - (s - s_0)\rho_0 u_0 \cdot \nabla (T - T_0) \tag{94}$$

For the one-dimensional sound and shock interaction, only acoustic and entropy modes are present (vorticity requires three dimensions). Thus, the energy density can be divided into two types of energy, acoustic E_a and entropy E_s, as

$$E_a = \frac{1}{2}\rho\left(u^2 - u_0^2\right) + \rho_0 u_0 (u_0 - u) - (p - p_0) + \rho \left.\frac{\partial h}{\partial p}\right|_s (p - p_0) \tag{95}$$

and

$$E_s = \rho\left[\left.\frac{\partial h}{\partial s}\right|_p (s - s_0) - T_0 (s - s_0)\right] \tag{96}$$

where

$$\left.\frac{\partial h}{\partial s}\right|_p = \frac{1}{\gamma - 1} p^{\frac{\gamma - 1}{\gamma}} s^{\frac{1 - \gamma}{\gamma}} \tag{97}$$

and

$$\left.\frac{\partial h}{\partial p}\right|_s = p^{\frac{-1}{\gamma}} s^{\frac{1}{\gamma}} \tag{98}$$

where γ is the ratio of specific heats for an ideal gas.

It is instructive to examine the energy components and energy source terms in space and time to see how these quantities change during the sound and shock interaction process. These quantities from equations (95), (96), and (94) are shown in figures 35 to 37 for the Mach number upstream of the shock $M_1 = 3$, the acoustic disturbance amplitude $\varepsilon = 0.1$, and 512 cells, which are distributed along the duct length. For these calculations, the shock is initially at $x = 0.4$. The sound disturbance enters the duct at a time of $t = 0$ at the duct inlet and propagates downstream. At a time of $t \approx 0.13$ the sound wave hits the shock. After the interaction, figure 35 shows that acoustic energy is present downstream. The amplitude of the sound energy downstream of the shock is higher than the energy upstream, which indicates that acoustic energy is generated by the sound and shock interaction process. Note that the slope of the path of the sound wave in space and time increases after interaction with the shock. The inverse of the slopes before and after the shock corresponds to the quantities $u_1 + c_1$ and $u_2 + c_2$, respectively, where u is velocity, c is speed of sound, and the subscripts 1 and 2 refer to the states upstream and downstream of the shock, respectively.

Figure 36 shows the component of entropy energy in space and time. Because the sound wave is by definition isentropic, there is no disturbance entropy upstream of the shock. After the sound wave hits the shock at $t \approx 0.13$, however, entropy energy appears downstream. Thus, entropy energy is generated during sound and shock interaction. The inverse slope of the path of the disturbance entropy corresponds to the downstream convection velocity, as expected. Figure 37 shows the variation in the source term of equation (94) and provides insight into the generation of disturbance acoustic and entropy energy downstream of the shock. The source term is zero except along the shock wave for $t > 0.13$. Thus, the shock wave is the source of the disturbance energies downstream. Equation (94) indicates that the source of disturbance energy is the transfer of energy from the mean flow. This transfer can occur in the presence of a temperature gradient with fluctuations in entropy and momentum and with fluctuations in entropy and temperature. Note that the source term is zero when the fluctuation in entropy is zero. This correlation implies that the disturbance energy source is related to the shock motion.

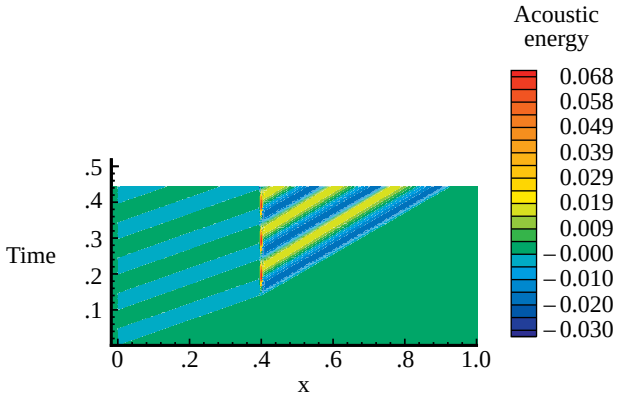

Figure 35. Disturbance acoustic energy as a function of space time for 512 cells distributed along duct length. Preshock Mach number = 3; disturbance acoustic amplitude = 0.1.

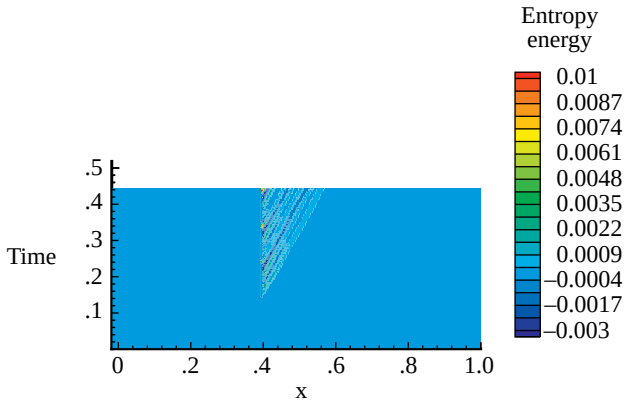

Figure 36. Disturbance entropy energy as a function of space time for 512 cells distributed along duct length. Preshock Mach number = 3; disturbance acoustic amplitude = 0.1.

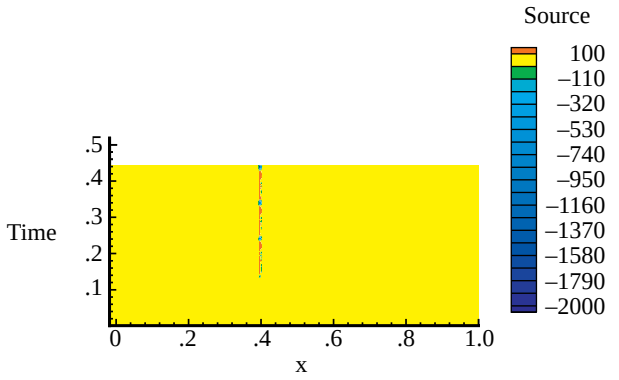

Figure 37. Disturbance energy source as a function of space time for 512 cells distributed along duct length. Preshock Mach number = 3; disturbance acoustic amplitude = 0.1.

Summary of Chapter 3

This section describes a numerical investigation of sound amplification by a shock wave. MacCormack's and the second, third, and fourth order ENO schemes are employed to compute the time dependent shocked flow field in a converging-diverging nozzle. The flow is disturbed by introducing a sound wave at the inflow boundary. All schemes are shown to predict the perturbation amplitude and phase speed in the nozzle well, especially in the supersonic, smooth portion of the flow. The high-order ENO schemes provide the best overall results because the flow around the shock does not contain spurious oscillations and the flow downstream of the shock shows little dissipation.

The numerical results are compared with linear theory. Linear theory validates the numerical solution for small perturbation amplitudes. Numerical results for the larger perturbation amplitude also compare well with the linear theory, which indicates that the linear theory has a wide range of applicability in predicting sound amplification by a shock.

Analysis of the equation governing the perturbation energy shows that disturbance energy is generated at the shock. The source term for this energy goes to zero as the entropy fluctuation goes to zero. This correlation indicates the importance of shock motion on the generation of disturbance energy.

Chapter 4

Interaction of a Vortex Ring With a Shock Wave

In this section the interaction of a vortex ring with a normal shock wave is considered. The study of this interaction models a fundamental mechanism of sound generation in supersonic jets: the interaction of turbulence with shock waves.

Early research on shock and vortex interaction focused primarily on experimental studies (refs. 46, 47, and 48) and the development of predictive linear theories (refs. 49, 50, and 38), which were compared with experimental results. Ribner suggested that the study of the interaction of a vorticity wave with a shock would provide useful information about the sound generated by turbulence in supersonic jet flows (ref. 49). Ribner studied the problem analytically and developed a linear theory that described sound generated by shock-vortex interaction (refs. 49 and 50). Moore studied the interactions of a variety of plane wave disturbances with shocks in an unsteady reference frame (ref. 38).

Pao and Salas studied the interaction of a shock wave and a vortex numerically (ref. 51). Their study investigated the interaction of a columnar vortex with a normal shock wave by solving the Euler equations and using MacCormack's scheme with a shock-fitting numerical technique. Salas (ref. 52), Hussanini et al. (ref. 53), and Kopriva et al. (ref. 54) applied spectral methods with shock fitting methods to the shock-vortex problem. Spectral methods provided increased accuracy of the solution, but were limited to weak shock and vortex interaction cases. Meadows, Kumar, and Hussaini (ref. 55) studied the interaction of a columnar vortex with a shock wave by using a shock capturing scheme. Shock capturing proved to be beneficial because strong shock and vortex interaction cases that result in the formation of secondary shocks could be studied readily. The authors noted that to provide a quantitatively accurate representation of the acoustic wave, improved downstream boundary conditions and higher order numerical schemes were required. Casper then investigated the shock and vortex interaction problem with a high-order ENO scheme and found that higher accuracy greatly improved the resolution of the acoustic wave downstream of the shock (ref. 56).

Reference 56 studied columnar vortex and shock interactions. The interaction of a vortex ring with a shock closely models the interaction of turbulence within the shear layer with shock waves present in the plumes of imperfectly expanded axisymmetric supersonic jets.

Model

The calculations presented in this section model the interaction of a vortical structure within the supersonic portion of the shear layer with a shock wave. The core size is small relative to the size of the ring in these calculations, primarily because of numerical considerations. Because the shear layer in a jet spreads with increasing distance from the nozzle exit plane, a vortex ring with a small core models the interaction of disturbances in the shock cell closest to the nozzle lip. When results are presented in dimensional units, the variables are dimensionalized with ambient stagnation sound speed and atmospheric pressure; thus, the calculations closely model disturbances that interact with the first shock cell of an overexpanded nozzle (fig. 37).

The strength of the vortex is chosen to correspond to the observed strengths of turbulent fluctuations in the jet shear layer. Experimental observations indicate that an appropriate level of velocity disturbance is approximately 3 percent of the mean flow velocity. The vortex strength chosen for the majority of the calculations presented here (M_1 = 1.5) has a velocity perturbation (the ratio of the vortex core velocity to the upstream mean flow velocity) of 6.8 percent.

Although imperfectly expanded jet flows typically contain systems of oblique shocks, this model uses the interaction of a ring vortex with a normal shock wave. This model is a reasonable

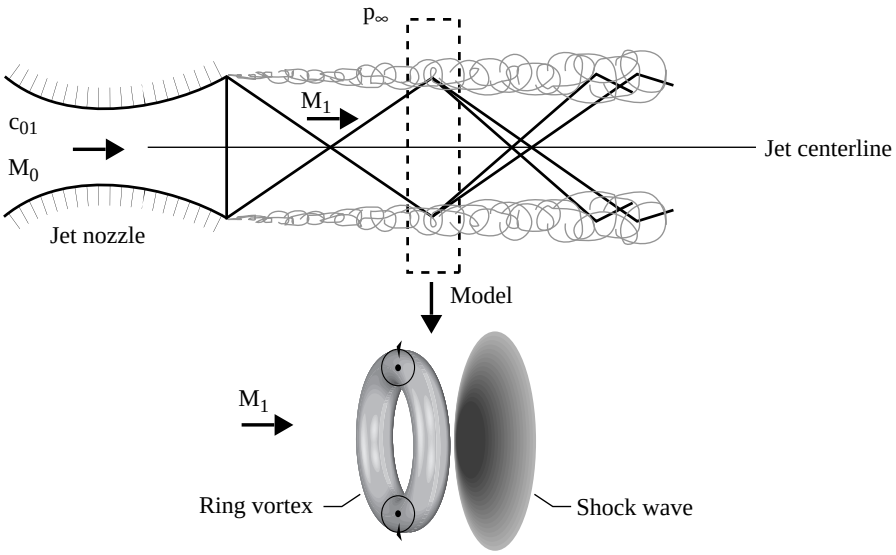

Figure 37. Model of vortex ring and shock interaction.

approximation because the oblique shocks tend to curve upstream with increasing distance from the jet centerline and are approximately normal upon termination in the shear layer (ref. 58).

Vortex rotation is taken to be counterclockwise for the majority of the calculations because the velocity decreases with increasing distance from the jet axis, which results in positive vorticity. Some results are shown for a clockwise rotating vortex in the section entitled "Typical Interaction of Clockwise Vortex."

Geometry

The geometric model of the interaction of a ring vortex with a shock wave that was used in the computations is illustrated in figure 38. A vortex ring is introduced upstream of the shock wave. The vortex ring is characterized by its strength Γ, its core radius r_c, and the distance from the axis of symmetry to the vortex filament r_0. The shock is characterized by the Mach number of the flow upstream of the shock M_1.

Governing Equations

The equations that govern the interaction of a vortex ring with a shock wave, neglecting viscous effects, are the Euler equations of gas dynamics in axisymmetric coordinates:

$$\frac{\partial r\mathbf{Q}}{\partial t} + \frac{\partial r\mathbf{F}}{\partial x} + \frac{\partial r\mathbf{G}}{\partial r} = \mathbf{H} \tag{99}$$

where

$$\mathbf{Q} = [\rho, \rho u, \rho v, \rho e]^T \tag{100}$$

$$\mathbf{F} = [\rho u, \rho u^2 + p, \rho uv, (\rho e + p)u]^T \tag{101}$$

$$\mathbf{G} = [\rho v, \rho vu, \rho v^2 + p, (\rho e + p)v]^T \tag{102}$$

$$\mathbf{H} = [0, 0, p, 0]^T \tag{103}$$

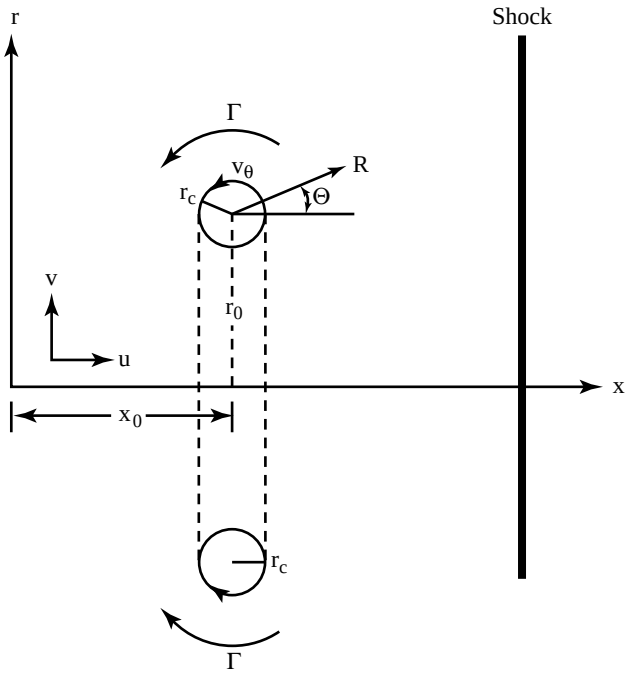

Figure 38. Vortex ring and shock interaction.

ρ is density, *u* and *v* are the velocity components in the axial and radial directions, *e* is total energy per unit mass, *p* is pressure, *x* is the axial position, and *r* is the radial distance from the axis of symmetry.

Boundary Conditions

Conditions are prescribed at the inflow and outflow computational boundaries to establish a shock with the specified strength at $x = 7$. The boundary condition along the axis of symmetry is prescribed by requiring that the fluxes across the axis are zero. The method of prescribing the boundary conditions is described in reference 44.

Solution Procedure

The calculation is performed in two steps. First, a steady, shocked flow is established with the flow parallel to the axis of symmetry. Next, a vortex ring is introduced to the flow field 7 core radii upstream of the shock at a time of $T = 0$. All flow variables are normalized with respect to the static pressure and density upstream of the shock and the size of the vortex core radius. The vortex ring then convects downstream and passes through the shock wave. After this interaction, significant changes occur downstream of the shock wave. Sound, vorticity, and entropy are generated as the vortex interacts with the shock wave. The primary focus of this section is on the acoustic waves generated by the interaction.

Vortex Model

A model of the ring vortex introduces appropriate perturbations in velocity and pressure to the flow field as an initial condition. The vortex is introduced at the initial time $t = 0$ and at subsequent times the Euler equations determine the entire flow field—including the vortex. At all subsequent time steps the Euler equations are satisfied to a level of error that corresponds to the truncation error of the ENO algorithm, which is third order accurate in space and time.

The initial condition prescribed for the vortex is the classical toroidal vortex of Lamb, which is augmented with a solid body core (ref. 59). The derivation of the velocity and pressure equations is provided in appendix B.

Limits of the Vortex Ring Model

The cross section of the vortex ring core is approximately circular when the vortex filament is 170 core radii away from the axis of symmetry (ref. 60). When the vortex core radius increases relative to the ring radius, the degree of circularity decreases, until the vortex becomes Hill's vortex (ref. 60). The streamlines of this vortex become oblong and flatten close to the axis of symmetry. To closely approximate the vortex ring with a circular core, the vortex filament is located 125 core radii away from the axis of symmetry unless otherwise noted. The small size of the vortex core radius relative to the ring radius reasonably approximates the size of a turbulent structure within the supersonic portion of the shear layer near the first shock cell.

Vortex Parameter Modeling

The parameters of the vortex ring which model the physical jet turbulence and shock interaction will be described here. The first parameter of interest is the vortex strength. Circulation is typically considered to be a measure of the vortex strength. For the vortex ring, the circulation is related to the geometrical parameters and induced velocity V according to (ref. 60)

$$\Gamma = \frac{4V\pi r_0}{\left(\ln\frac{8r_0}{r_c}\right) - \frac{1}{4}} \tag{104}$$

The next parameter of interest is the ratio of the core radius to the ring radius r_c/r_0. The core radius models the size of the disturbance in the supersonic portion of the mixing layer when it interacts with the shock wave. The ring radius models the radial distance between the jet axis of symmetry and the inner boundary of the turbulent mixing layer. This ratio is a function of distance downstream from the jet exit plane.

Vortex Preservation Study

An important feature of this calculation is the accurate representation of the source of the sound generation: the interaction of a vortex with the shock. To ensure that the vortex is adequately resolved in the calculation, the time history of the minimum pressure within the vortex is tracked. A series of computations is performed where the vortex ring convects over grids of various resolutions. It was found that while convecting on a uniform mesh with 10 cells per core diameter, the minimum pressure varies by a maximum of 0.035 percent over the time it takes the vortex to travel 7 core radii, which is the initial distance of the vortex from the shock. This level of numerical error is considered to be acceptable; therefore, this grid resolution was held fixed for all the computations.

Computational Grid

As mentioned in the previous section, a grid with 10 cells per vortex core diameter adequately resolved the vortex in the computation. This grid resolution is used in the fine uniform grid in the region $-6 \le x \le 85$ and $72 \le r \le 178$, where $\Delta x = \Delta r = 0.2$. However, it is computationally prohibitive to use a uniform mesh with such fine resolution throughout the entire computational domain. The computational domain is required to be large enough so that at least one wavelength of the acoustic disturbance is contained in the calculation. This size of domain allows accurate measurements to be made in the acoustic far field so that computations to determine the acoustic energy level can be made. In addition, the computational domain must also be large enough that once the acoustic wave has passed a far field observer

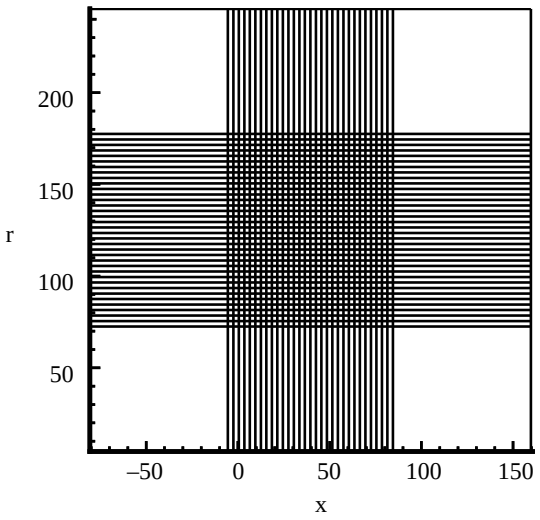

Figure 39. Standard grid used in calculations with only every fifteenth cell shown.

point, the wave has time to go through one period of its oscillation without being contaminated by errors introduced by the boundaries. Thus, in the calculations shown here, the computational grid is uniform over the range of the acoustic source interaction and sound wave propagation through at least one acoustic wavelength. The grid is then stretched to the boundaries by using a hyperbolic sine function. The grid contains 481 cells in the axial direction and 556 cells in the radial direction. Every fifteenth cell of the grid is shown in figure 39.

Note that this grid resolves the generated acoustic waves. Preliminary test calculations performed over Mach number range $1.1 \leq M \leq 1.7$ cover an acoustic peak-to-valley wavelength range of $2.5 \leq \lambda \leq 3.0$. Thus, the minimum resolution of the acoustic wave is 12.5 points per peak-to-valley wavelength. The actual number of points per wavelength is at least twice this number. Thus, the acoustic wave is well resolved.

Also note that there is another length scale of possible interest in this problem, which is not well resolved on this grid. During the interaction of the vortex with the shock, the shock wave begins to move. For typically small vortex strengths, the shock displacement is small. In fact, for many of the calculations performed during the course of this research, the shock moves through the distance of only one cell. Because further grid refinement proved to be prohibitively expensive and one-dimensional calculations of sound and shock interaction provided results which matched linear theory well without resolving the shock motion, the grid was not refined further.

Typical Interaction of Counterclockwise Vortex

A typical interaction of a counterclockwise rotating vortex with a shock wave is described in this section. In the calculations for this case, the Mach number upstream of the shock is $M = 1.5$ and the vortex strength is $\Gamma = 0.75$.

In the contour plots shown in this chapter, contours are shown for a part of the computational domain near the interaction point of the vortex core and the shock wave. Because of the axisymmetry, only a single cross section of the solution will be shown in the results which follow. All the results presented are within the uniform grid region of the computational grid so that effects of grid stretching are not present in the results. The contours are computed on a grid which is five times as coarse as the computational grid. Note that the contour range is kept constant for each plot so that relative values of the perturbation quantities at different time levels can be compared. In these calculations, a unit of time is

defined as $T = r_c/u_1$ where u_1 is the upstream flow speed; thus T represents the time it takes the vortex core to move 1 radius in the flow upstream of the shock.

Contour plots of the flow variables are shown for three selected times: $T = 0$, $T = 8$, and $T = 50$. At time $T = 0$, the vortex is upstream of the shock. At $T = 8$ the most upstream edge of the vortex core is approximately aligned with the shock; at $T = 50$, the vortex is approximately 30 core radii downstream of the shock.

Pressure

Figure 40 shows the change in pressure from the mean state. The only perturbation in pressure at $T = 0$ is the decrease in pressure at the vortex core. As the vortex begins to interact with the shock,

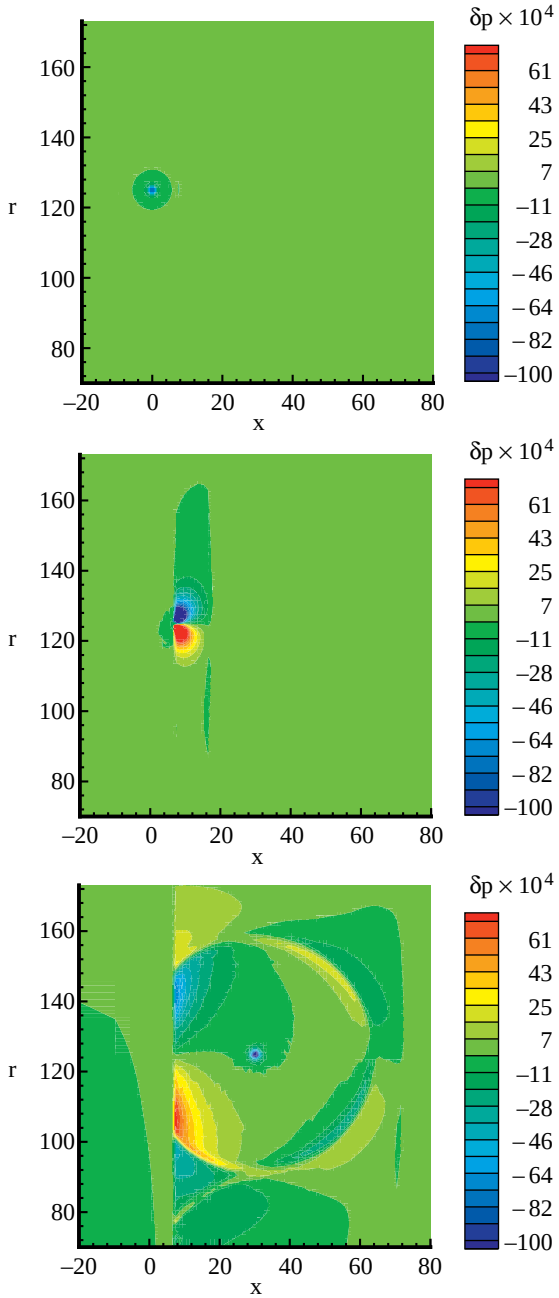

Figure 40. Contours of pressure perturbation downstream of shock at $T = 0$, $T = 8$, and $T = 50$.

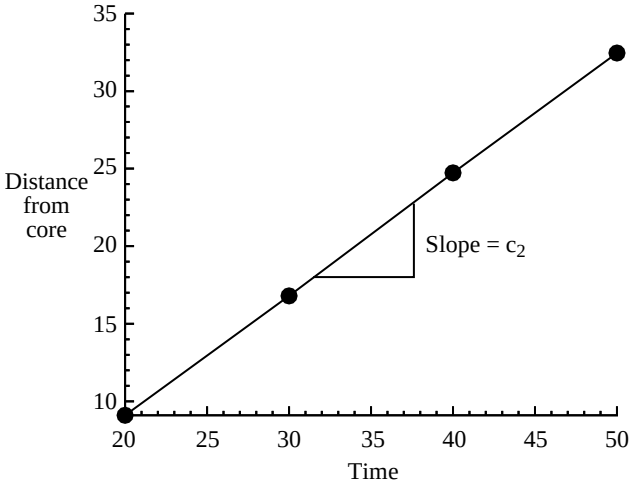

Figure 41. Peak pressure perturbation as a function of time.

additional pressure perturbations are generated downstream of the shock. At $T = 8$ high amplitude pressure disturbances are seen just downstream of the shock. As time passes, these pressure disturbances travel downstream more rapidly than the vortex. Figure 41 shows a plot of the position of the peak pressure as a function of time. The plot shows a linearly increasing change in the position of the pressure disturbance as a function of time, which means that the pressure disturbance is traveling at a constant speed relative to the vortex. The slope of this curve is found to be $\Delta R/\Delta T = 0.77$ core radii per period, which is the sound speed downstream of the shock. (The velocity 0.77 core radii per period is equivalent to a velocity normalized by the sound speed upstream of the shock of 1.15. The ratio of the sound speeds across the shock is 1.15 for an upstream Mach number of 1.5.) Thus, the pressure disturbances are traveling at the sound velocity relative to the mean flow, satisfying one of the defining features of acoustic waves.

The structure of the acoustic wave is readily apparent at $T = 50$ in figure 40. As predicted in linear theory, the sound wave is quadrupole in nature. The acoustic wave front is composed of alternate compression and rarefaction fronts.

Pressure perturbations along radii extending from the vortex center at 10° increments are shown in figure 42. This figure quantifies the change in amplitude as a function of the angle from the horizontal and shows that the peak-to-peak pressure amplitude is maximum at $\Theta = 50°$ and $\Theta = -55°$. From this figure, the peak-to-valley measure of the wavelength of the pressure disturbances is seen to be $\lambda \approx 2.8$.

Figure 43 shows a carpet plot of the pressure levels downstream of the shock at $T = 50$. The image is processed with the Fast computer software (ref. 61) and is shown at an angle to clarify the detailed features of the flow field. Note the resolution of the cylindrical acoustic wave and the complex system of pressure waves between the shock and the cylindrical acoustic wave front.

Figure 44 shows the product of the square root of the distance the acoustic wave has traveled (relative to the vortex core) and the peak pressure amplitude along a line extending from the vortex core at 60° from the horizontal passing through the vortex filament as a function of distance from the vortex filament. The product varies significantly at small distances from the core, which is synonymous with early time and proximity to the source, but flattens to an almost constant level at larger distances. This behavior of the product shows that in the far field, the sound pressure decays as $1/\sqrt{r}$, which is characteristic of geometrical spreading in two dimensions (cylindrical spreading). Although these calculations are performed in an axisymmetric coordinate system, which should allow for three-dimensional geometrical spreading of the sound, the presence of the shock wave prohibits the spreading upstream. In

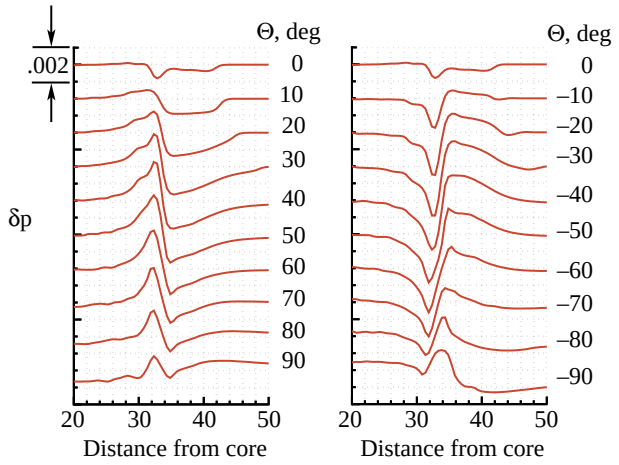

Figure 42. Pressure perturbations along radii extending from vortex core at $x = 30$.

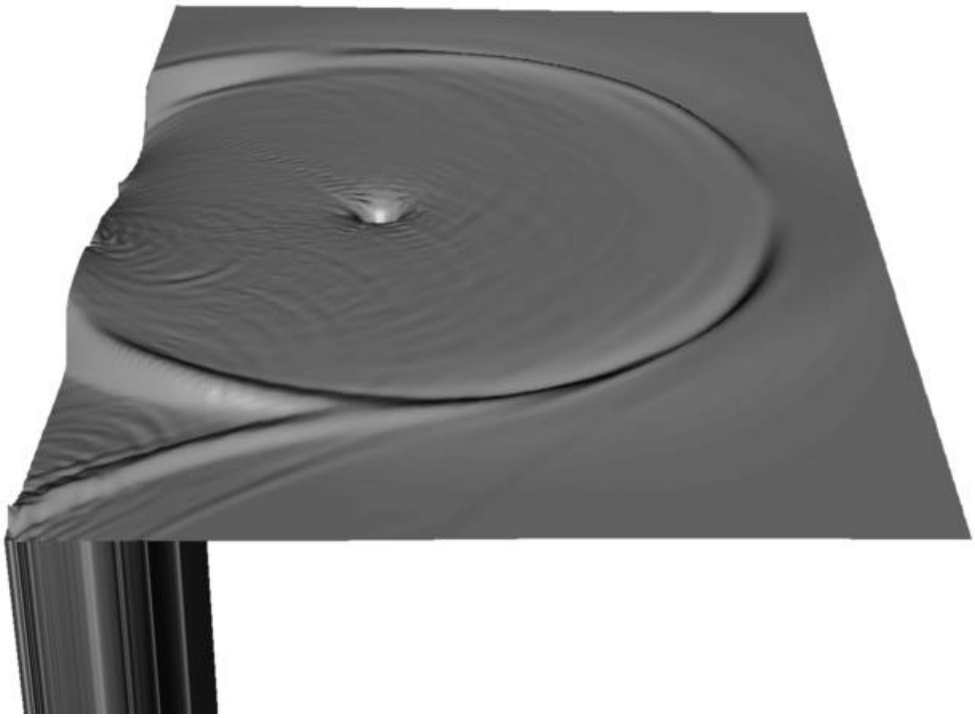

Figure 43. Pressure perturbations downstream of shock at $T = 50$.

realistic flows, where viscosity plays a role in the fluid dynamics, shock waves are finite in extent. In these model flows, cylindrical spreading would occur close to the shock wave, while spherical spreading (with p decaying as $1/r$) would occur in the far field. Hardin has shown that in cylindrical coordinates, the sound decay rate is a function of the source size to the distance from the source to the observer (ref. 62). In the section "Shock Dynamics," it will be shown that the interaction of the vortex ring and shock wave produces a disturbance that travels along the shock, thereby increasing the size of the potential noise source with increasing time.

A cusp-shaped pressure wave in the pressure field, which results from the ring vortex and shock interaction, is apparent in the flow field downstream of the shock and below the vortex filament. The ring vortex and shock interaction produces not only the acoustic quadrupole, but also a cusp-shaped

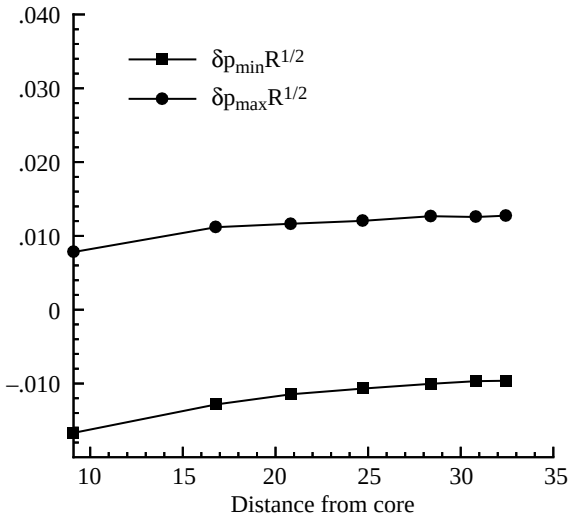

Figure 44. Decay rate of acoustic pressure.

pressure wave that connects the portion of the acoustic wave immediately below the vortex filament and the shock wave. This feature was not found in columnar vortex and shock interaction studies and appears to be sensitive to the introduction of the initial condition (refs. 46, 49, 50, 51, 55, and 56). Because of computational cost, the vortex is introduced seven core radii upstream of the shock for most of the calculations presented in this paper. However, to test the effect of the initial distance between the vortex and the shock wave, Δx_1 on the flow field downstream of the shock, a single calculation is presented where the vortex is initially 23 core radii upstream of the shock. Figure 45 shows the solution downstream of the shock at times $T = 50$ and $T = 66$ for initial shock locations of $x = 7$ and $x = 23$, respectively. In both of these cases the vortex has traveled approximately 23 core radii after its filament has passed through the shock wave. The cylindrical portion of the pressure field is similar for both initial conditions; however, there are differences in the downstream flow field. Most notably, the cusp-shaped pressure structure is much larger for the longer time solution ($\Delta x_1 = 23$), which indicates that it originates at the beginning of the computation. Further study of this feature is required to quantify the effect of axisymmetry and the initial condition on its structure, and to determine whether it is numerical or physical in nature.

Density

Figure 46 shows the change in density of the flow field. At time $T = 0$ the only change in density is associated with the vortex. As the vortex core begins to interact with the shock, density waves appear downstream of the shock. The interesting character of the density waves becomes clear in the final figure of the time sequence. Two types of density perturbations are evident in the figure. Density disturbances associated with the acoustic wave propagate in a nearly circular pattern downstream of the shock. This is to be expected, because acoustic waves are by definition isentropic and there is a clear relationship between the density and pressure (s = constant = p/ρ^{γ}). In addition, there are also convective density disturbances. These density disturbances look like spokes reaching out from the vortex core and terminating at the shock. These disturbances are associated with the entropy waves that are associated with changes in the shock strength. As the vortex interacts with the shock, the shock wave begins to move. As the shock moves, the change in entropy across the shock is no longer constant and an entropy wave is generated that convects downstream at the local flow velocity. For the counterclockwise rotating vortex, the portion of the shock above the vortex filament initially moves upstream and the portion of the shock below the filament moves downstream. As time increases, disturbances move away from the interaction point and their motion along the shock wave creates entropy perturbations that convect

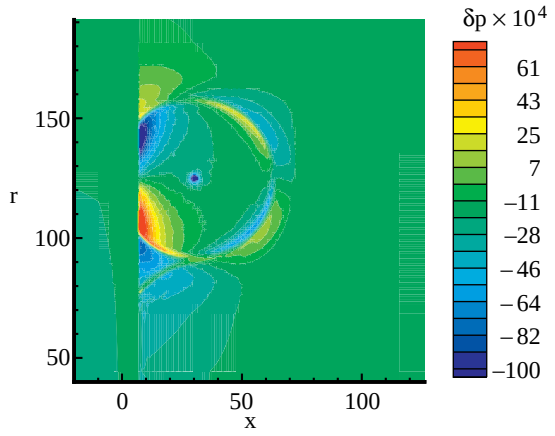

(a) Vortex initially 7 core radii from the shock at $T = 50$.

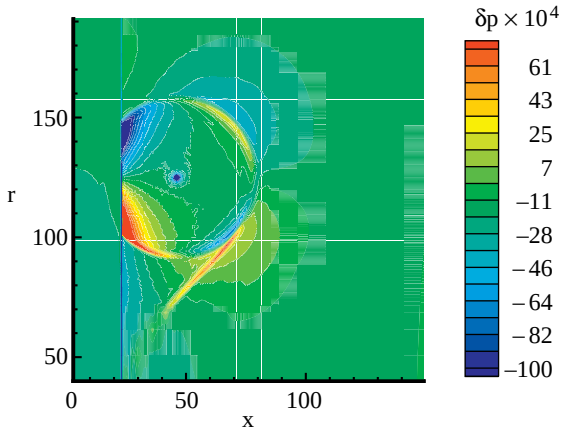

(b) Vortex initially 23 core radii from the shock at $T = 66$.

Figure 45. Pressure contours downstream.

downstream at the local flow velocity. These disturbances show a strong resemblance to the features observed by Naumann and Hermanns and described as contact surfaces (ref. 46).

Figure 47 shows a digitized version of a Mach-Zehnder interferogram from reference 46 that illustrates the sound wave and contact surface observed in the experiment. In the experiment, the interaction is produced as follows. A sharp edged profile is placed in a shock tube. A diaphragm (located to the left of the airfoil) is broken and a weak disturbance travels through the tube and over the trailing edge, which produces a starting vortex. Another diaphragm (located at the right of the airfoil) is broken and a shock wave travels towards the vortex. The results of the interaction are shown in figure 47. Because the interaction observed in this experiment is strong, the motion of the shock wave is pronounced and the acoustic wave front is asymmetrical. The contact surfaces form a curved funnel-shaped structure between the shock wave and the vortex.

Figure 48 shows a carpet plot of the density at $T = 50$. The sound wave and complex nature of the contact surfaces are clearly visible. Experiments provide evidence for the physical nature of the contact surfaces observed in these computations. However, earlier analysis in chapter 3 demonstrated that the computation of slowly moving shock waves produces error that manifests itself primarily in entropy. Therefore, caution must be exercised in the interpretation of the strength of these disturbances. Further analysis is required before the nature of these contact surfaces is validated.

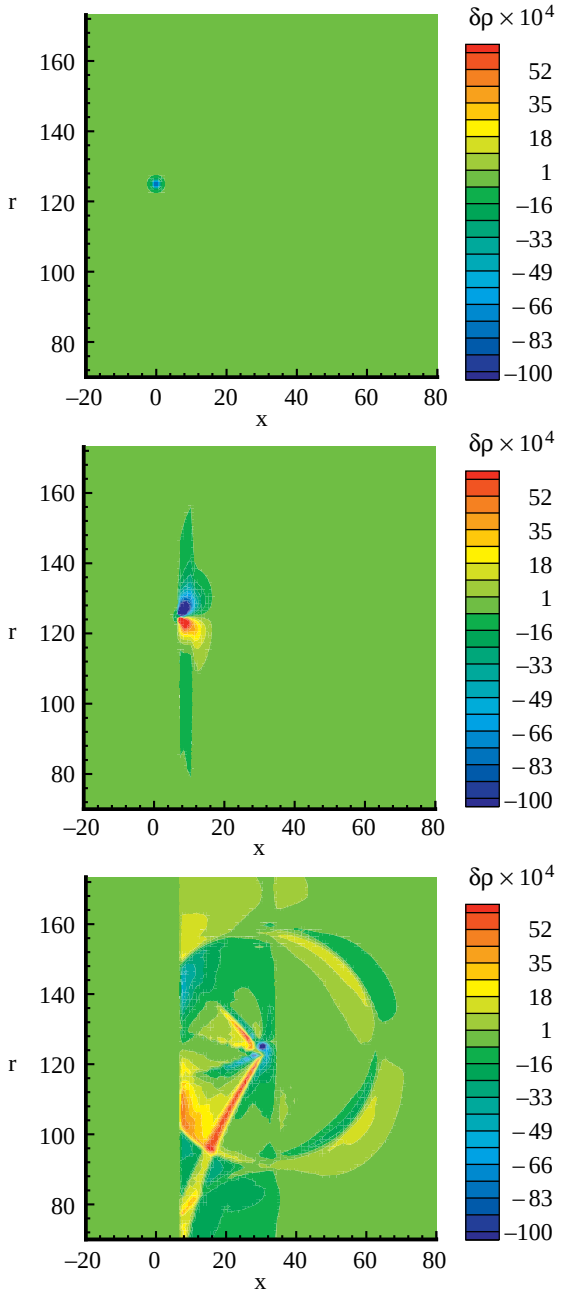

Figure 46. Contours of density perturbation downstream of shock at $T = 0$, $T = 8$, and $T = 50$.

Vorticity. Figure 49 shows the change in vorticity. At the initial time, the only vorticity is a circular spike at the vortex core; therefore, this contour plot is not shown. As the vortex interacts with the shock at $T = 8$, vorticity appears downstream. At $T = 50$, the vorticity becomes clearer. The vorticity patterns, like the convective density disturbances, look like the spokes of a wheel radiating from the vortex core and terminating at the shock. Looking closely at a region in the immediate vicinity of the vortex core at $T = 50$, it is clear that the lines of constant vorticity are oblong in shape (fig. 50).

Velocity. Figures 51 and 52 show the changes in the axial and radial components of velocity. Except for small changes in amplitude, the velocity field shows no significant variation as a result of the interaction on this scale. There are, however, features similar to those observed in the density perturbations

Figure 47. Mach-Zehnder interferogram of sound wave and contact surfaces generated shock and vortex interaction. (From ref. 46.)

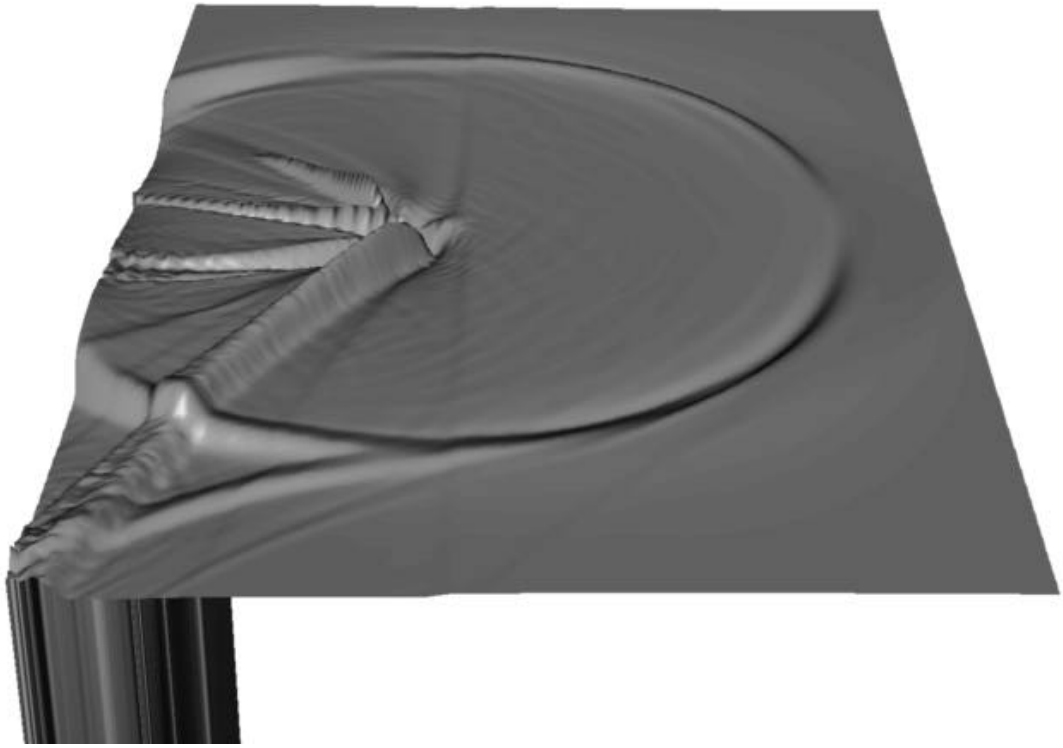

Figure 48. Contours of density perturbation downstream of shock at $T = 50$.

when the contour range is decreased. Figure 53 shows the change in the axial component of velocity on a smaller contour range. The vortex, acoustic wave, and entropy disturbances are all readily distinguished on this scale.

Entropy. Figure 54 shows the change in entropy, which is defined as $\delta s = s_o(p/\rho^\gamma) - s_0$. At the initial time, there is no fluctuation in entropy, since the initial vortex is isentropic. Therefore, the contour plot at $T = 0$ is not shown. However, as the vortex core interacts with the shock wave, entropy appears

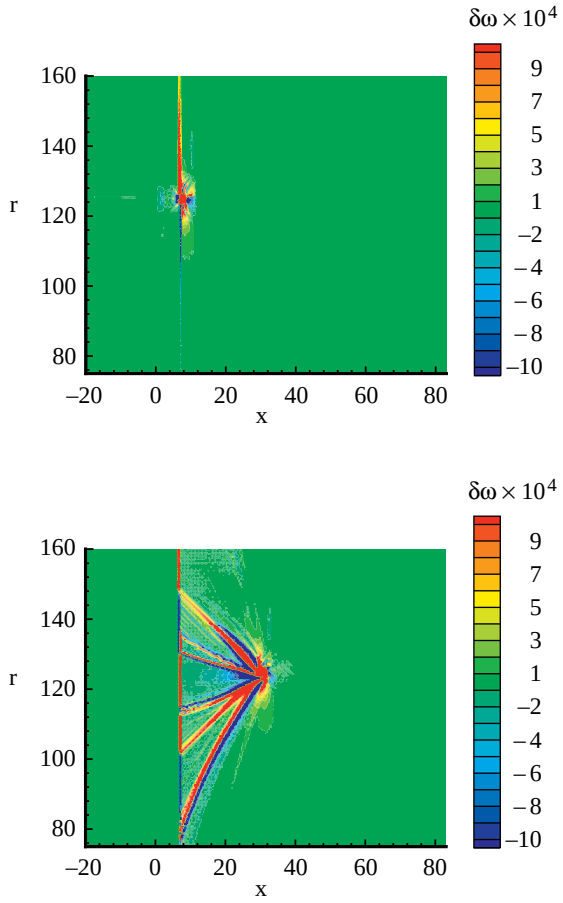

Figure 49. Contours of vorticity perturbation downstream of shock at $T = 8$ and $T = 50$.

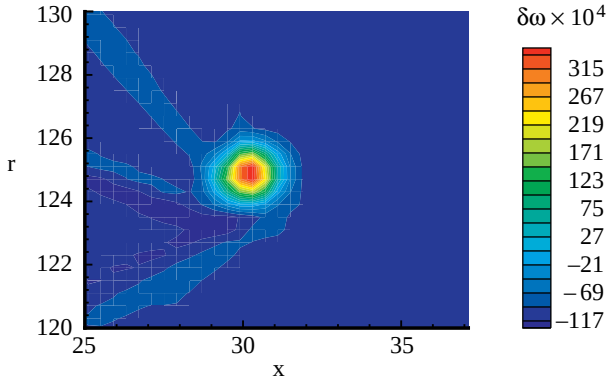

Figure 50. Contours of vorticity perturbation in region immediately surrounding vortex filament at $T = 50$.

downstream. Note that the entropy perturbations correspond to the convective fluctuations in density and vorticity as shown in figures 46 and 49.

Flow features. Figures 40 through 54 illustrate flow features that result from the interaction of a ring vortex and a shock wave. After observing the perturbations in the flow quantities, it is clear that an acoustic wave and contact surfaces result from this interaction. The acoustic wave is isentropic and

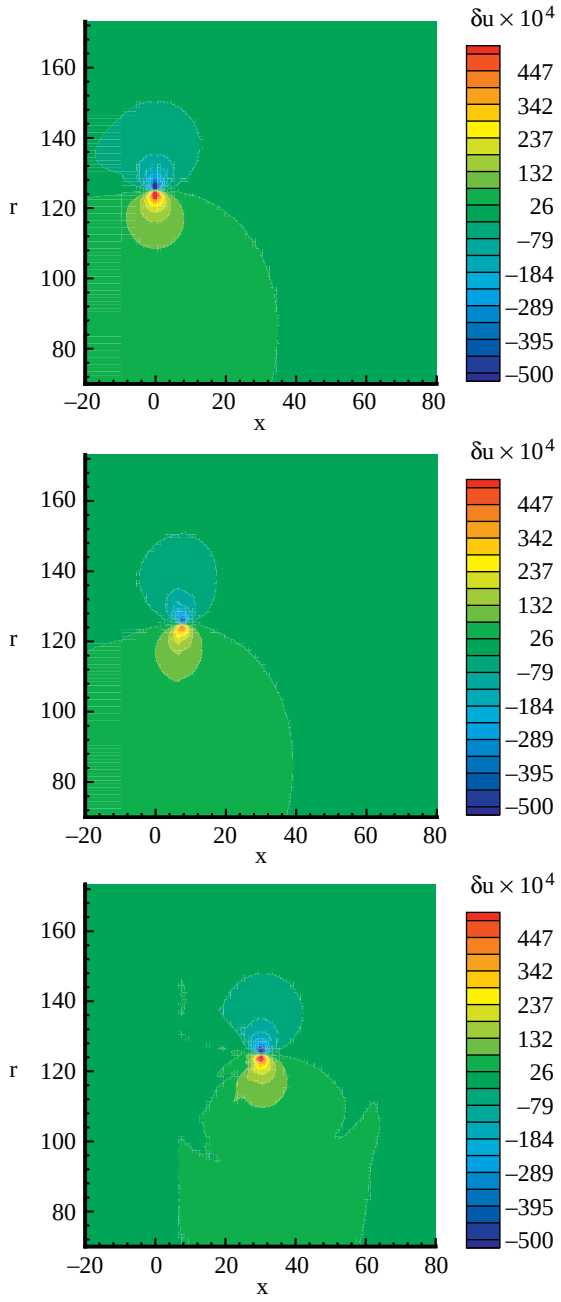

Figure 51. Contours of axial velocity perturbation of shock at $T = 0$, $T = 8$, and $T = 50$.

travels at the sound speed relative to the moving fluid. The contact surfaces do not support a pressure disturbance, but do support differences in flow velocity, density, entropy, and vorticity. The disturbances are the result of the interaction. From a mathematical perspective, the shock wave is the feature that allows for the coupling of the linear modes (acoustic, entropy, and vorticity). Crocco's theorem provides the relationship between the flow vorticity and entropy. From this theorem it can be shown that vorticity can be generated in the presence of a curved shock. Because the evidence points to the importance of the shock wave in the generation of the acoustic, vortical, and entropy disturbances, a closer observation of the shock dynamics will be made in the next section.

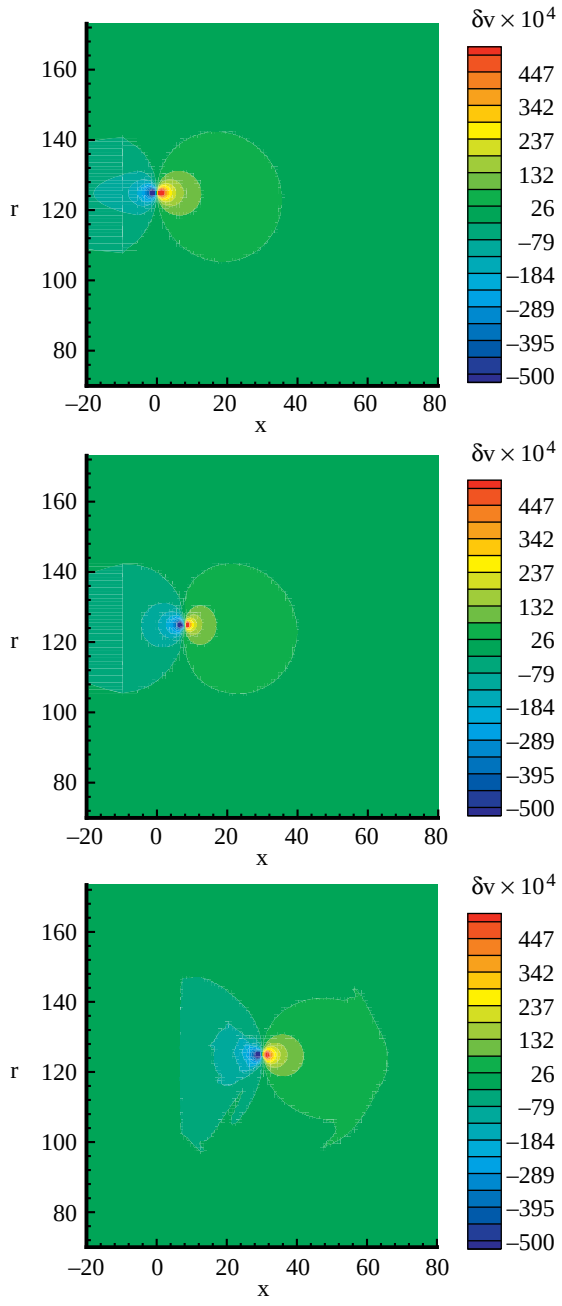

Figure 52. Contours of radial velocity perturbation downstream of shock at $T = 0$, $T = 8$, and $T = 50$.

Shock dynamics. Figure 55 shows a space and time diagram of the shock displacement. For times $T = 0$ through $T = 6$ the shock position remains nearly fixed as the vortex convects supersonically towards it. Once the vortex core begins to strongly interact with the shock at $T = 6$, the shock motion becomes significant. Figure 55 illustrates the nature of the shock displacement as a function of time. A small disturbance on the shock is initiated at $T \approx 6$. The disturbance proceeds to travel both away from and towards the axis of symmetry. The speed of these waves is approximately the same in both directions, but the disturbance reaches a local maximum away from the axis of symmetry and continues to grow towards the axis of symmetry.

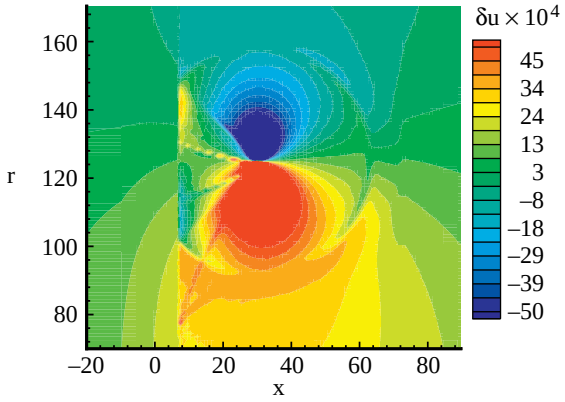

Figure 53. Contours of axial velocity perturbation at $T = 50$ with range of contour levels reduced to show velocity features.

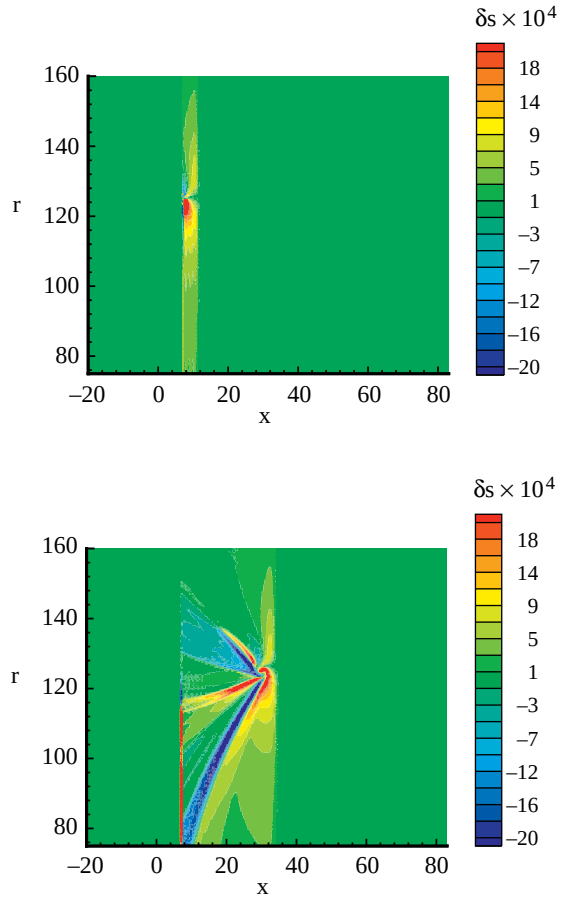

Figure 54. Contours of entropy perturbation at $T = 8$ and $T = 50$.

Figure 56 clarifies the details of the shock displacement at various times. This figure shows the axial displacement of the shock as a function of radial position along the shock for $T = 1$, $T = 6$, $T = 10$, $T = 20$, $T = 30$, $T = 40$, and $T = 50$. At $T = 10$, the shock wave has maximum displacement magnitudes of 0.1 and 0.14 in the upstream and downstream directions, respectively. At this early time, the displacement of the shock is limited to a small region around $r = 125$, which is the radial position of the vortex filament. As time progresses, the maximum shock displacement occurs farther away from the

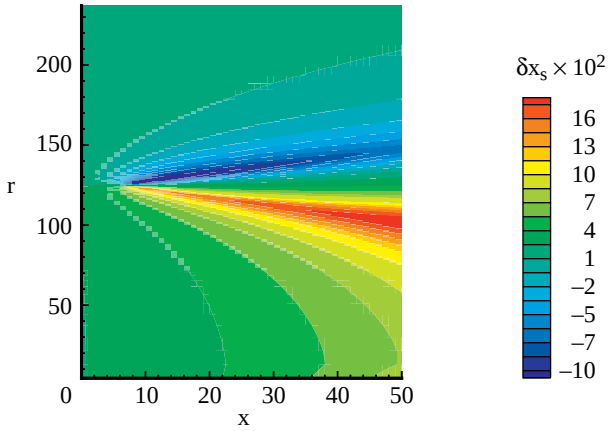

Figure 55. Shock displacement as a function of space and time.

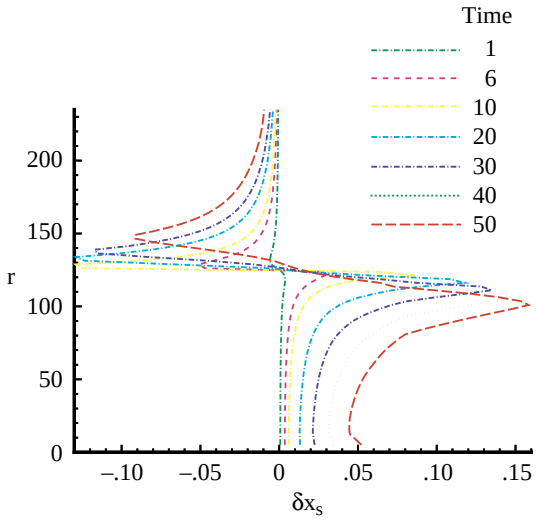

Figure 56. Shock displacement for $T = 1$, $T = 6$, and $T = 10$ through $T = 50$. Positive displacement refers to downstream shock displacement.

interaction point. The maximum upstream displacement occurs at a time of $T \approx 10$. However, the displacement in the downstream direction continues to increase, even after 50 periods. If the motion of the maximum shock is considered to be displacements along the shock wave, it is apparent that these disturbances travel away from the vortex and shock interaction point at a particular velocity. By careful examination of the results presented in figure 55, this velocity is found to be ≈ 0.54 core radii per period (which corresponds to a normalized velocity of ≈ 0.68 core radii per period). This velocity is well below both the upstream and downstream sound speeds (1.0 and 1.15, respectively).

The shock wave displacement continues to increase in the direction towards the center of the ring, while it maximizes and then decreases in the direction away from the axis of symmetry of the ring.

Figures 55 and 56 show the asymmetry in the shock position relative to an axis passing through the vortex filament position at $r = 125$. The portion of the shock closest to the axis of symmetry continues to move downstream over the time of the calculation. The maximum shock displacement is greater downstream ($\Delta x_s = 0.16$) than upstream ($\Delta x_s = -0.1$).

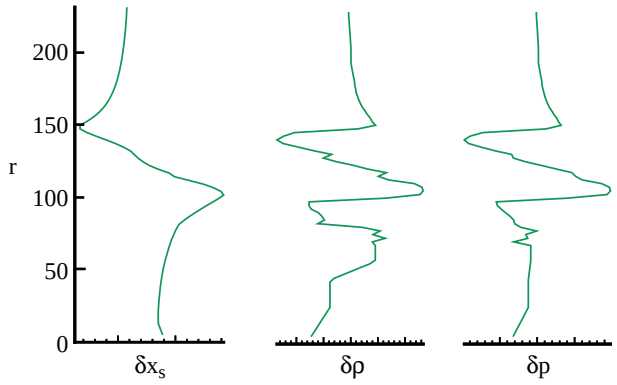

Figure 57. Shock displacement and density and pressure perturbations for $T = 50$. Density and pressure perturbations were obtained slightly downstream of the shock ($x = 7.02$).

Figure 57 shows the displacement of the shock and the perturbation in density and pressure immediately downstream of the shock at $x = 7.02$ at $T = 50$. This figure shows that there is a correlation between the disturbances downstream of the shock and the shock displacement. The shock displacement leads the disturbances in pressure and density. The maximum and minimum of the shock displacement correspond to the large jumps in density at $r = 100$ and $r = 150$. The changes in slope of the δx_s and r curve that are located at $r = 70$, $r = 120$, and r = 130 also correspond to significant high frequency changes in density. This type of fluctuation in pressure occurs only at $r = 70$. Thus, by comparing this figure with the contour plots of figures 40 and 46, the spoke-like disturbances in density and vorticity can be related directly to the shock motion and curvature.

Frequency analysis. To obtain information about the frequency content of the solution, the fast Fourier transform (FFT) is used to determine the time dependent information obtained from the numerical calculation to the frequency domain:

$$P(\omega) = \int_{-\infty}^{+\infty} \delta p(t) e^{-i\omega t}\, dt \tag{105}$$

where δp is the perturbation pressure defined as the difference between the pressure and the mean pressure ($\delta p = p - p_0$), t is time, and ω is the cyclic frequency.

This integral is written in discrete form

$$P \approx \Delta t \sum_{n=0}^{N-1} p(n\Delta t) e^{-i\omega n \Delta t} \tag{106}$$

where Δt is the discrete time interval of the discrete pressure time history $p(n\Delta t)$, and N is the number of points in the time history. Equation (106) is computed using the FFT. To efficiently use the FFT, N must be a power of 2.

In this numerical simulation, solutions were saved at every period (defined as $T = r_c/u_1$). Thus, there are 50 discrete representations of pressure in the time history that are available for analysis at each point in the computational domain. To effectively use the FFT approach, the time history at each point at which the spectrum is to be computed is padded with zeros so that the number of discrete values in the time history is a power of two. Padding the time history with zeros does not affect the highest frequency that can be resolved in a discrete approximation to the Fourier transform (the Nyquist frequency), since the Nyquist frequency ω_c is a function only of the temporal increment in the time history $\omega_c = \pi/\Delta t$.

However, padding the time history with zeros does increase the frequency resolution of the spectral estimate.

The increase in frequency resolution provided by zero padding is readily illustrated by an example (ref. 34). Suppose the original time history T has b elements: $T(n\Delta t)$, $n = 0,1,2,...,b-1$. The original time history is then padded with additional b elements, which are zero: $T(n\Delta t) = 0$, $n = b, b+1,...,2b-1$. The discrete Fourier transform T_T is then

$$T_T(\omega_k) = \frac{\Delta t}{2\pi} \sum_{n=0}^{2b-1} T(n\Delta t) e^{-i2\pi kn/2b}$$
$$= \frac{\Delta t}{2\pi} \sum_{n=0}^{2b-1} T(n\Delta t) e^{-i\pi kn/b} \tag{107}$$

Note that $\omega_k = \pi k/b\Delta t$, $k = 0,1,2,...,b$, and the frequency resolution is $\Delta\omega = \pi/b\Delta t$. Similarly, for the original time history without zero padding, $\omega_k = 2\pi k/b\Delta t$, $k = 0,1,2,...,b/2$, and the frequency resolution is $\Delta\omega = 2\pi/b\Delta t$. Thus, the zero padding has the effect of increasing the frequency resolution by a factor of two.

Although it would be sufficient to pad the 50-element time history with 14 zeros to obtain a 64 element time history, each time series was padded with 206 zeros for a total of 256 points in the time history. This number of zeros provided better frequency resolution that was necessary for localization of the acoustic energy in the spectrum. The price paid for enhanced frequency resolution is a loss of accuracy. (See ref. 34 for details.)

Typical sound pressure levels are presented in figures 58 and 59. The frequencies are normalized by the upstream flow velocity and core radius to obtain a Strouhal number. In these figures, the effect of the mean flow has been removed from the spectra by subtracting the time average of the pressure from each point in the time history. This subtraction removes the energy from the zero frequency bin. The sound pressure level is presented in decibels (dB). The decibel level is obtained by computing

$$P(\omega) = 20 \log\left[\frac{P(\omega)}{p_{\text{ref}}}\right] \tag{108}$$

where $p_{\text{ref}} = 20\mu Pa$ is the conventional acoustic reference pressure.

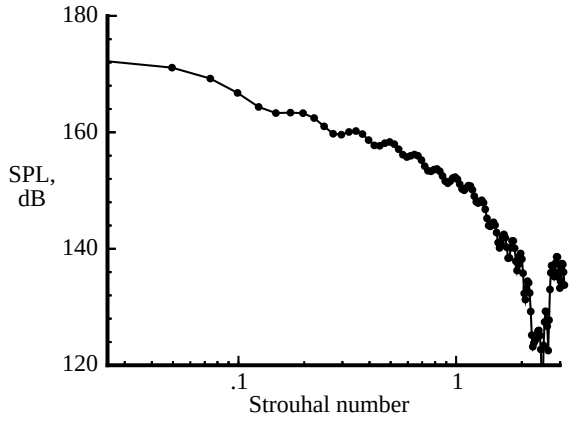

Figure 58. The SPL at 6.0811 core radii from source and 45° from horizontal as a function of dimensionless frequency.

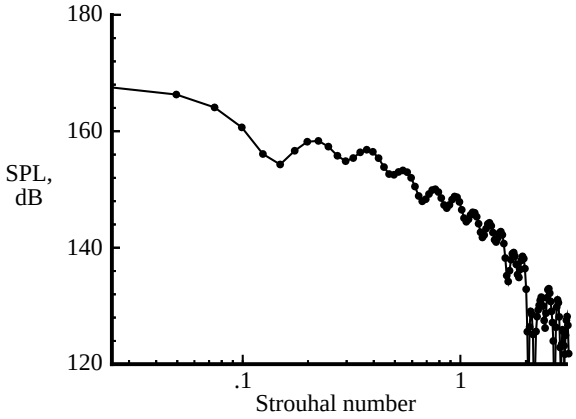

Figure 59. The SPL at 11.74 core radii from source and 45° from horizontal as a function of dimensionless frequency.

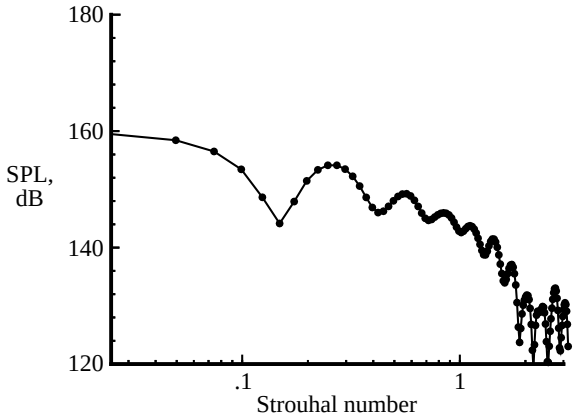

Figure 60. The SPL at 23.1 core radii from source and 45° from horizontal as a function of dimensionless frequency.

Figures 58 through 60 show the sound pressure level at locations along a 45° line from the sound source point ($x = 7$, $y = 125$) at 6.08, 11.74, and 23.1 core radii away from the source point. The highest energy levels are in the low frequency range (Strouhal numbers less than 0.1). There are additional peaks at Strouhal numbers of ≈ 0.2, 0.4, and 0.6. The energy in the frequency band of about 0.22 becomes relatively more important than the low frequency energy as distance from the source point is increased. By observation of the time history from which the spectrum is computed, the period of the acoustic wave is determined to be approximately 21 periods. This period corresponds to a Strouhal number of $\omega r_c/u_1 = 2\pi r_c/Tu_1 = 2\pi 1/21(1.5) = 0.2$. Thus, the energy in the frequency range of 0.22 is associated with the acoustic energy of the signal. The large peaks near the Nyquist frequency (Strouhal number = π) are probably due to aliasing. Hardin has shown that for spectral estimates near the Nyquist frequency ω_c contributions from $-\omega_c$ can appear, even for a sufficiently sampled time history (ref. 57). Figure 61 shows the sound pressure level of the two frequencies 0.025 and 0.2 as a function of distance from the sound source point. The data are taken along a 45° line from the horizontal that passes through the vortex core at $r = 125$. The data show a rapid decay in the energy associated with the low frequency energy. The energy decays at about 6 dB per doubling of distance away from the source. This implies a decay rate of $1/r^2$, which is consistent with the expected decay rate for a vortical pressure field.

The energy at the Strouhal number of 0.22 decays at a lower rate of ≈ 3 dB per doubling of distance, which implies a sound pressure level decay of $1/r$. Because the sound pressure level is a function of the square of the pressure, this result is consistent with the pressure decay rate of $1/r^{1/2}$ that was discussed in the section entitled “Pressure” and implies cylindrical spreading of the acoustic energy.

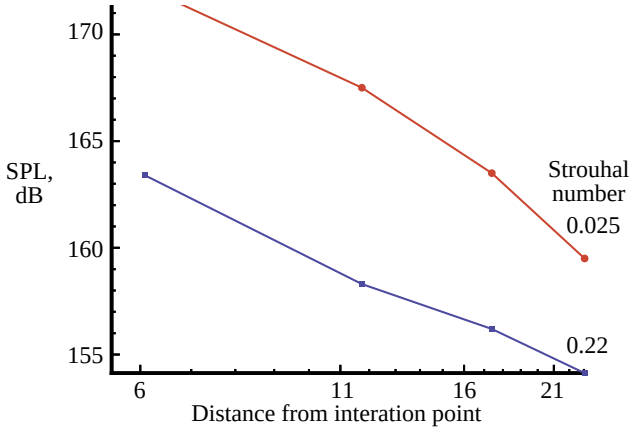

Figure 61. The SPL at 45° from point where a horizontal line passing through vortex filament (r = 125) passes through undisturbed shock.

Sound intensity level. The sound intensity is a vector quantity defined by

$$\mathbf{I}(\mathbf{x}) = \frac{1}{T}\int_0^T \mathbf{W}\, dt \tag{109}$$

where T is the period of a periodic disturbance or a sufficiently long time for nonperiodic bounded signals and $\mathbf{W}$ is the instantaneous acoustic energy flux vector

$$\mathbf{W} = (\delta p + \rho_0 \mathbf{U}_0 \cdot \delta\mathbf{u})\left(\delta\mathbf{u} + \frac{\delta\rho}{\rho_0}\mathbf{U}_0\right)$$

where $\mathbf{U}$ is velocity and δp, δu, and $\delta\rho$ are disturbances in pressure, velocity, and density, which are defined

$$\begin{aligned} \delta p &= p - p_0 \\ \delta\mathbf{u} &= \mathbf{u} - \mathbf{u}_0 \\ \delta\rho &= \rho - \rho_0 \end{aligned}$$

and the subscript 0 represents the mean flow state.

Note that in a quiescent medium (where $\mathbf{U}_0 = 0$), three of the terms in the instantaneous acoustic energy flux vector vanish and the equation for sound intensity reduces to

$$\mathbf{I}_c(\mathbf{x}) = \frac{1}{T}\int_0^T \delta p\,\delta\mathbf{u}\, dt \tag{110}$$

Because early acoustics theory was developed for sound disturbances in a quiescent state, this definition will be called the “classical” definition of sound intensity and it will be labeled with a subscript c to distinguish it from the definition of intensity presented in equation (109). It will be shown later that it can be beneficial to consider the classical definition of sound intensity, even in the presence of mean flow.

In the calculations performed here, the acoustic signal is transient, which provides some difficulty in the interpretation of sound intensity. Because this problem models the periodic convection of turbulent disturbances through a shock wave, the interpretation taken here is to use the length of time of the transient disturbance as the period of a signal. This interpretation assumes that sound waves generated

by periodically convecting disturbances do not overlap and the time between pressure disturbances is equal to the time of the transient.

Once the sound intensity is computed and dimensionalized, the sound intensity level is determined by the relation

$$IL = 10 \log \frac{\mathbf{I}}{I_{\text{ref}}}$$

where $I_{\text{ref}} = 10^{-12}$ watts/m^2. To dimensionalize the calculations, standard sea-level conditions are used; the upstream stagnation sound speed is 340 m/s and upstream static pressure is 101 325 N/m^2.

It is important to state that the computation of the sound intensity vector will *not* guarantee that the result is all *sound*. It is difficult, if not impossible, to separate the acoustic fluctuations from hydrodynamic fluctuations in the near field of the sound source. The definition of the sound intensity vector can provide useful information regarding the strength and directivity of disturbances in the flow and will provide a useful description of the sound when the calculation is made in the far field.

Typical intensity plots are presented in figure 62, which shows the axial and radial components of the intensity vector for an upstream Mach number of 1.5 and a vortex strength of 0.75. The total time history in the calculation of the intensity components is $T = 50$.

These plots show two distinct regions of high intensity level. One region is along the path that the vortex travels after intersecting with the shock wave. This region is most clear on the plot of the axial component of intensity level. This region is not *sound* intensity, since most of the disturbances related to the vortex *convect*. The high intensity level shown in this region demonstrates the high correlation between the pressure and velocity disturbances in the vortex.

Some acoustical energy may be generated as the vortex changes shape after its interaction with the shock, but small scale vortical motions were not observed to be a significant sound source in these calculations. This insignificance is most clearly seen in figure 43, which shows a carpet plot of pressure fluctuations downstream of the shock. The most significant structure is the ring, which has already been identified with the interaction of vortex core with the shock wave. Much less significant pressure disturbances are seen in the center of this acoustic wave, but there are no waves visibly emanating from the vortex.

The other region of high intensity is visible along the shock wave. The intensity plots show that sound is directed primarily in directions closely aligned with the shock wave. The intensity originates at the point of interaction and travels both towards and away from the axis of symmetry. Both axial and radial components of intensity have high levels along the shock; the region is much narrower in the contour plot of the axial component. The high amplitude of these waves makes it difficult to classify them as acoustic in the classical sense, but because there is no convective velocity in the radial direction, these disturbances are clearly not convective.

A plot of the axial component of sound intensity that is determined by the classical definition is shown in figure 63. (Because the mean flow is in the axial direction only, the radial component of classical sound intensity is the same as that shown in fig. 62.) The region of high intensity in the vicinity of $r = 125$ is due to the passage of the vortex along this path. Figure 63 shows that the intensity has four lobes not related to the convection of the vortex. Two of these lobes are along the shock wave, similar to the results shown in figure 62. However, two additional lobes originate at the point of vortex filament and shock interaction and point at angles of approximately 50° and −55°. The lobe directed at −55° is narrower than the lobe directed at 50°. Note that these regions are not evident in the contours of the full description of the sound intensity (fig. 62) because the energy associated with the acoustics is overwhelmed by the contributions from the mean flow terms. The high intensity level along the lobes is

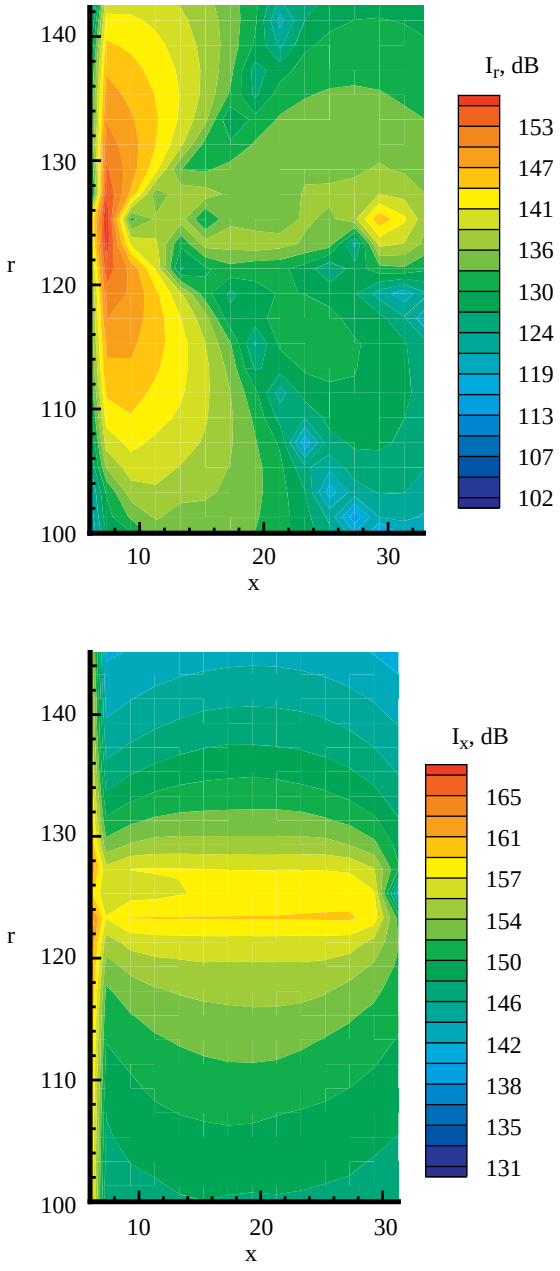

Figure 62. Sound intensity level.

significant because it corresponds to the location of the strongest region of the sound wave. (See fig. 42.) This correspondence indicates that it can be beneficial to consider the classical definition of sound intensity, even in the presence of a mean flow. It is legitimate to apply equation (110) as long as it is not used to draw conclusions about acoustic energy conservation.

Effect of Mach number on directivity. To determine the effect of Mach number on the directivity of the pressure disturbances, a series of computations was performed where all flow parameters were held fixed except the upstream Mach number. The preshock Mach numbers studied were M = 1.1, 1.3, 1.4, 1.5, and 1.7. These Mach numbers were chosen because they are within the range of practical interest. The sound intensity level was computed over this Mach number range. The directivity angles as a function of shock strength are plotted in figure 64. The figure shows the angles of the four primary beaming

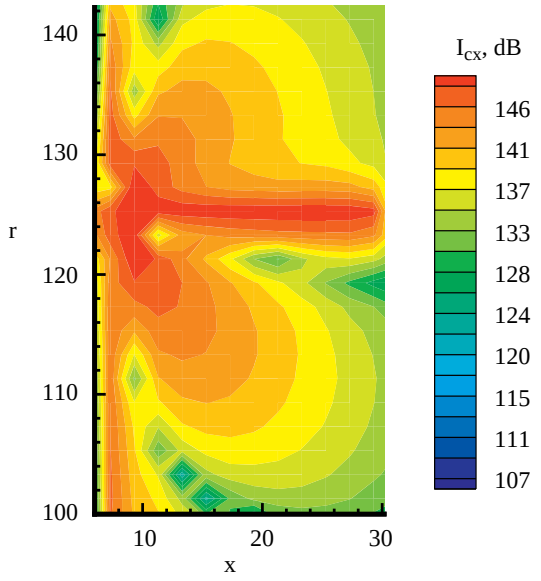

Figure 63. Sound intensity level with primary directivity of sound wave along shock wave and downstream at angles of ±50°.

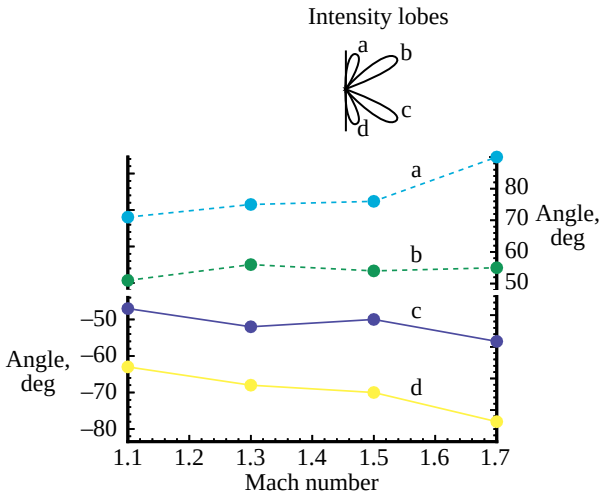

Figure 64. Directivity angles of primary intensity lobes as a function of upstream Mach number.

directions. The change in lobe direction is most significant for the lobes closely aligned along the shock. As the Mach number increases, these lobe angles approach ±90°.

Effect of flow Mach number on sound pressure level. Because of the complexities in defining and computing the sound intensity level for a transient signal in the presence of a mean flow and because the human ear responds to pressure fluctuations, a study of the effect of flow Mach number on the sound pressure level is presented here. In this study, sound pressure level is computed for a point in the acoustic far field (defined to be one wavelength away from the source) at a distance of 23 core radii from the interaction point at an angle of θ = 50°. In these calculations, the sound pressure level is computed by

$$\mathrm{SPL} = 20 \log\left(\frac{p_{\mathrm{rms}}}{p_{\mathrm{ref}}}\right) \tag{111}$$

where p_{ref} is standard reference pressure and

$$p_{rms} = \sqrt{1/T \int_0^T p^2 \, dt}$$

where T is the period of the acoustic signal. Because this calculation is performed in the far field, the acoustic wave is readily distinguished from hydrodynamic disturbances. The result of this study is presented in figure 65, which shows sound pressure level as a function of $\beta = \sqrt{M^2 - 1}$, for Mach numbers in the range $1.1 \le M \le 1.5$. Experimental measurements obtained by Seiner and Norum for shock noise of an underexpanded supersonic jet, which was measured at a distance of 12 ft from the jet centerline (145.6 jet radii from the source), but corrected to a distance of 0.188 jet radii for comparison with numerical computation are also presented in figure 65 (ref. 58). In addition, the trend that the sound pressure level of shock noise in imperfectly expanded supersonic jets is proportional to β^4 over a large range of flow Mach numbers, which was observed by Harper-Bourne and Fisher is also included in the figure (ref. 63). The slope of the sound pressure level and β^4 curve very nearly matches the slope of the experimental results for shock noise in supersonic jets. This similarity is significant because it shows that this simple model for shock noise generation can predict the effect of Mach number on shock noise that is observed in experiment.

Although this model correctly reproduces the trend in sound intensity level as a function of shock strength, it does not reproduce the actual sound amplitude even when differences in the distance between the sound source and measurement location are accounted for. This lack of reproduction is not surprising since shock noise measured during an experiment is the result of many interactions of turbulent structures of a variety of sizes and strengths with a sequence of shock waves of decaying strength and at varying angles to the flow.

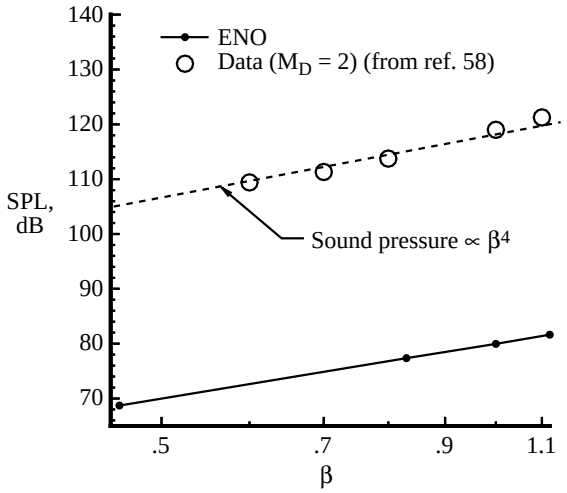

Figure 65. The SPL as a function of upstream Mach number.

Strong Interaction

The results presented in this section are for the interaction of a strong vortex with a shock wave. For all the results presented in this section, the upstream Mach number is 1.5 and the strength of the vortex is $\Gamma = 5.5$. Thus, this vortex is 7 1/3 times stronger than the vortex studied in the previous sections. When the vortex strength increases, the pressure disturbances generated downstream of the shock increase in magnitude, which shows contour plots of the pressure disturbances at $T = 50$ (fig. 66). The

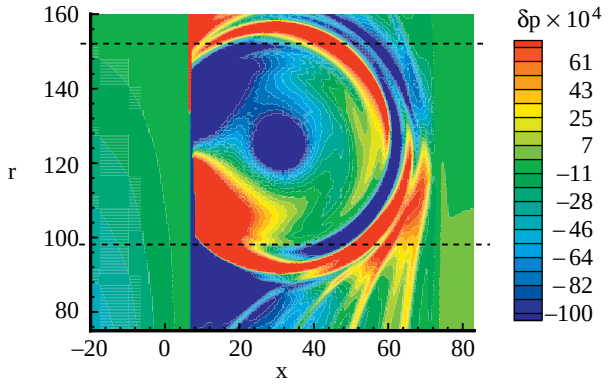

Figure 66. Contours of pressure perturbation downstream of shock at $T = 50$ and $\Gamma = 5.5$.

actual range of the pressure disturbances are on the order of 1, but for the plot, the range of contours was chosen to be from −0.01 to 0.007 so that direct comparison with figure 40 can be made. In both figures, a sound wave and a cusp-shaped pressure disturbance are apparent on the side of the vortex filament closest to the axis of symmetry and downstream of the shock. However, the sound wave is much stronger in the strong vortex and shock interaction case, and on this plot contour scale, additional pressure structures are visible downstream and below the vortex filament (fig. 66).

Figure 67 shows pressure perturbation along radii extending from the vortex center at 10° increments. This figure shows that the peak-to-peak pressure amplitude is a maximum at 55° and −55°, as in the case for $\Gamma = 0.75$. From this figure, the peak-to-valley measure of the wavelength is found to be ≈ 2.5. In comparison with figure 42, the disturbances for the strong vortex interaction case are almost an order of magnitude larger. For example, the amplitude of the peak disturbance at 50° is 10.2 times larger for the strong interaction case ($\Gamma = 5.5$) than the weak interaction case ($\Gamma = 0.75$). Thus, the acoustic pressure p scales as the vortex strength Γ.

Note that the pressure disturbances immediately downstream of the shock form very steep gradients. These gradients may be considered to be shock waves and have been referred to as “reflected shocks” (ref. 10). Figure 68 shows the distribution of perturbation pressure as a function of distance from the initial shock position at locations above and below the vortex filament. There are significant

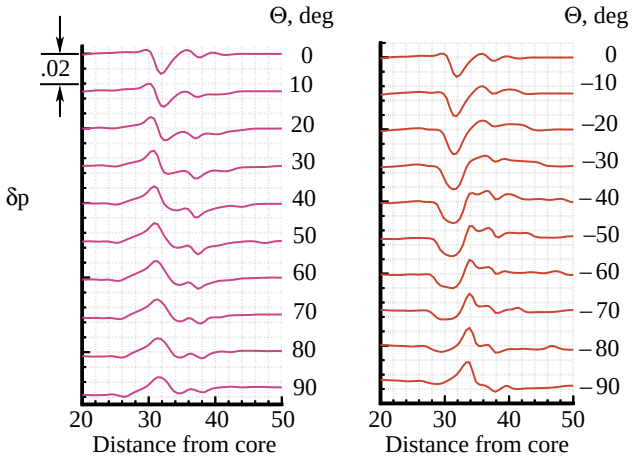

Figure 67. Pressure perturbations along radii extending from vortex core with $\Gamma = 5.5$ at $x = 30$.

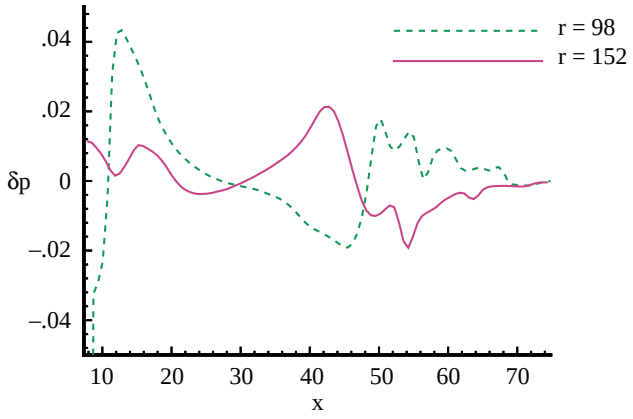

Figure 68. Pressure perturbations as functions of axial position at $T = 50$.

jumps in pressure downstream of the original shock wave, especially below the vortex filament. The formation of steep gradients downstream requires that the algorithm used in the calculation be robust.

Figure 69 shows contours of the density perturbations downstream of the shock. The same features present in the $\Gamma = 0.75$ case are present here, but the strength of these features is now enhanced.

Typical Interaction of Clockwise Vortex

In this section, results are presented for the interaction of a clockwise rotating vortex with a shock. This case is not representative of the physics of the interaction of vortices in the jet shear layer with shock waves, but is included for completeness. This interaction could model wake flow and shock interaction, such as the wake of a helicopter blade interacting with a shock on the subsequent blade.

Figure 70 shows contours of pressure for the vortex rotating clockwise with a shock wave. The strength of the vortex is $\Gamma = -0.75$ and the Mach number upstream of the shock is $M = 1.5$.

Note that this case is directly analogous to the case presented in the section entitled “Strong Interaction” except for the sign of the vortex circulation. Comparison of figure 70 with figure 40 shows that the contours of pressure perturbation are quite similar except that the regions of compression in figure 70 are regions of rarefaction in figure 40. The difference in the rotation sense of the vortex results in a different response of the shock wave, which in turn results in a difference in the sign of the pressure disturbance downstream. As shown in figure 55, a CCW rotating vortex causes the shock to move upstream in the region above the votex filament and to move downstream in the region below the vortex filament.

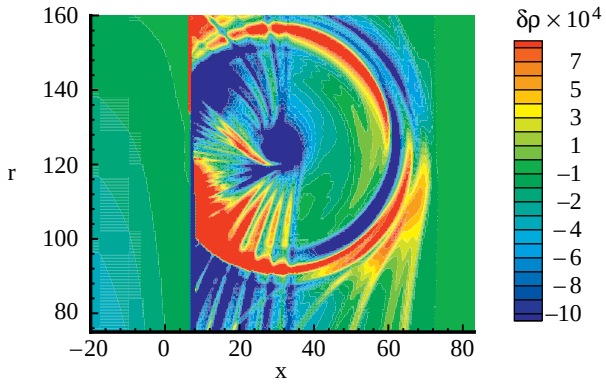

Figure 69. Contours of density perturbation downstream of shock at $T = 50$ and $\Gamma = 5.5$.

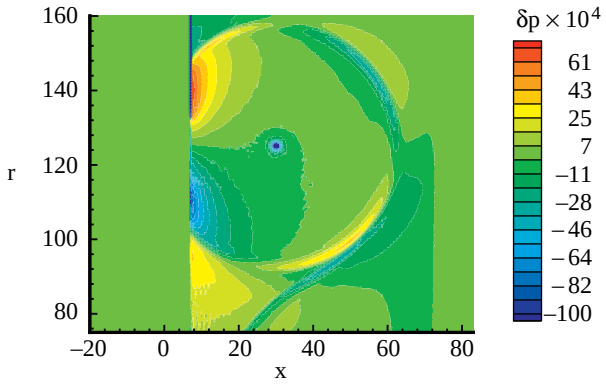

Figure 70. Contours of pressure perturbation downstream of shock at $T = 50$.

For the clockwise rotation, the shock wave moves downstream in the region above the vortex filament and upstream in the region below the vortex filament, as shown in figure 71. Figure 72 clearly shows that the shock displacement is significantly greater upstream than downstream.

The downstream pressure disturbances resulting from the CW and CCW vortices are not perfect images of each other about the vortex filament. The cusp-shaped structure described in the section entitled “Strong Interaction” connects the acoustic disturbance to a position on the shock near the axis of symmetry in both cases.

There is also asymmetry of the acoustic disturbances. Figure 73 shows the pressure perturbations along radii extending from the vortex core at ±40°, ±50°, and ±60°. For ease of comparison, the results have been plotted so that the pressure disturbance associated with the positive angle of the CW vortex is compared with the negative angle of the CCW rotating vortex. The results show good agreement between the pressure peak at the positive angle for the CW vortex and the negative angle for the CCW vortex. However, there is a significant difference in the maximum pressure amplitude of the disturbances that corresponds to the CW vortex at a negative angle and the CCW vortex at the positive angle. For these cases, the CW vortex generates a larger pressure disturbance. The largest difference is 156 percent for the sound disturbance traveling at ±60° from the horizontal.

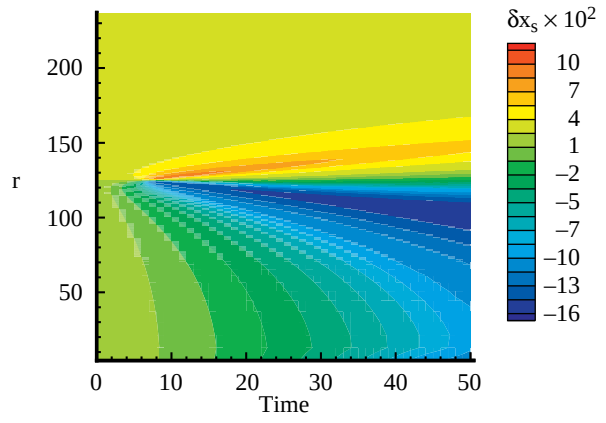

Figure 71. Shock displacement as a function of space and time.

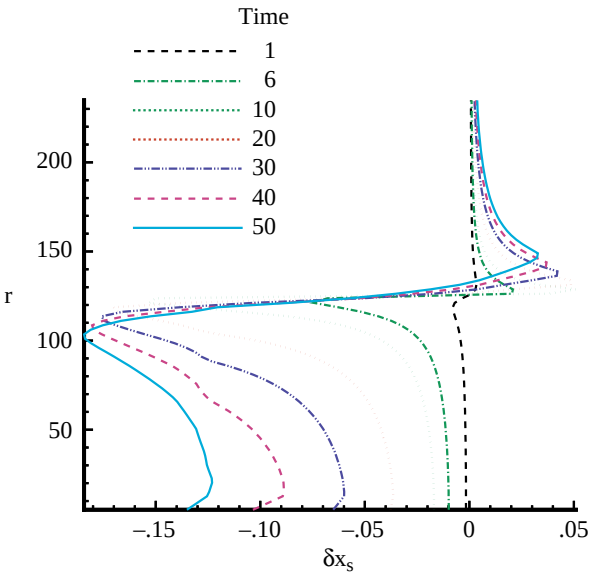

Figure 72. Shock displacement as a function of radial distance for $T = 1$, $T = 6$, and $T = 10$ through $T = 50$.

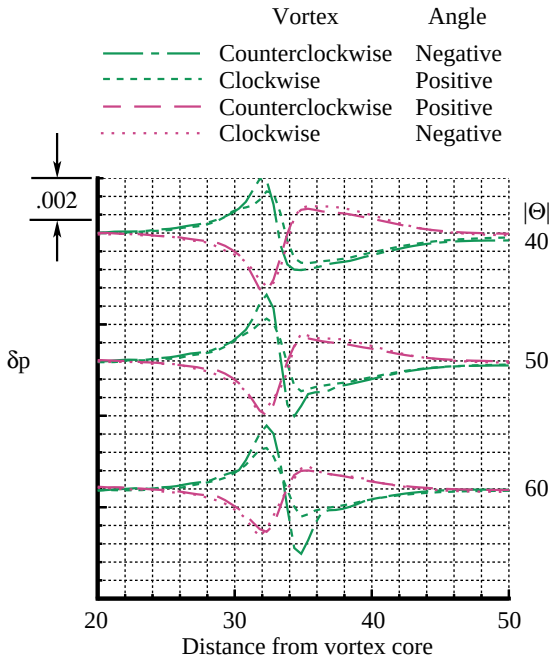

Figure 73. Pressure perturbations along radii at ±40°, ±50°, and ±60° extending from vortex core at $x = 30$, $y = 125$.

Effect of Vortex Core Size

To show the effect of vortex core size relative to the vortex ring size, a study is included in which the ratio of the core radius to ring radius is 1/250. Figure 74 shows the contours of change in pressure at $T = 50$ for this case. The range of pressure levels in the contour plot is kept the same as in figure 40 for direct comparison. The strength and wavelength of the acoustic waves are essentially identical to those in the case where the ratio of core radius to ring radius is 1/125. The primary difference is that the cusp-shaped structure so apparent in the core radius to ring radius shown in figure 40 is no longer visible on

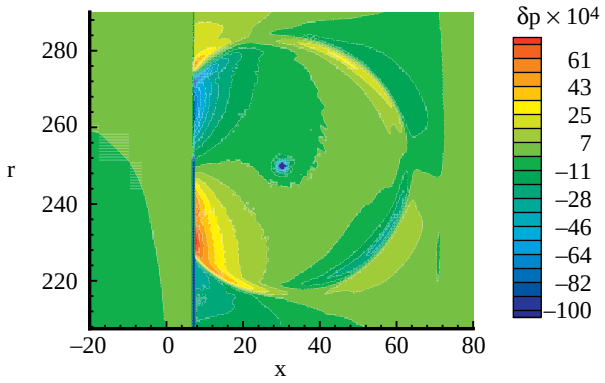

Figure 74. Contours of pressure perturbation for Γ= 0.75, upstream M = 1.5, and ratio of vortex core radius to ring radius is 1/250.

the contour plot. This lack of a cusp-shaped structure indicates that the presence of this wave may be related to axisymmetry. As the vortex ring becomes larger relative to the core size, the resultant wave structures more closely resemble those generated in a two-dimensional planar interaction, which does not show the cusp-shaped structure.

Summary of Chapter 4

In this chapter, the interaction of a ring vortex with a shock wave is presented as a simple model for a mechanism responsible for generating shock noise in imperfectly expanded supersonic jets. This model was inspired by the works of Ribner (refs. 49 and 50) and Moore (ref. 38) who considered two-dimensional interactions of disturbances with shock waves in the context of linear theory. The model reported herein differs from these pioneering studies because the interaction considered more closely models the interaction of axisymmetric turbulent structures within axisymmetric jets. In addition, the present study provides a tool for solving the nonlinear equations that govern the fluid dynamics of this very complex interaction.

An effort was made in the design of these calculations to model the physical parameters of an imperfectly expanded jet. The size of the vortex core relative to the vortex ring radius was small because of numerical considerations, so flow parameters were chosen to model the interaction of a turbulent disturbance with a shock wave in the first shock cell. The magnitude of the vortex strength and the sense of the vortex rotation were chosen to be consistent with those observed in experiments. The range of Mach numbers studied was within the range for practical nozzles.

Observation leads to the conclusion that sound, entropy, and vorticity are generated downstream of the shock wave during the interaction process. The sound wave is isentropic and propagates downstream at the sum of the convection and sound speeds. Contact surfaces are formed during the interaction process. These disturbances do not support a difference in pressure, but do support differences in density, entropy, and vorticity. Both sound waves and contact surfaces have been observed in experimental studies of shock and vortex interaction. It is believed that these are the first calculations performed with enough resolution to show the presence of the contact surfaces downstream of the shock for these flows. Contact surfaces have been observed in experiments. These experiments provide evidence for the physical nature of these disturbances, but as discussed in chapter 3, numerical error associated with moving shock waves may readily manifest itself in entropy, so further analysis is necessary to validate the strength of the computed contact disturbances.

The structure of the contact surfaces is related to the shock dynamics. The contact disturbances are observed to be generated by a wave that is initiated during the interaction and travels along the shock

both towards and away from the center of the vortex ring. The motion of the shock corresponding to the wave traveling along its length generates entropy and vorticity disturbances. Pressure perturbations are also observed to originate at the locations of large shock motion.

Analysis of the data provides further insight into the physics of the interaction. A frequency analysis suggests that the sound wave generated in these computations decays as a cylindrical wave. This cylindrical decay rate is due to the presence of the shock wave, which acts as a barrier to sound spreading upstream of the shock. An analysis of sound intensity level provides insights into the directive nature of the sound wave. High intensity levels are observed close to the shock wave and in downstream directions at angles of approximately 50° and −55° from a horizontal axis through the vortex filament for the case where the upstream Mach number is 1.5.

Additional studies of the interaction of a strong vortex with a shock wave validated the robustness of the numerical code used in this work. The interaction produced extremely high gradients in the flow downstream of the shock and the computation maintained stability.

The sound generated by clockwise and counterclockwise rotating vortices was compared. It was found that the structure of the alternating compression and rarefaction zones along the sound wave changed sign when the sense of the vortex rotation changed. (Regions of compression resulting from the clockwise vortex became regions of rarefaction for the counterclockwise vortex and vice versa.) It is also observed that the clockwise rotating vortex generates disturbances that can be significantly larger in amplitude. The peak pressure perturbation resulting from the interaction of the clockwise rotating vortex and the shock produces pressure levels up to 156 percent higher than the counterclockwise rotating vortex.

A study of the effect of the ratio of core size to ring size was also performed. This study shows that the effects of axisymmetry are reduced when the core radius size is decreased relative to ring radius.

A study of the effect of flow Mach number on the sound pressure level found that the sound pressure level increased with Mach number. The rate of this increase corresponds closely to that observed in experimental data of shock noise of supersonic jets. This result implies that the interaction of a vortex ring with a shock wave is a dominant physical process in shock noise generation in supersonic jets.

Conclusions

This research pioneered the application of a direct computational approach to the study of shock noise mechanisms. Direct simulation of sound generation in shocked flows is challenging because of the disparity in amplitudes between the acoustic waves and the shock waves. These challenges were met by the implementation of an essentially nonoscillatory (ENO) scheme that uses adaptive stenciling to maintain high-order accuracy in smooth regions of the flow. This maintenance of high-order accuracy minimized numerical dissipation of the acoustic waves while maintaining sufficient numerical dissipation at the shock for stability. A study of the economics of high-order schemes shows that the added cost of higher order algorithms should be balanced with the level of accuracy required. An analysis performed for sound in a converging nozzle showed that for a numerical error on the order of 10^{-6}, the third order accurate ENO scheme is the most cost-effective. Therefore, a third order ENO algorithm was used for most of the work presented herein. A study of the numerical error in the computation of slowly moving shock waves showed that spurious numerical waves were produced downstream of the shock. The numerical error manifested itself primarily in entropy and is a function of the algorithm used in the computation and the shock speed relative to the grid. As the shock speed relative to the grid increases, the entropy error decreases.

This report presents and describes the modeling of sound generating mechanisms in a supersonic jet. Experimental evidence is presented to illustrate that shock noise contributes significantly to the sound field of a supersonic jet. Two mechanisms of sound generation by shocked flows were

investigated: shock motion and shock deformation. These mechanisms were modeled by the interaction of sound disturbances with shock waves and the interaction of vortical structures with shock waves. These models permit the consideration of shock oscillation and shock deformation in the development of sound.

Analysis of shock motion with Lighthill's equation showed that monopole, dipole, and quadrupole terms all have potential to contribute to the far field sound. At low supersonic Mach numbers, the monopole term dominates, followed by the dipole. The dipole term is highly directional.

Shock motion was modeled numerically by the interaction of a sound wave with a shock wave. During the interaction, the shock wave begins to move and the sound pressure is amplified as the sound wave passes through the shock wave. Computations of sound waves interacting with shocks in a converging-diverging nozzle were performed. The results show that the amplitude of the transmitted pressure perturbation is greater than the incident pressure perturbation for all Mach numbers greater than one. The numerical approach was validated by comparison of the computed ratio of transmitted with incident sound pressures with linear theory. The comparison is good over the range of shock Mach numbers studied ($1.3 < M < 2.6$). An energy analysis was performed to determine whether acoustic energy was generated in the sound and shock interaction. The analysis is based on an exact representation of the transport of energy in an arbitrary flow field and shows that acoustic energy is generated during the sound and shock interaction. The source term of this energy was shown to be confined to a region along the shock wave in space and time, and is a function of the changes in entropy, momentum, and temperature in the mean flow state.

Shock deformation was investigated by the simulation of a ring vortex interacting with a shock wave. This investigation has practical significance because it models the passage of a turbulent structure through a shock wave. Observations of the evolution of perturbations in pressure, density, entropy, vorticity, and velocity downstream of the shock lead to the conclusion that acoustic waves and contact surfaces are generated by the interaction of shock and vortex. That these two fluid structures were generated by the interaction was validated by experimental evidence. The structure of the contact surfaces was related to the shock dynamics. The contact surfaces were observed to be generated by disturbances that were initiated during the interaction and traveled along the shock both towards and away from the center of the vortex ring. The motion and deformation of the shock generated entropy and vorticity, respectively.

Analysis of the numerical results demonstrated that the sound wave that results from the interaction of a vortex ring with a shock wave spreads cylindrically. This cylindrical spreading is due primarily to the presence of the shock wave, which acted as a barrier to sound traveling upstream. Analysis of the sound intensity level over the region of the computation provided insight into the directivity of the sound. High intensity levels were seen along the shock wave at angles of approximately 50° and –55° from a horizontal axis through the vortex filament when the upstream Mach number was 1.5. The peak sound amplitude that was generated by a clockwise rotating vortex was found to be as much as 156 percent higher than sound generated by the interaction of a counterclockwise rotating vortex and shock wave. A significant result of this work is that the sound pressure level was shown to increase with shock strength. The relationship between the sound pressure and shock strength, defined by the parameter $\beta = \sqrt{M^2 - 1}$, is shown to be approximately: sound pressure $\propto \beta^4$. This relationship is consistent with experimental observations of shock noise in supersonic jets and implies that the interaction of a vortex ring with a shock wave is a dominant physical process in the physics of shock noise generation.

NASA Langley Research Center
Hampton, VA 23681-0001
November 8, 1996

Appendix A

Derivation of Unsteady Shock Jump Relations

In this appendix, the shock jump relations for a moving shock are derived by using generalized functions. The results obtained here for the continuity and momentum equations are also in reference 9 without a derivation of the unsteady shock jump relation for the energy.

Generalized functions will not be defined in a rigorous mathematical context here, but will be presented to show the connection between generalized and ordinary functions for clarity. (See ref. 9 and its references for details.)

Conventionally, a function is defined as a table of ordered pairs (x, $f(x)$), where for each x, $f(x)$ is unique. This table may have an infinite number of ordered pairs. In an analogous fashion, in generalized function theory, the function $f(x)$ is defined by its action on a given space of ordinary functions called test function space:

$$F[\phi] = \int_{-\infty}^{\infty} f(x)\ \phi(x)\ dx \tag{A1}$$

where the function $\phi(x)$ is a test function that must satisfy certain properties given in reference 9. The mapping described by equation (A1) is functional. The function f is now identified by the new table $F[\phi]$, $\phi \in$ test function space.

It can be shown that there are an infinite number of functions ϕ that satisfy the conditions prescribed on the space of test functions, so the table produced by equation (A1) has an uncountably infinite number of elements. The space of test functions is so large that the functions on this space generated by equation (A1) contain not only ordinary functions, but also generalized functions. Thus, ordinary functions are a subset of the generalized functions. It can be shown from classical Lebesque integration theory that the Dirac delta function cannot be an ordinary function (ref. 9). However, functions such as the Dirac function are included in the definition of generalized functions. Now that the concept of function space has been extended to include functions such as the Dirac function, the extension of the definition of derivative is presented.

Let $f(x,y,z)$ be a piecewise smooth function with one surface of discontinuity. Denote this surface by $g = 0$. Such a surface is illustrated in figure A1. At this surface of discontinuity, there is a jump in the value of the function denoted by

$$\Delta f = f(g = 0^{+}) - f(g = 0^{-}) \tag{A2}$$

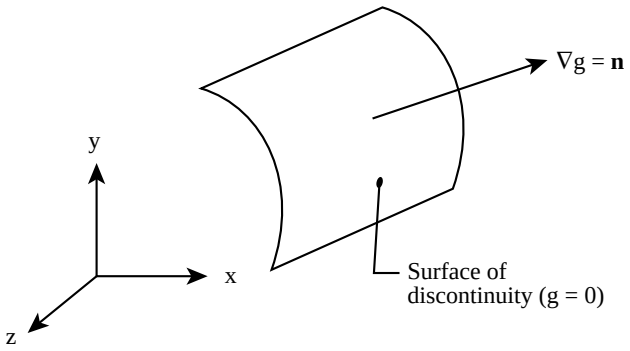

Figure A1. Schematic of a discontinuous surface.

Note that $g = 0^+$ is on the side of the surface into which ∇g points and that, following Farassat, $\nabla g = \mathbf{n}$ (ref. 9).

The generalized divergence of a vector $f\ \overline{\nabla} \cdot \mathbf{f}$ is related to the ordinary divergence $\overline{\nabla} \cdot \mathbf{f}$ and the jump across the surface normal $\Delta\mathbf{f}$ by

$$\begin{aligned} \overline{\nabla} \cdot \mathbf{f} &= \nabla \cdot \mathbf{f} + \nabla g \cdot \Delta\mathbf{f}\delta(g) \\ &= \nabla \cdot \mathbf{f} + \mathbf{n} \cdot \Delta\mathbf{f}\delta(g) \end{aligned} \tag{A3}$$

The shock jump relations for a flow in which a discontinuity in the flow is moving may be derived by using equation (A3). The differential forms of the laws governing the conservation of mass, momentum, and energy are valid even when discontinuities exist within the region, as long as the derivatives are interpreted as generalized derivatives. The application of generalized derivatives to the conservation laws is most readily performed when the equations are in divergence form. Begin by considering the conservation of mass

$$\frac{\bar{\partial}\rho}{\partial t} + \overline{\nabla} \cdot (\rho\mathbf{u}) = 0 \tag{A4}$$

Applying the definition of the generalized derivative equation (A3)

$$\frac{\partial\rho}{\partial t} + \Delta(\rho)\frac{\partial g}{\partial t} + \nabla \cdot (\rho\mathbf{u}) + \Delta(\rho\mathbf{u}) \cdot \mathbf{n}\delta(g) = 0 \tag{A5}$$

The sum of the first and third terms defines the ordinary continuity equation, thus this sum is zero. The term $\partial g/\partial t$ is equal to the negative of the velocity of the surface $-v_n$.

Thus,

$$\Delta[\rho(u_n - v_n)] = 0 \tag{A6}$$

where $u_n = \mathbf{u} \cdot \mathbf{n}$ is the component of velocity normal to the surface g and v_n is the velocity of the surface. If the states upstream and downstream of a shock are denoted by the subscripts 1 and 2, respectively, and the shock is not moving, note that equation (A6) reduces to the Rankine-Hugoniot relation for steady flows in one dimension:

$$\rho_2 u_2 = \rho_1 u_1$$

Consider now the conservation of momentum:

$$\frac{\bar{\partial}(\rho u_i)}{\partial t} + \frac{\bar{\partial}(\rho u_i u_j)}{\partial x_j} + \frac{\bar{\partial} p}{\partial x_i} = 0 \tag{A7}$$

Applying the definition of generalized derivatives

$$\frac{\partial(\rho u_i)}{\partial t} + \frac{\partial(\rho u_i u_j)}{\partial x_j} + \frac{\partial p}{\partial x_i} + \left[\Delta(\rho u_i)\frac{\partial g}{\partial t} + \Delta\rho u_i u_j \frac{\partial g}{\partial x_j} + \Delta p \frac{\partial g}{\partial x_i}\right]\delta(g) = 0 \tag{A8}$$

But, since $\partial g/\partial t = -v_n$ and $\partial g/\partial x_j = n_j$, and the sum of the first three terms is equivalent to the momentum equation for continuous flows, equation (A8) reduces to

$$\Delta[\rho u_i(u_n - v_n) + p n_i] = 0 \tag{A9}$$

Again, note that when the shock is not moving, this equation reduces to the Rankine-Hugoniot relation for steady, one-dimensional flow:

$$\rho_2 u_2^2 + p_2 = \rho_1 u_1^2 + p_1$$

Now consider the energy equation

$$\frac{\bar{\partial} e}{\partial t} + \frac{\bar{\partial}(e + p)u_i}{\partial x_i} = 0 \tag{A10}$$

where e is the total energy defined by $e = \rho h + 1/2\,\rho u^2 - p = \rho H - p$. The total specific enthalpy is represented by the symbol H. Applying the definition of the generalized derivative

$$\frac{\partial e}{\partial t} + \frac{\partial (e + p)u_i}{\partial x_j} + \left\{ \Delta(e)\frac{\partial g}{\partial t} + \Delta[(e + p)u_i]\frac{\partial g}{\partial x_i} \right\}\delta(g) = 0 \tag{A11}$$

Making simplifications similar to those made for the continuity and momentum equations

$$-\Delta(e)v_n + \Delta[(e + p)u_n] = 0 \tag{A12}$$

$$-\Delta\left(\rho h + \frac{1}{2}\rho u^2 - p\right)v_n + \Delta\left[\left(\rho h + \frac{1}{2}\rho u^2\right)u_n\right] = 0 \tag{A13}$$

$$\Delta\left[\left(\rho h + \frac{1}{2}\rho u^2\right)(u_n - v_n) + p v_n\right] = 0 \tag{A14}$$

For steady one-dimensional flow, equation (A14) reduces to the Rankine-Hugoniot relation

$$h_2 + \frac{1}{2}\rho_2 u_2^2 = h_1 + \frac{1}{2}\rho_1 u_1^2$$

Appendix B

Equations for the Velocity and Pressure of a Ring Vortex

For the purpose of prescribing the initial condition for the numerical calculation, the vortex ring is assumed to be incompressible. The vortex moves relative to a fixed coordinate system at a velocity equal to the sum of the mean flow velocity *U* and the vortex translational velocity *V*. A cross section of the vortex ring is illustrated in figure B1. The equations for velocity and pressure in the fluid as a result of the presence of the vortex are derived for the purpose of prescribing an initial condition for a numerical calculation.

Velocity Outside the Core

Lamb provides the expression for the stream function ψ of a vortex ring (ref. 59)

$$\psi = -\frac{\Gamma r r_0^{1/2}}{2\pi}\left[\left(\frac{2}{K} - K\right)K(k) - \frac{2}{K}E(k)\right] \tag{B1}$$

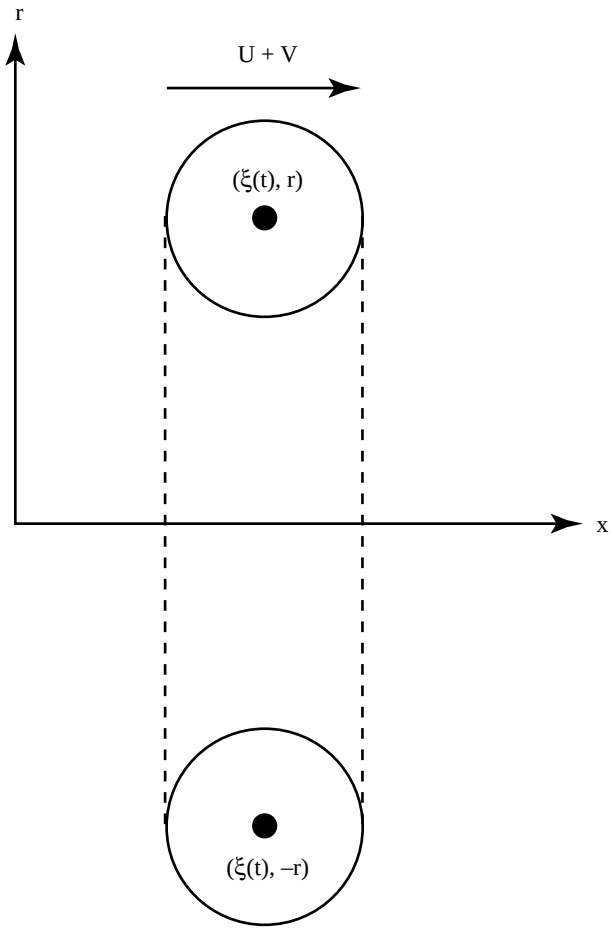

Figure B1. Ring vortex moving at a velocity $U + V$ with respect to a fixed coordinate system (x, r).

where Γ is the circulation, r is the distance from the axis of symmetry, and K and E are the complete elliptic integrals of the first and second kind

$$K(m) = \int_0^{\frac{\pi}{2}} (1 - m \sin^2 \theta)^{-\frac{1}{2}} d\theta \tag{B2}$$

$$E(m) = \int_0^{\frac{\pi}{2}} (1 - m \sin^2 \theta)^{\frac{1}{2}} d\theta \tag{B3}$$

where m is an index and

$$k^2 = \frac{4rr_0}{[(x - x_0)^2 + (r + r_0)^2]} \tag{B4}$$

where r_0 and x_0 are the radial and axial positions of the vortex filament, respectively.

Given the stream function, axial and radial velocity components u and v, respectively, can be found:

$$\begin{aligned} u &= -\frac{1}{r}\frac{\partial \psi}{\partial r} \\ &= \frac{\Gamma}{2\pi r_2}\left\{K(k) + \frac{\left[r_0^2 - (x - x_0)^2 - r^2\right]}{r_1^2}E(k)\right\} \end{aligned} \tag{B5}$$

$$\begin{aligned} v &= \frac{1}{r}\frac{\partial \psi}{\partial x} \\ &= -\frac{\Gamma}{2\pi r_2}\frac{x - x_0}{rr_2}\left\{K(k) - \frac{\left[r_0^2 + (x - x_0)^2 + r^2\right]}{r_1^2}E(k)\right\} \end{aligned} \tag{B6}$$

where

$$r_1 = \sqrt{(r - r_0)^2 + (x - x_0)^2}$$

$$r_2 = \sqrt{(r + r_0)^2 + (x - x_0)^2}$$

In the implementation of these equations for vortex velocity, the polynomial approximations of $K(k)$ and $E(k)$, which have an error bounded by 2×10^{-8}, are used (ref. 64).

Velocity Inside the Core

To avoid mathematical singularity on the vortex filament and to better model the physics of a real, viscous vortex, the velocity distribution inside the vortex core is assumed to have a linear distribution of tangential velocity:

$$u = v_\theta \sin\theta \frac{R}{r_c} \tag{B7}$$

$$v = v_\theta \cos\theta \frac{R}{r_c} \tag{B8}$$

where v_θ is the tangential velocity at the core radius r_c and R and θ are the polar coordinates centered on the vortex filament. The tangential velocity v_θ is known by substituting $x = x_0 + r_c$ where $r = r_0$ into equation (B6). Note that this description of the core assumes that the core is circular. This equation is an approximation since the core is elliptical for finite values of r_c/r_0.

Pressure Outside the Core

The pressure field of this vortex is determined by momentum conservation. Consider the momentum equation for an irrotational flow:

$$-\frac{1}{\rho} \nabla p = \nabla \frac{q^2}{2} + \frac{\partial \mathbf{u}}{\partial t} \tag{B9}$$

where ρ is density, p is pressure, q is the magnitude of the velocity vector, and $\mathbf{u}$ is the velocity vector $[u,v]^T$. Now, the velocity component in the axial direction is $u = U + u_v(x - \xi(t),r)$ where U is the mean flow velocity, u_v is the perturbation velocity induced by the vortex, the coordinate ξ is the vortex filament position, t is time, and r is radial distance. The radial component of velocity is $v = v_v(x - \xi(t),r)$, where v_v is the velocity induced by the vortex.

The flow is not steady in the fixed reference frame because the position of the vortex varies as a function of time $\xi = x + (U + V)t$, where V is the vortex translational velocity. Evaluating the derivative $\partial u/\partial t$ results in

$$\begin{aligned}
\frac{\partial u}{\partial t} &= \frac{\partial u_v(x-\xi(t),y)}{\partial t} \\
&= \frac{\partial u_v}{\partial [x-\xi(t)]} \frac{\partial [x-\xi(t)]}{\partial t} \\
&= \frac{\partial u_v}{\partial (x-\xi)} (U+V) \\
&= -\frac{\partial u_v}{\partial x} (U+V)
\end{aligned} \tag{B10}$$

Similarly,

$$\frac{\partial v}{\partial t} = -\frac{\partial v}{\partial x}(U+V) \tag{B11}$$

Note that for irrotational flow, $\partial v/\partial x = \partial u/\partial r$. Therefore, $\partial v_v/\partial x = \partial u_v/\partial r$ so that

$$\frac{\partial \mathbf{u}}{\partial t} = -\nabla u_v (U+V) \tag{B12}$$

If density is assumed to be constant, the momentum equation can be written

$$\nabla \left[\frac{p}{\rho} + \frac{q^2}{2} - (U+V)u_v \right] = 0 \tag{B13}$$

where $q^2 = u^2 + v^2 = (U + u_v)^2 + v_v^2$. Substituting for u and v and evaluating the integral of equation (B13) along a streamline that terminates in the mean flow state where the velocity induced by the vortex is zero, results in

$$p - p_0 = -\frac{\rho_0}{2}(u_v^2 + v_v^2) + \rho_0 V u_v \tag{B14}$$

where the subscript 0 denotes the mean flow state.

Pressure Inside the Core

Equation (B14) is valid for the flow outside the vortex core, where the flow is irrotational. To determine the pressure field inside the vortex core where the flow is rotational, consider the radial momentum equation

$$dp = \frac{\rho v_\theta^2}{r}\, dr \tag{B15}$$

Substituting for v_θ and integrating from the edge of the vortex core to r,

$$p(r) = p(r_c) + \frac{\rho_0}{2}\frac{v_\theta^2}{r_2^2}\left(r^2 - r_c^2\right) \tag{B16}$$

assuming that $\rho = \rho_0$. The pressure $p(r_c)$ that is determined from equation (B14) to ensure continuity of pressure across the vortex core interface is

$$p(r_c) = p_0 - \frac{\rho_0}{2} v_\theta^2 \tag{B17}$$

The pressure profile of a counterclockwise vortex of strength $\Gamma = 0.75$ is shown in figure B2. Note the asymmetry in the pressure field relative to the vortex filament and the region of slightly positive pressure below the filament.

When the vortex ring is the initial condition, the flow quantities are normalized with respect to the upstream static pressure and density and the vortex core radius.

Remarks

Note that although the pressure and the velocity are defined to be continuous at the rim of the vortex core, the derivatives of these quantities are not. Because the natural dissipation in the algorithm will automatically smooth these derivatives at the rim, discontinuities in derivatives at the rim are not a problem with this algorithm. Less robust schemes may have difficulty with this initial condition.

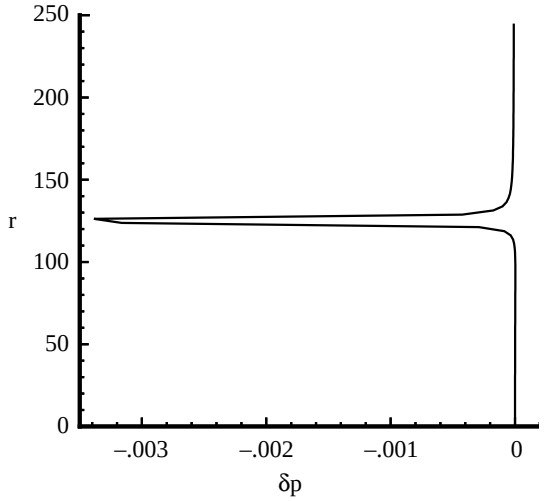

(a) Overall pressure distribution range.

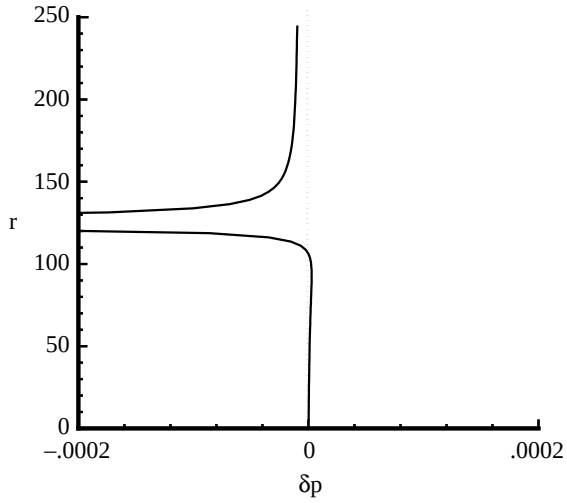

(b) Detail of pressure distribution range.

Figure B2. Profile of pressure distribution of counterclockwise rotating ring vortex of $\Gamma = 0.75$.

Appendix C

Finite Wave Boundary Conditions

General Description

This report uses the inflow and outflow boundary conditions developed by Atkins and Casper (ref. 44). Some equations from reference 44 are examined in this appendix for completeness.

The formulation of these boundary conditions is based upon the Riemann approach, which is illustrated in figure C1. As shown in the figure, the finite wave models assume that state 1 and state 4 are separated by left and right traveling acoustic waves and a convecting entropy wave. This assumption simplifies the mathematics for deriving the equations that were used for the boundary conditions because the wave structure can be solved in closed form without iteration. The finite wave boundary conditions have the advantage that the order of accuracy of the conditions is determined by the order of accuracy of the solver.

The equations that govern the simple waves that are shown in figure C1 are (ref. 65)

$$u_2 - u_1 = -\frac{2n}{\gamma - 1}(c_2 - c_1) \tag{C1}$$

$$\frac{c_2}{c_1} = \left(\frac{p_2}{p_1}\right)^{\frac{\gamma-1}{2\gamma}} \tag{C2}$$

$$u_3 = u_2 \tag{C3}$$

$$p_3 = p_2 \tag{C4}$$

$$u_4 - u_3 = \frac{2n}{\gamma - 1}(c_4 - c_3) \tag{C5}$$

$$\frac{c_4}{c_3} = \left(\frac{p_4}{p_3}\right)^{\frac{\gamma-1}{2\gamma}} \tag{C6}$$

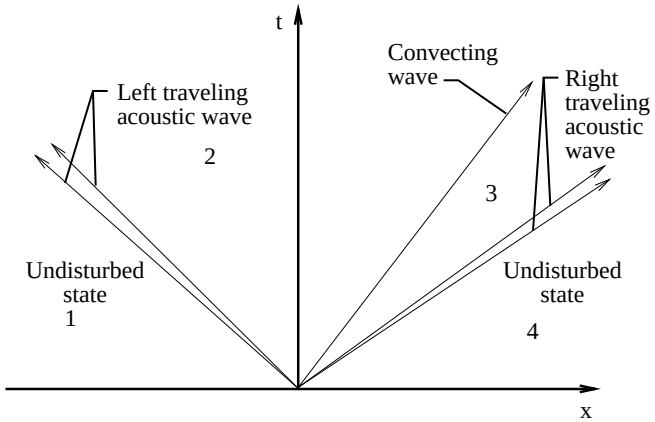

Figure C1. Diagram of quasi-steady Riemann analysis used in derivation of finite wave boundary conditions.

where the subscript denotes the state, u is the flow speed, c is the sound speed, p is the pressure, γ is ratio of specific heats, and n is a sign parameter defined to be +1 or −1 for the inflow and outflow boundaries, respectively (ref. 29).

Note that equations (C1) and (C2) describe left traveling acoustic waves, equations (C3) and (C4) describe convecting entropy waves, and equations (C5) and (C6) describe right traveling acoustic waves.

These equations can be arranged so that states 2 and 3 are described completely by states 1 and 4:

$$c_2 = c_1 \left[\frac{n\frac{\gamma-1}{2}(u_1 - u_4) + c_1 + c_4}{c_1 + c_4\left(\frac{p_1}{p_4}\right)^{\frac{\gamma-1}{2\gamma}}} \right] \tag{C7}$$

$$p_3 = p_2 = p_1\left(\frac{c_2}{c_1}\right)^{\frac{2\gamma}{\gamma-1}} \tag{C8}$$

$$c_3 = c_4\left(\frac{p_3}{p_4}\right)^{\frac{\gamma-1}{2\gamma}} \tag{C9}$$

$$u_3 = u_2 = u_1 - \frac{2n}{\gamma-1}(c_2 - c_1) \tag{C10}$$

The boundary state sought is either state 2 or state 3, depending on the direction of the flow. When the flow is into the domain (inflow boundary), state 2 is the correct boundary state. State 3 becomes the boundary state when the flow leaves the computational domain (outflow boundary).

Example

To illustrate the implementation of the finite wave conditions, consider the interaction of a plane wave with a shock with the quasi-one-dimensional Euler equations of chapter 2.

Inflow

The upstream exterior state is defined to be the conditions for a steady ambient flow, represented here by the subscript $-\infty$.

The acoustic wave introduced to the inflow boundary satisfies the expression

$$\delta p = \varepsilon p_{-\infty} \sin \omega t \tag{C11}$$

where $p_{-\infty}$ is the pressure at the ambient (steady) upstream state, ε is an amplitude parameter, ω is the frequency of the acoustic wave, and t is time.

Therefore, the pressure at state 1 is

$$p_1 = p_{-\infty} + \delta p \tag{C12}$$

The corresponding sound speed, velocity, and density are, respectively,

$$c_1 = c_{-\infty}\left(\frac{p_4}{p_{-\infty}}\right)^{\frac{\gamma-1}{2\gamma}} \tag{C13}$$

$$u_1 = u_{-\infty} + \frac{2}{\gamma-1}(c_1 - c_{-\infty}) \tag{C14}$$

$$\rho_1 = \left(\frac{p_1}{s_{-\infty}}\right)^{\frac{1}{\gamma}} \tag{C15}$$

where $s_{-\infty}$ is the inflow entropy. State 4 is determined by the computational interior. Thus state 4 is defined by the solution in the first computational cell within the domain.

Now that both states 1 and 4 are defined, the boundary condition is determined by solving for state 2 with equations (C7) through (C10).

Outflow

For the outflow condition, the downstream exterior state (state 4) is defined to be steady ambient flow, represented by ∞. For this state, the conditions at ∞ are determined so that the Rankine-Hugoniot jump conditions are satisfied across the shock, given an upstream ambient state at −∞. The interior state (state 1) is defined by the computational interior, in this case the last cell of the computational domain. The boundary conditions are determined by solving for state 3 with equations (C7) through (C10).

References

1. Seddon, J.; and Goldsmith, E. L.: *Intake Aerodynamics*. AIAA/Collins Professional and Technical Books, 1985.

2. Morley, A. W.: Estimation of Aeroplane Noise Level: Some Empirical Laws With an Account of the Present Experiments on Which They Are Based. *Aircr. Eng.*, vol. 11, no. 123, May 1939, pp. 187–189.

3. Lighthill, M. J.: On Sound Generated Aerodynamically. I. General Theory. *Proc. R. Soc*. (London), vol. 211, no. 1107, Mar. 1952, pp. 564–587.

4. Lilley, G. M.: *Jet Noise Classical Theory and Experiments. Aeroacoustics of Flight Vehicles: Theory and Practice, Volume 1: Noise Sources*, Harvey H. Hubbard, ed., NASA RP-1258, Vol. 1, WRDC TR-90-3052, 1991, pp. 211–289.

5. Seiner, J. M.: Advances in High Speed Jet Aeroacoustics. *Ninth Aeroacoustics Conference*, AIAA, Oct. 1984. (Also available as AIAA-84-2275.)

6. Tam, Christopher K. W.: Supersonic Jet Noise. *Annu. Rev. Fluid Mech*., vol. 27, 1995, pp. 17–43.

7. Powell, A.: On the Mechanism of Choked Jet Noise. *Proc. Phys. Soc.* (London), vol. 66, pt. 12, no. 408B, Dec. 1953, pp. 1039–1056.

8. Norum, T. D.; and Seiner, J. M.: Broadband Shock Noise From Supersonic Jets. *AIAA J*., vol. 20, no. 1, Jan. 1982, pp. 68–73.

9. Farassat, F.: *Introduction to Generalized Functions With Applications in Aerodynamics and Aeroacoustics*. NASA TP-3428, 1994.

10. Ellzey, Janet L.; Henneke, Michael R.; Picone, J. Michael; and Oran, Elaine S.: The Interaction of a Shock With a Vortex—Shock Distortion and the Production of Acoustic Waves. *Phys. Fluids*, vol. 1, Jan. 1995, pp. 172–184.

11. Gradshteyn, I. S.; and Ryzhik, I. M. (Scripta Technica, Inc., transl.): *Table of Integrals, Series, and Products*, Fourth ed., Academic Press, Inc., 1965.

12. Seiner, J. M.; and Norum, T. D.: Aerodynamic Aspects of Shock Containing Jet Plumes. *Sixth Aeroacoustics Conference*, AIAA, June 1980. (Also available as AIAA-80-0965.)

13. Roberts, Thomas W.: The Behavior of Flux Difference Splitting Schemes Near Slowly Moving Shock Waves. *J. Comput. Phys.*, vol. 90, Sept. 1990, pp. 141–160.

14. Meadows, Kristine R.; Caughey, David A.; and Casper, Jay: Computing Unsteady Shock Waves for Aeroacoustic Applications. *AIAA J.*, vol. 32, no. 7, pp. 1360–1366.

15. Watson, Willie Ross: A Time Domain Numerical Theory for Studying Steady-State Acoustic Disturbances in Flow. Ph.D. Diss., The George Washington Univ., May 1991.

16. Hardin, J. C.; and Pope, D. S.: A New Technique for Aerodynamic Noise Calculation. *Proceedings of DGLR/AIAA 14th Aeroacoustics Conference*, May 1992, pp. 448–456. (Also available as AIAA-92-02-076.)

17. Nark, Douglas Martin: A Computational Aeroacoustics Approach to Sound Generation by Baffled Pistons. M.S. Thesis, The George Washington Univ., July 1992.

18. Anderson, Dale A.; Tannehill, John C.; and Pletcher, Richard H.: *Computational Fluid Mechanics and Heat Transfer*. Hemisphere Publ. Corp., 1984.

19. Hirsch, Charles: *Numerical Computation of Internal and External Flows: Volume 2—Computational Methods for Inviscid and Viscous Flows*. John Wiley & Sons, 1990.

20. Jameson, A.: A Steady-State Solution of the Euler Equations for Transonic Flow—Transonic Shock and Multi-Dimensional Flows. *Advances in Scientific Computing*, R. Meyer, ed., Academic Press, 1982, pp. 37–70.

21. Casper, Jay; and Carpenter, Mark H.: *Computational Considerations for the Simulation of Shock-Induced Sound*. NASA TM-110222, 1995.

22. Harten, Ami; Enquist, Bjorn; Osher, Stanley; and Chakravarthy, Sukumar R.: *Uniformly High Order Accurate Essentially Non-Oscillatory Schemes III*. NASA CR-178101, Apr. 1986. (Also Available as ICASE Rep. No. 86-22.)

23. Shu, Chi-Wang; and Osher, Stanley: Efficient Implementation of Essentially Non-Oscillatory Shock-Capturing Schemes. *J. Comput. Phys.*, vol. 77, Aug. 1988, pp. 439–471.

24. Rogerson, A. M.; and Meiburg, E.: A Numerical Study of the Convergence Properties of ENO Schemes. *J. Sci. Comput.*, vol. 5, no. 2, June 1990, pp. 151–167.

25. Casper, Jay; Shu, Chi-Wang; and Atkins, H.: A Comparison of Two Formulations for High-Order Accurate Essentially Non-Oscillatory Schemes. *11th Computational Fluid Dynamics Conference*, July 1994, pp. 1–9. (Also Available as AIAA-93-3338.)

26. Shu, Chi-Wang: Numerical Experiments on the Accuracy of ENO and Modified ENO Schemes. *J. Sci. Comput.*, vol. 5, no. 2, June 1990, pp. 127–129.

27. Atkins, H. L.: High-Order ENO Methods for the Unsteady Compressible Navier-Stokes Equations. *Tenth Computational Fluid Dynamics Conference*, AIAA, June 1991, pp. 328–338. (Also available as AIAA-91-1557.)

28. Roe, P. L.: Approximate Riemann Solvers, Parameter Vectors, and Difference Schemes. *J. Comput. Phys.*, vol. 43, no. 2, Oct. 1981, pp. 357–372.

29. Osher, Stanley; and Solomon, Fred: Upwind Difference Schemes for Hyperbolic Systems of Conservation Laws. *Math. Comput.*, vol. 38, no. 158, Apr. 1982, pp. 339–374.

30. Woodward, P.; and Colella, P.: The Numerical Simulation of Two-Dimensional Fluid Flow With Strong Shocks. *J. Comput. Phys.*, vol. 54, Apr. 1984, pp. 115–173.

31. Lindquist, Dana R.; and Giles, Michael B.: On the Validity of Linearized Unsteady Euler Equations With Shock Capturing. *Tenth AIAA Computational Fluid Dynamics Conference*, AIAA, 1991, pp. 800–813. (Also available as AIAA-91-1598.)

32. Whitham, Gerald Beresford: *Linear and Nonlinear Waves*. John Wiley & Sons, 1974.

33. Doak, P. E.: On the Interdependence Between Acoustic and Turbulent Fluctuating Motions in a Moving Fluid. *J. Sound and Vib.*, vol. 19, no. 2, Nov. 1971, pp. 211-225.

34. Hardin, Jay C.: *Introduction to Time Series Analysis*. NASA RP-1145, 1986.

35. Meadows, Kristine R.; Casper, Jay; and Caughey, David A.: A Numerical Investigation of Sound Amplification by a Shock Wave. *Computational Aero- and Hydro-Acoustics*, A. Mankbadi, A. Lyrintzis, and O. Baysal, eds., FED-Vol. 147, ASME Book No. H00787, pp. 47–52, 1993.

36. Blokhintsev, D.: Sound Receiver in Motion. *Comptes Rendus (Doklady) De L'Academe Des Sciences De L'URSS*, vol. XLVII, no. 1, 1945.

37. Burgers, J. M.: On the Transmission of Sound Waves Through a Shock Wave. *Koninklijke Nederlandische Adademic van Wetenschappen*, vol. XLIX, no. 3, 1946.

38. Moore, Franklin K.: *Unsteady Oblique Interaction of a Shock Wave With a Plane Disturbance.* NACA Rep. 1165, 1954. (Supersedes NACA TN 2879.)

39. Chang, C. T.: On the Interaction of Weak Disturbances and a Plane Shock of Arbitrary Strength in a Perfect Gas. Ph.D. Thesis, Johns Hopkins University, 1955.

40. Kerrebrock, J. L.: Interaction of Flow Discontinuities With Small Disturbances in a Compressible Fluid. Ph.D. Thesis, California Institute of Technology, 1956.

41. Powell, Alan: *One-Dimensional Treatment of Weak Disturbances of a Shockwave*. Aeronautical Research Council (ARC) No. CP-441, 1959.

42. Zang, T. A.; Hussaini, M. Y.; and Bushnell, D. M.: Numerical Computations of Turbulence Amplification in Shock-Wave Interactions. *AIAA J.*, vol. 22, Jan. 1984, pp. 13–21.

43. Landau, L. D.; and Lifshitz, E. M. (J. B. Sykes and W. H. Reid, transl.): *Fluid Mechanics*. Addison-Wesley Publ. Co., Inc., 1959.

44. Atkins, H. L.; and Casper, Jay: Nonreflective Boundary Conditions for High-Order Methods. *Thirtieth Aerospace Sciences Meeting and Exhibit*, AIAA, Jan. 1993. (Also available as AIAA-93-0152.)

45. Myers, M. K.: Transport of Energy by Disturbances in Arbitrary Steady Flows. *J. Fluid Mech.*, vol. 226, May 1991, pp. 383–400.

46. Naumann, A.; and Hermanns, E.: On the Interaction Between a Shock Wave and a Vortex Field. *Noise Mechanisms—AGARD Conference on Propagation and Reduction of Jet Noise.* AGARD-CP-131, 1973, pp. 23-1–23-7.

47. Hollingsworth, M. A.; and Richards, E. J.: *A Schlieren Study of the Interaction Between a Vortex and a Shock Wave in a Shock Tube*. Aeronautical Research Council (ARC) No. 17985, 1955.

48. Hollingsworth, M. A.; and Richards, E. J.: *On the Sound Generated by the Interaction of a Vortex and a Shock Wave.* Aeronautical Research Council (ARC) No. 2371, 1956

49. Ribner, H. S.: *Convection of a Pattern of Vorticity Through a Shock Wave*. NACA Rep. 1164, 1954. (Supersedes NACA TN 2864.)

50. Ribner, H. S.: *Shock-Turbulence Interaction and the Generation of Noise*. NACA Rep. 1233, 1955. (Supersedes NACA TN 3255.)

51. Pao, S. P.; and Salas, M. D.: A Numerical Study of Two-Dimensional Shock Vortex Interaction. AIAA-81-1205, June 1981.

52. Salas, Manuel D.: Shock-Fitted Euler Solutions to Shock-Vortex. NASA TM-84481, 1982.

53. Hussanini, M. Y.; Kopriva, D. A.; Salas, M. D.; and Zang, T. A.: Spectral Methods for the Euler Equations: Part II—Chebyshev Methods and Shock Fitting. *AIAA J.*, vol. 23, no. 2, Feb. 1985, pp. 234–240.

54. Kopriva, David A.; Zang, Thomas A.; Salas, M. D.; and Hussaini, M. Y.: Pseudospectral Solution of Two-Dimensional Gas-Dynamic Problems. NASA CR-172,230, 1983.

55. Meadows, Kristine R.; Kumar, Ajay; and Hussaini, M. Y.: A Computational Study on the Interaction Between a Vortex and a Shock Wave. AIAA-89-1043, Apr. 1989.

56. Casper, Jay: Finite-Volume Application of High-Order ENO Schemes to Two-Dimensional Boundary-Value Problems. Twenty-Ninth Aerospace Sciences Meeting, AIAA, Jan. 1991. (Also available as AIAA-91-0631.)

57. Hardin, J. C.: An Additional Source of Uncertainty and Bias in Digital Spectral Estimates Near the Nyquist Frequency. *J. Sound & Vib.*, vol. 110, Nov. 1986, pp. 533–537.

58. Seiner, J. M.; and Norum, T. D.: Aerodynamic Aspects of Shock Containing Jet Plumes. *Sixth Aeroacoustics Conference,* AIAA, June 1980, pp. 1–18. (Also available as AIAA-80-9065.)

59. Lamb, Horace: *Hydrodynamics—Treatise on the Mathematical Theory of the Motion of Fluids.* Dover Publ., 1945.

60. Robertson, James Mueller: *Hydrodynamics in Theory and Application.* Prentice-Hall, 1965.

61. Walatka, Pamela P.; Culcas, Jean; McCabe, R. Kevin; Plessel, Todd; and Potter, Rick: *Fast 1.0 User Guide*. RND-92-015, NASA Ames Research Center, Nov. 1992.

62. Hardin, Jay C.: High Reynolds Number Computational Aeroacoustics. *First Joint CEAS/AIAA Aeroacoustic Conference.* Munich, Germany, June 1995, p. 667.

63. Harper-Bourne, M.; and Fisher, J. J.: *The Noise From Shock Waves in Supersonic Jets. Noise Mechanisms*, AGARD-CP-131, Mar. 1974, pp. 11.1–11.13.

64. Abromowitz, Milton; and Stegun, Irene A.; eds.: *Handbook of Mathematical Functions*—With Formulas, Graphs, and Mathematical Tables. 9th printing, Dover Publications, Inc., 1970, pp. 591-592.

65. Liepmann, H. W.; and Roshko, A.: *Elements of Gasdynamics*. John Wiley & Sons, 1957.

REPORT DOCUMENTATION PAGE

Form Approved
OMB No. 0704-0188

1. AGENCY USE ONLY *(Leave blank)*	2. REPORT DATE	3. REPORT TYPE AND DATES COVERED
	April 1997	Technical Paper

4. TITLE AND SUBTITLE
A Study of Fundamental Shock Noise Mechanisms

5. FUNDING NUMBERS
WU 505-59-52-03

6. AUTHOR(S)
Kristine R. Meadows

7. PERFORMING ORGANIZATION NAME(S) AND ADDRESS(ES)
NASA Langley Research Center
Hampton, VA 23681-0001

8. PERFORMING ORGANIZATION REPORT NUMBER
L-17530

9. SPONSORING/MONITORING AGENCY NAME(S) AND ADDRESS(ES)
National Aeronautics and Space Administration
Washington, DC 20546-0001

10. SPONSORING/MONITORING AGENCY REPORT NUMBER
NASA TP-3605

11. SUPPLEMENTARY NOTES

12a. DISTRIBUTION/AVAILABILITY STATEMENT
Unclassified–Unlimited
Subject Category 71
Availability: NASA CASI (301) 621-0390

12b. DISTRIBUTION CODE

13. ABSTRACT *(Maximum 200 words)*

This paper investigates two mechanisms fundamental to sound generation in shocked flows: shock motion and shock deformation. Shock motion is modeled numerically by examining the interaction of a sound wave with a shock. This numerical approach is validated by comparison with results obtained by linear theory for a small-disturbance case. Analysis of the perturbation energy with Myers' energy corollary demonstrates that acoustic energy is generated by the interaction of acoustic disturbances with shocks. This analysis suggests that shock motion generates acoustic and entropy disturbance energy. Shock deformation is modeled numerically by examining the interaction of a vortex ring with a shock. These numerical simulations demonstrate the generation of both an acoustic wave and contact surfaces. The acoustic wave spreads cylindrically. The sound intensity is highly directional and the sound pressure increases with increasing shock strength. The numerically determined relationship between the sound pressure and the Mach number is found to be consistent with experimental observations of shock noise. This consistency implies that a dominant physical process in the generation of shock noise is modeled in this study.

14. SUBJECT TERMS
Computational acoustics; Shock noise; Aeroacoustics; Computational aeroacoustics; Shock waves; Vortices; Shock-vortex interaction; Sound-shock interaction

15. NUMBER OF PAGES
103

16. PRICE CODE
A06

17. SECURITY CLASSIFICATION OF REPORT	18. SECURITY CLASSIFICATION OF THIS PAGE	19. SECURITY CLASSIFICATION OF ABSTRACT	20. LIMITATION OF ABSTRACT
Unclassified	Unclassified	Unclassified	